Supplement to:
State of Wildfires 2024-25

Douglas I. Kelley[1,*] Chantelle Burton[2,*], Francesca Di Giuseppe[3,*], Matthew W. Jones[4,*], Maria L. F. Barbosa[15], Esther Brambleby[4], Joe R. McNorton[3], Zhongwei Liu[6], Anna S. I. Bradley[2], Katie Blackford[7], Eleanor Burke[2], Andrew Ciavarella[2], Enza Di Tomaso[8], Jonathan Eden[9], Igor José M. Ferreira[10], Lukas Fiedler[11 12], Andrew J Hartley[2], Theodore R. Keeping[13], Seppe Lampe[14], Anna Lombardi[8], Guilherme Mataveli[4 10], Yuquan Qu[15], Patrícia S. Silva[16], Fiona R. Spuler[17 18], Carmen B. Steinmann[19 20], Miguel Ángel Torres-Vázquez[21], Renata Veiga[22], Dave van Wees[23], Jakob B. Wessel[24], Emily Wright[2], Bibiana Bilbao[25 26], Mathieu Bourbonnais[27], Gao Cong[28], Carlos M. Di Bella[29 30], Kebonye Dintwe[31], Victoria M. Donovan[32], Sarah Harris[33], Elena A. Kukvaskaya[34], Brigitte N'Dri[35], Cristina Santín[36 37], Galia Selaya[38 39], Johan Sjöström[40], John Abatzoglou[41], Niels Andela[23], Rachel Carmenta[42], Emilio Chuvieco[43], Louis Giglio[44], Douglas S. Hamilton[45], Stijn Hantson[46], Sarah Meier[47], Mark Parrington[8], Mojtaba Sadegh[48], Jesus San-Miguel-Ayanz[49], Fernando Sedano[49], Marco Turco[50], Guido R. van der Werf[51], Sander Veraverbeke[4 15], Liana O. Anderson[52], Hamish Clarke[53], Paulo M. Fernandes[54], Crystal A. Kolden[55]

Correspondence to:
doukel@ceh.ac.uk
chantelle.burton@metoffice.gov.uk
Francesca.DiGiuseppe@ecmwf.int
matthew.w.jones@uea.ac.uk

---
[1] Water and Climate Science, UK Centre for Ecology & Hydrology, Wallingford OX10 8BB, U.K.
[2] Hadley Centre, Met Office, Fitzroy Road, Exeter, UK, EX1 3PB
[3] European Centre for Medium-range Weather Forecast, Shinfield Park, Reading RG29AX, United Kingdom
[4] Tyndall Centre for Climate Change Research, School of Environmental Sciences, University of East Anglia, Norwich Research Park, Norwich, UK, NR4 7TJ
[5] Federal University of São Carlos, Rodovia Lauri Simões de Barros, km 12 - SP-189 - Aracaçu, Buri - São Paulo, 18290-000, Brazil
[6] National Centre for Earth Observation, University of Leicester, Space Park Leicester, 92 Corporation Road, Space City, Leicester, LE4 5SP, UK
[7] Department of Life Sciences, Imperial College London, Chemistry Building CHEM062, South Kensington, London, SW7 2AZ, UK
[8] European Centre for Medium-Range Weather Forecasts, Robert-Schuman-Platz 3, 53175 Bonn, Germany
[9] Centre for Agroecology, Water and Resilience, Coventry University, Wolston Ln, Ryton-on-Dunsmore, Coventry CV8 3LG, UK
[10] Earth Observation and Geoinformatics, National Institute for Space Research (INPE), Astronautas Avenue 1758, São José dos Campos, Brazil, 12227-010
[11] Institute of Oceanography, Center for Earth System Research and Sustainability, University of Hamburg, Bundesstraße 53, 20146 Hamburg, Germany
[12] International Max Planck Research School on Earth System Modelling, Max Planck Institute for Meteorology, Bundesstraße 53, 20146 Hamburg, Germany
[13] World Weather Attribution, Centre for Environmental Policy, Imperial College London, Weeks Building, 16-18 Prince's Gardens, London SW7 1NE
[14] Water & Climate, Vrije Universiteit Brussel, Pleinlaan 2, 1050 Brussel, Belgium
[15] Faculty of Science, Vrije Universiteit Amsterdam, De Boelelaan 1100, Amsterdam, Netherlands, 1081 HV
[16] School of the Environment, Yale University, 195 Prospect St, New Haven, CT 06511, USA
[17] Department of Meteorology, University of Reading, Brian Hoskins Building, Whiteknights Road, Earley Gate, Reading, RG6 6ET, UK
[18] The Alan Turing Institute, British Library, 96 Euston Rd., London NW1 2DB
[19] Institute for Environmental Decisions, Department of Environmental Systems Science, ETH Zurich
[20] Federal Office of Meteorology and Climatology MeteoSwiss, Operation Center 1, P.O. Box 257, 8058 Zurich-Airport, Switzerland
[21] Environmental Remote Sensing Research Group, Department of Geology, Geography and Environment, Universidad de Alcalá, Calle Colegios 2, Alcalá de Henares 28801, Spain
[22] Laboratory for Environmental Satellite Applications (LASA), Department of Meteorology, Federal University of Rio de Janeiro
[23] BeZero Carbon Ltd, 25 Christopher Street, London, EC2A 2BS, UK

59 [24] Department of Mathematics and Statistics, University of Exeter, Harrison Building, University of Exeter, North
60 Park Road, EX4 4QF Exeter, United Kingdom
61 [25] Biology, Departamento de Estudios Ambientales, Universidad Simón Bolívar, Valle de Sartenejas, Aartado
62 89000, Caracas, Venezuela
63 [26] UMR Art-Dev 5281, Université Paul Valéry Montpellier, Site Saint-Charles, France , UMR 5281, Site Saint-
64 Charles 1, Rue du Professeur Henri Serre, F-34090 Montpellier, France
65 [27] Earth, Environmental and Geographic Sciences, University of British Columbia - Okanagan, 1177 University
66 Way, Kelowna, BC, Canada V1V 1V7
67 [28] Department of Geography, University of Hong Kong, 10F, The Jockey Club Tower, Centennial Campus,
68 Pokfulam Road, Hong Kong
69 [29] Departamento de Métodos Cuantitativos y Sistemas de Información, University of Buenos Aires, Av. San
70 Martin 4453 (1417), CABA, Argentina
71 [30] IFEVA (Agricultural Physiology and Ecology Research Institute), Av. San Martin 4453 (1417), CABA, Argentina
72 [31] Department of Environmental Science, University of Botswana, Plot 4775 Notwane Rd, Gaborone Botswana
73 [32] West Florida Research and Education Center, School of Forest, Fisheries, and Geomatics Sciences, University
74 of Florida, 5988 Highway 90, Milton, FL 32583
75 [33] Fire Risk, Research and Community Preparedness, Country Fire Authority, Burwood East, Victoria, Australia
76 [34] Laboratory of Experimental and Applied Ecology, V.N. Sukachev Institute of Forest Siberian Branch of the
77 Russian Academy of Sciences - separate subdivision of the FRC KSC SB RAS, 50/28 Akademgorodok,
78 Krasnoyarsk, Russian Federation, 660036
79 [35] Natural Sciences, Nangui Abrogoua University, 02 BP 801 Abidjan 02
80 [36] Research Institute of Biodiversity (IMIB), CSIC-University of Oviedo-Principality of Asturias, IMIB, Research
81 Building, Mieres Campus, Mieres, Spain, 33600
82 [37] Biosciences, Swansea University, Wallace Building, Singleton Campus, Swansea, UK, SA2 8PP
83 [38] Research and action, ECOSCONSULT, Calle Tte. H. Balcazar No. 24, Santa Cruz de la Sierra
84 [39] Research, Fundacion Innova, Calle Tte. H. Balcazar No. 24, Santa Cruz de la Sierra
85 [40] Fire and Safety, RISE Research institutes of Sweden, Box 857, 51515 Borås, Sweden
86 [41] School of Engineering, University of California, Merced, 5200 N Lake Rd, Merced, CA, 95343, USA
87 [42] Tyndall Centre for Climate Change Research, School of Global Development, University of East Anglia,
88 Norwich Research Park, Norwich, UK, NR4 7TJ
89 [43] Environmental Remote Sensing Research Group, Department of Geology, Geography and Environment,
90 Universidad de Alcalá, Calle Colegios 2, Alcalá de Henares 28801, Spain
91 [44] Department of Geographical Sciences, University of Maryland, College Park, MD 20742
92 [45] Marine, Earth, and Atmospheric Science, North Carolina State University, 2800 Faucette Drive, Raleigh, North
93 Carolina, USA, 27603
94 [46] Hantson, Stijn
95 [47] Land, Environment, Economics and Policy Institute (LEEP), Department of Economics, University of Exeter,
96 Rennes Drive EX4 4ST Exeter, United Kingdom
97 [48] Sadegh, Mojtaba
98 [49] Disaster Risk Management Unit (E.1), Directorate E (Space, Security, and Migration), European Commission
99 Joint Research Centre, European Commission, Rue du Champ de Mars 21, 1050 Brussels, Belgium
100 [50] Regional Atmospheric Modelling (MAR) Group, Regional Campus of International Excellence Campus Mare
101 Nostrum (CEIR), Department of Geography, University of Hong Kong
102 [51] Meteorology and Air Quality, Wageningen University and Research, Droevendaalsesteeg 3-3 A, 6708 PB,
103 Wageningen, the Netherlands
104 [52] Cemaden/MCTI, 500 – Distrito de Eugênio de Melo, São José dos Campos – São Paulo, Brazil
105 [53] FLARE Wildfire Research, School of Agriculture, Food and Ecosystem Sciences, University of Melbourne,
106 Grattan St, Parkville, 3010, Australia
107 [54] ForestWISE—Collaborative Laboratory for Integrated Forest & Fire Management, Centre for the Research and
108 Technology of Agro-Environmental and Biological Sciences, Universidade de Trás-os-Montes e Alto Douro,
109 Quinta de Prados, Vila Real, Portugal, 5000-801
110 [55] Wildfire Resilience Center, School of Engineering, University of California, Merced, 5200 N Lake Rd, Merced,
111 CA 95343, USA
112
113

S2 Supplementary Material for Section 2: Context of Recent Extremes

S2.1 Method

S2.1.1 Contemporaneous Fire Weather

In this edition of the report, we introduce routine summaries of the extreme (95th percentile) fire weather days during the March 2024–February 2025 global fire season based on the fire weather index (FWI), a common metric of fire danger developed by the Canadian Forest Service as part of the Canadian Forest Fire Danger Rating System (CFFDRS) (van Wagner, 1987). The FWI comprises various components that consider the influence of weather on fire danger, with 2m temperature, 10m wind speed, precipitation, and 2m relative humidity as prerequisite variables. Higher FWI values are generally seen during droughts and heatwaves but they are more broadly indicative of meteorological conditions more conducive to wildfires in environments with sufficient fuel load (Di Giuseppe et al., 2016; Jones et al., 2022).

We base our analysis of extreme (95th percentile) fire weather on the FWI dataset derived from the Copernicus Climate Change Service ERA5 reanalysis (Hersbach et al., 2023; Vitolo et al., 2020) and maintained by the Copernicus Emergency Management Service (CEMS, version4.1 2019). This dataset provides global fire weather data at a 0.25° spatial resolution and daily temporal resolution. To identify extreme fire weather conditions, we computed the 95th percentile of daily FWI values at 0.25° resolution over the reference period March 1978–February 2025 (i.e., covering 46 fire seasons). For each fire season, we then calculated the number of days on which the daily FWI exceeded this threshold, yielding our estimate of extreme fire weather days, referred to as FWI_{95d}—defined as the annual number of days when fire weather conditions surpass the 95th percentile threshold.

Anomalies in FWI_{95d} for the March 2024–February 2025 fire season were subsequently calculated following the same methodology used for the observational fire variables, and are presented as (i) ranks, (ii) proportional anomalies, and (iii) standardised anomalies (see **Section 2.1.2.1**). The data produced using these methods are available from (Turco et al., 2025).

We adopt FWI_{95d} as our metric for extreme fire weather for several reasons. First, FWI_{95d} focuses on periods of high fire danger, when fire ignition and rapid spread are more likely (e.g. Barbero et al., 2014). Second, it has been widely used in previous studies assessing fire–climate relationships (Abatzoglou et al., 2019; Jones et al., 2022; Quilcaille et al., 2023), supporting consistency with the broader literature. Third, and crucially for a global analysis, the use of a quantile-based threshold reduces the impact of regional biases in absolute FWI values, allowing for a more robust comparison of fire weather extremes across geographically diverse environments.

S2.1.2 21st Century Trends in Burned Area

To place recent extremes in the context of fire trends of the past two decades, we update our regional analyses of trends in annual BA from Jones et al. (2022). In contrast, we present trends that align more closely with global fire seasons, spanning the period March 2002-February 2025 rather than trends over calendar years. We quantified trends using the Theil-Sen slope estimator, which is useful when data may contain outliers or be non-normally distributed making it less sensitive to outliers than a standard least squares regression slope. Changes were calculated by multiplying trends (unit year[-1]) by the number of fire seasons in the period of coverage for each variable (**Section 2.1.1.2**). Relative changes were calculated

167 as the absolute changes divided by the mean annual BA during the period following (Andela
168 et al., 2017; Jones et al., 2022). The significance of trends was evaluated using the Mann-
169 Kendall test, with a confidence level set at 95%.
170
171 In addition to reporting trends in *total* BA, we also present trends in *forest* BA as these regularly
172 diverge from total BA trends, following Jones et al. (2024a) see **Section 2.2.2**). Forest BA is
173 calculated as described in **Section 2.1.1,** but after isolating burned cells in areas with tree
174 cover exceeding 30% in NASA's annual MODIS MOD44B collection 6.0 Continuous
175 Vegetation Field product (250m; Dimiceli et al., 2015). The 30% threshold is widely used
176 amongst studies of forest cover change (Cunningham et al., 2020; e.g. Li et al., 2017; Sexton
177 et al., 2016).
178

S2.2 Results

S2.2.1 Contemporaneous Fire Weather

183 **Section 4** of this report comprehensively explores the drivers of the extreme fire season for 4
184 selected events during 2024-25, not only in terms of meteorological factors influencing the
185 preconditioning of vegetation fuels for fire but also including factors such as fuel loading, land
186 use and management, and ignition opportunities. However, because large-scale regional
187 patterns of drought and heatwave are known to influence fire extent (Abatzoglou et al., 2018;
188 Jolly et al., 2015; Jones et al., 2022), we briefly summarise here the meteorological
189 circumstances underlying some of the regional extremes of the 2024-25 fire season identified
190 above. Robust relationships are observed between fire weather and fire activity in regions with
191 ample fuels across multiple decades, particularly in forests (Abatzoglou et al., 2018; Jones et
192 al., 2022, 2024a; Turco et al., 2018).
193
194 **Figure S2** shows world regions experiencing high levels of extreme fire weather during the
195 2024-25 fire season (data are available from Turco et al., 2025). Extreme fire weather was
196 notably prevalent in the majority of regions in tropical South America, with the highest number
197 of fire weather days on record in most states of Brazil, Bolivia and Peru and many other states
198 of Colombia, Venezuela, and the Guianas experiencing a high-ranking–if not record-breaking–
199 number of days with extreme fire weather. For example, Amazonas State in Brazil experienced
200 more than 50 additional days of extreme fire weather than its annual mean and many regions
201 saw more than a month of additional fire weather days than is the average year (**Figure S2**).
202 The spatial pattern of fire weather anomalies (**Figure S2**) clearly aligns with the elevated fire
203 activity across the Amazon, broader moist tropical forests, Pantanal, and Chiquitano regions
204 of South America during 2024-25 (**Figure 2, Figure 3**). Similarly, Mesoamerica experienced
205 an unusually high number of extreme fire weather days during 2024-25 (**Figure S2**) and this
206 is likely one factor contributing to higher than average fire activity in parts of Mexico during
207 2024-25 (**Figure 2**, **Figure 3**).
208
209 In Canada, some anomalies in extreme fire weather were observed in the northernmost
210 provinces of western Canada (e.g. Northwest territories) and some eastern provinces during
211 2024-25 (**Figure S2**). Although anomalies in BA and C emissions were indeed centred on the
212 same regions of Canada, we note that the anomalies in extreme fire weather days were fairly
213 small and overall less widespread than the anomalies in BA and C emissions. This evidence
214 points towards other factors (beyond contemporaneous fire weather) as drivers of the elevated
215 fire activity during 2024-25, potentially including the carryover effects of the prior-year
216 heatwave and drought from 2023 and of overwintering ignitions from smouldering peat
217 combustion (Scholten et al., 2021).
218
219 In Africa, widespread high fire weather was observed across the Congo basin during the 2024-
220 25 fire season (**Figure S2**), aligning strongly with the anomalous BA and fire C emissions

221 observed in the region (**Figure 2, Figure 3**). In Southern Africa, extreme fire weather
222 anomalies were widespread (**Figure S2**) but also characteristically decoupled from anomalies
223 in BA (**Figure 2**) due to the inverted relationship between fire weather and fire activity in this
224 fuel-limited region, where fire weather tends to correlate with poor vegetation productivity
225 (Jones et al., 2022).
226
227 In Eastern Europe, anomalies in extreme fire weather were centred on Ukraine and the Balkan
228 states (**Figure S2**), corresponding with BA and C emissions anomalies in some parts of
229 Ukraine, Serbia, and North Macedonia (**Figure 2**, **Figure 3**). However, spatial relationship
230 between extreme fire weather and extreme fire activity was not direct in neighbouring regions,
231 with western Turkey (for example) experiencing above-average BA and emissions (**Figure 2**,
232 **Figure 3**) despite no clear anomaly in extreme fire weather (**Figure S2**). Similarly, anomalies
233 in extreme fire weather spanned much of southern and southeast Asia (**Figure S2**), yet
234 positive anomalies in BA and fire C emissions emerged in northern India, Nepal and
235 Bangladesh but not in nearby parts of Thailand, Cambodia and Myanmar (**Figure 2**, **Figure
236 3**). In Siberia, a record-breaking number of extreme fire weather days occurred during the
237 2024-25 fire season (**Figure S2**) but did not translate into especially high BA or fire C
238 emissions (**Figure 2**, **Figure 3**). This is a somewhat surprising finding for this region, given
239 that the most extreme fire seasons of 2020 and 2021 were previously linked with extreme fire
240 weather associated with heatwave and drought (Zheng et al., 2023).
241
242 Overall, these findings highlight that there is noise in the relationship between fire weather and
243 BA, with extreme fire weather preconditioning vegetation to burn but a variety of other factors
244 such as ignition availability, fuel loading, and management factors driving dissociation in
245 certain regions and years. For certain focal events, **Section 4** formally evaluates the role of
246 fire weather's sub-components (temperature, precipitation, humidity and wind speed) as
247 drivers of fire alongside non-meteorological factors.
248
249 **S2.2.2 21st Century Trends in Burned Area**
250
251 The anomalies of 2024-25 occur against a backdrop of trends in BA this century that point
252 towards shifts in fire regime. **Figure S3** shows significant trends in BA and forest BA across
253 the fire seasons in the period March 2002-February 2025 derived from MODIS BA data. While
254 many world regions are experiencing declines in total BA, increases in forest BA are far more
255 prevalent than declines at the scale of continental biomes, countries, and administrative
256 regions.
257
258 In South America, trends in total and forest BA are varied. The more than doubling of both
259 total and forest BA in Amazonas (significant at $p<0.05$; **Figure S3**), among the most pristine
260 parts of Amazonia, contrasts with the neighbouring state of Pará, where total BA has fallen by
261 44% ($p<0.05$) as deforestation rates and deforestation-related fires have broadly declined
262 since their peak during the early 2000s (Mataveli et al., 2025). The anomalous fire activity and
263 C emissions in Amazonas state during the 2024-25 fire season is consistent with the emerging
264 pattern of increased fire extent within in the state, whereas in Pará and other regions of South
265 America's tropical forests, the 2024-25 anomaly punctuates the either reducing or stable BA
266 trends of recent decades.
267
268 More broadly across the tropics, total BA has reduced across many savannah regions of
269 Africa, South America, and northern Australia (**Figure S3**). The low fire seasons of 2024-25
270 and 2023-24 in the African savannahs (**Section 2.2.1.2**) are highly consistent with the decline
271 in BA seen in those regions this century. In tropical forests, BA has generally fallen in
272 Southeast Asia, increased in the Congo basin, and shown no significant trend in South
273 America. Hence, fires in the tropics do not show a consistent global trend (**Figure S3**). Notably,
274 the BA anomalies seen in the Congo basin during the 2024-25 fire season appear to be an

extension of a trend towards increased BA across in the region over recent decades (**Figure S3**).

Northern hemisphere extratropical regions in North America and Asia show a clear pattern of increased forest BA since 2002 (**Figure S3**), which is also visible on national scales in Canada and the US and on state/provincial scales in various states of western and eastern Canada, the western US, and northeast Russia. The consecutive large anomalies in BA in Canada during 2023-2024 and 2024-25 align with the doubling of forest BA seen in Canada across fire seasons since 2002 (significant trend, $p < 0.05$) and a 22% increase in total BA in Canada (marginally significant at $p < 0.1$). Three Canadian provinces showed significant increases in both total and forest BA this century: British Columbia (+39-49%); Northwest Territories (+52-80%), and; Yukon (+75-141%). No Canadian provinces experienced a significant decline in forest BA or total BA. More widely, there was a 51% increase in forest BA in the North American boreal forest biome since 2002, and a 118% increase across the pan-boreal forest biome of North America and Eurasia. The succession of events affecting boreal forests in Canada in 2023 and 2024, Siberia in 2020, and both North America and Siberia during 2021 are part of a continued trend towards rising fire extent in high latitude forests this century (Jones et al., 2024a).
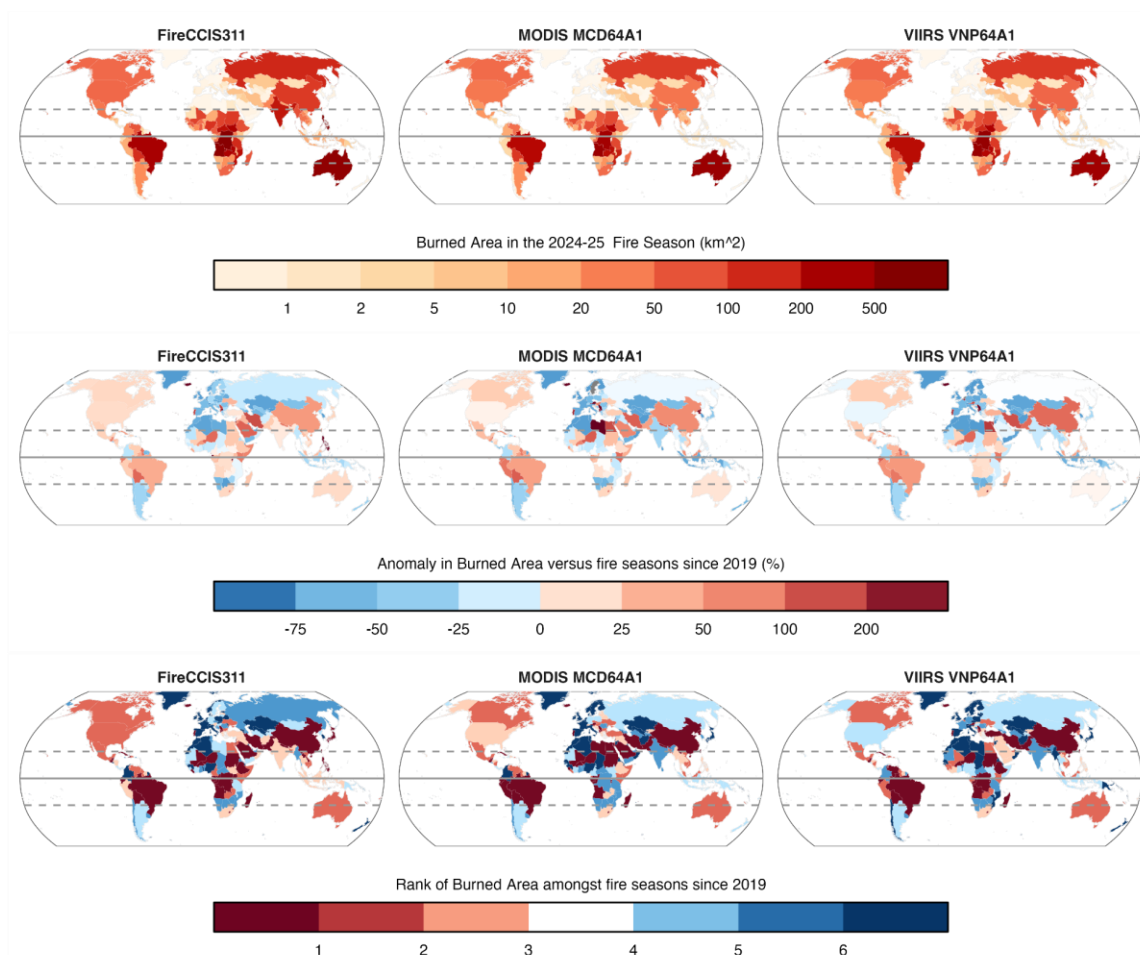
Figure S1: Comparison of the burned area (BA) estimates from **(left column)** the ESA Climate Change Initiative FireCCI product Sentinel-3 SYN Burned Area Grid product, version 1.1 (Chuvieco et al., 2024; FireCCIS311; Lizundia-Loiola et al., 2022), **(middle column)** the VIIRS BA product produced by NASA (VNP64A1 v002) (Giglio, 2024; Zubkova et al., 2024) and **(right)** the MODIS BA product produced by NASA (MCD64A1 collection 6.1; Giglio et al., 2018).
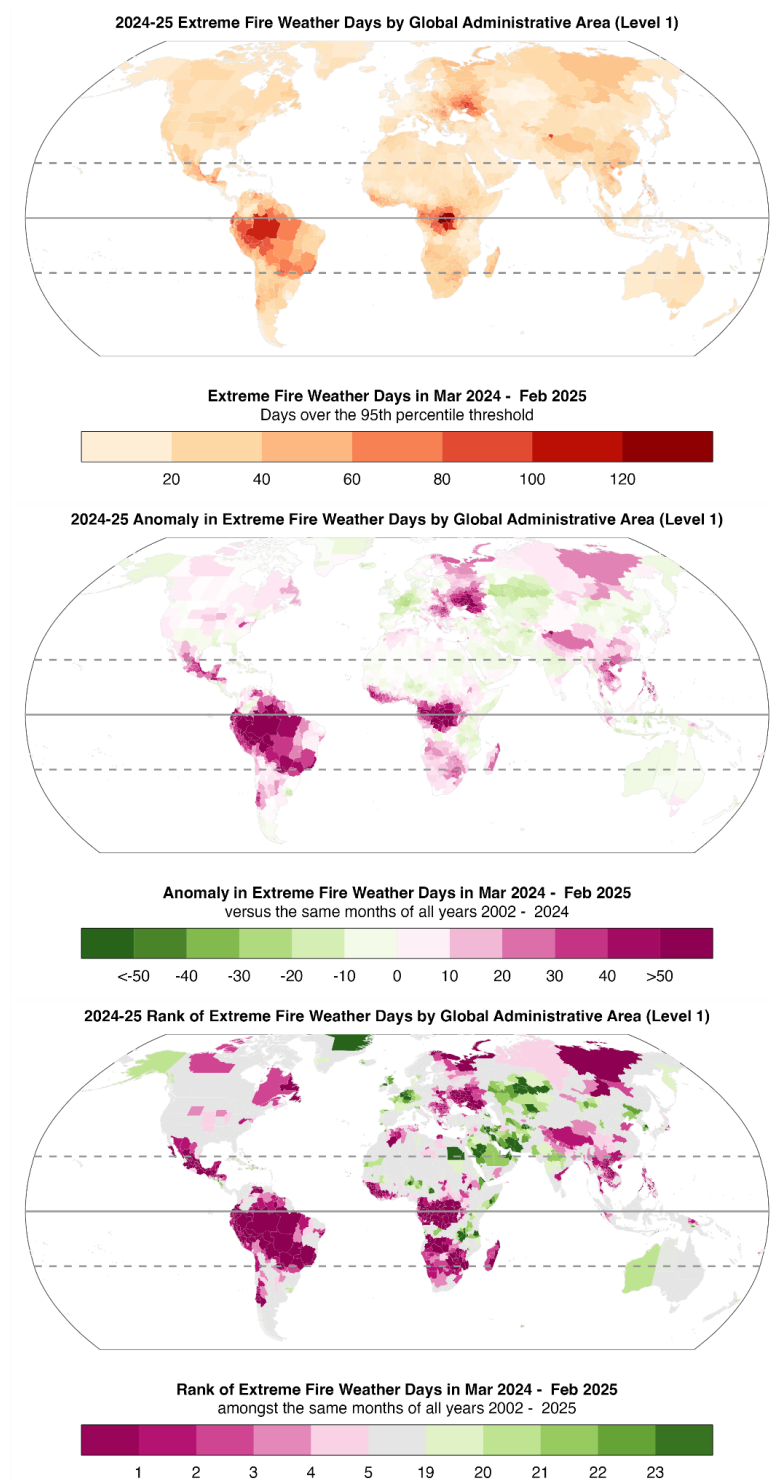
301
Figure S2: Extreme fire weather in the past fire season, including **(top panel)** the number of days with extreme (95th percentile) fire weather during the 2024-25 fire season, **(middle panel)** the anomaly versus the mean of all prior fire seasons 2002-2024, and **(bottom panel)** rank amongst all fire seasons since 2002.
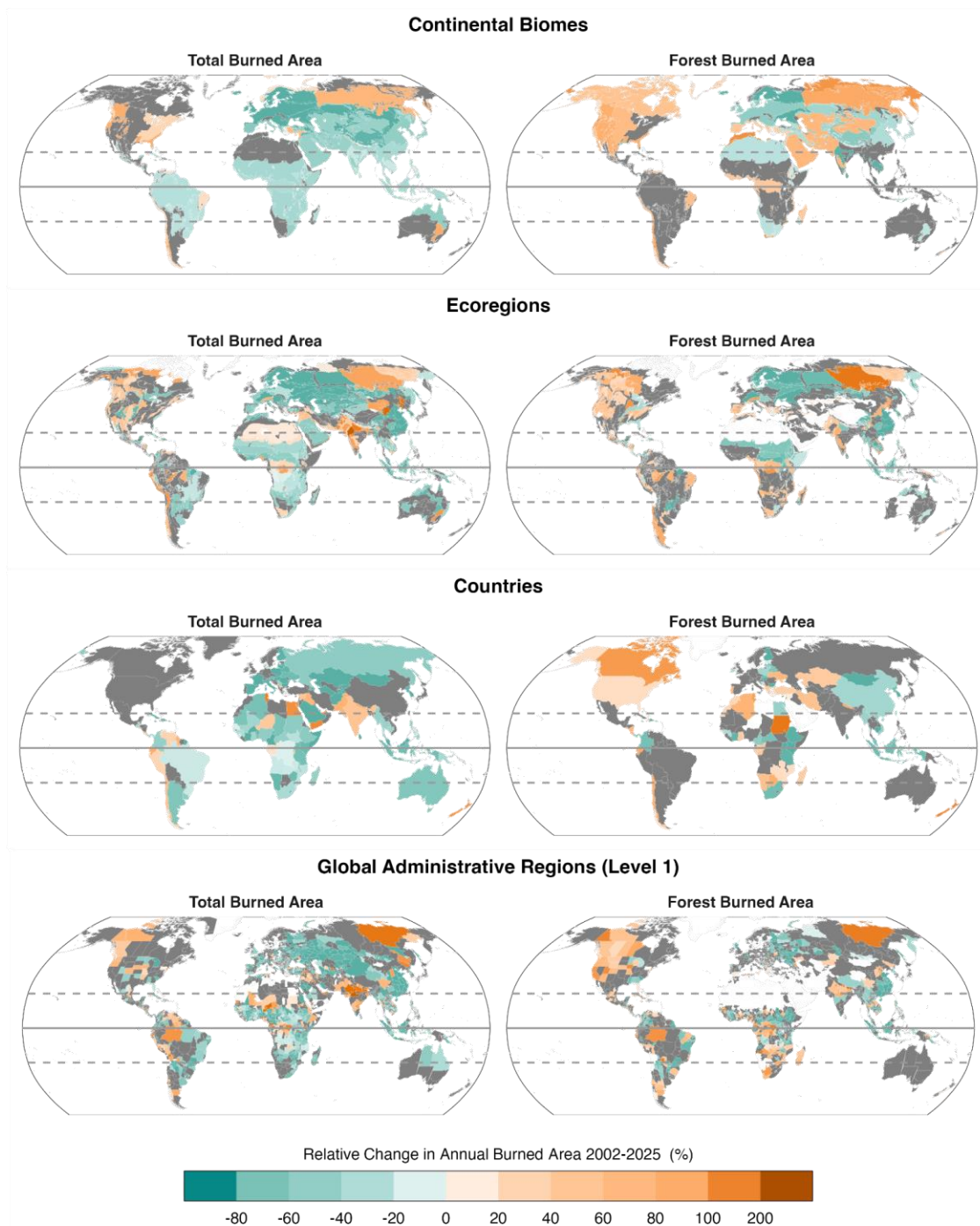
Figure S3: Relative changes (%) in **(left panels)** total annual BA and **(right panels)** forest BA across March-February fire seasons during 2002-2025 for three regional layers: **(top panels)** continental biomes; **(middle panels)** countries, and; **(bottom panels)** level 1 administrative regions (e.g. states or provinces). Forest BA considers only areas with tree cover over 30% at the native (500 m) resolution of the BA observations. Relative changes are calculated as the trend in BA across fire seasons March 2002-February 2003 through March 2024-February 2025 multiplied by the number of years in the time series and divided by the mean annual BA during the period. Trends in BA are derived using the Theil-Sen slope estimator. Only significant trends in BA are shown (dark grey fill signifies no significant trend).

316

318
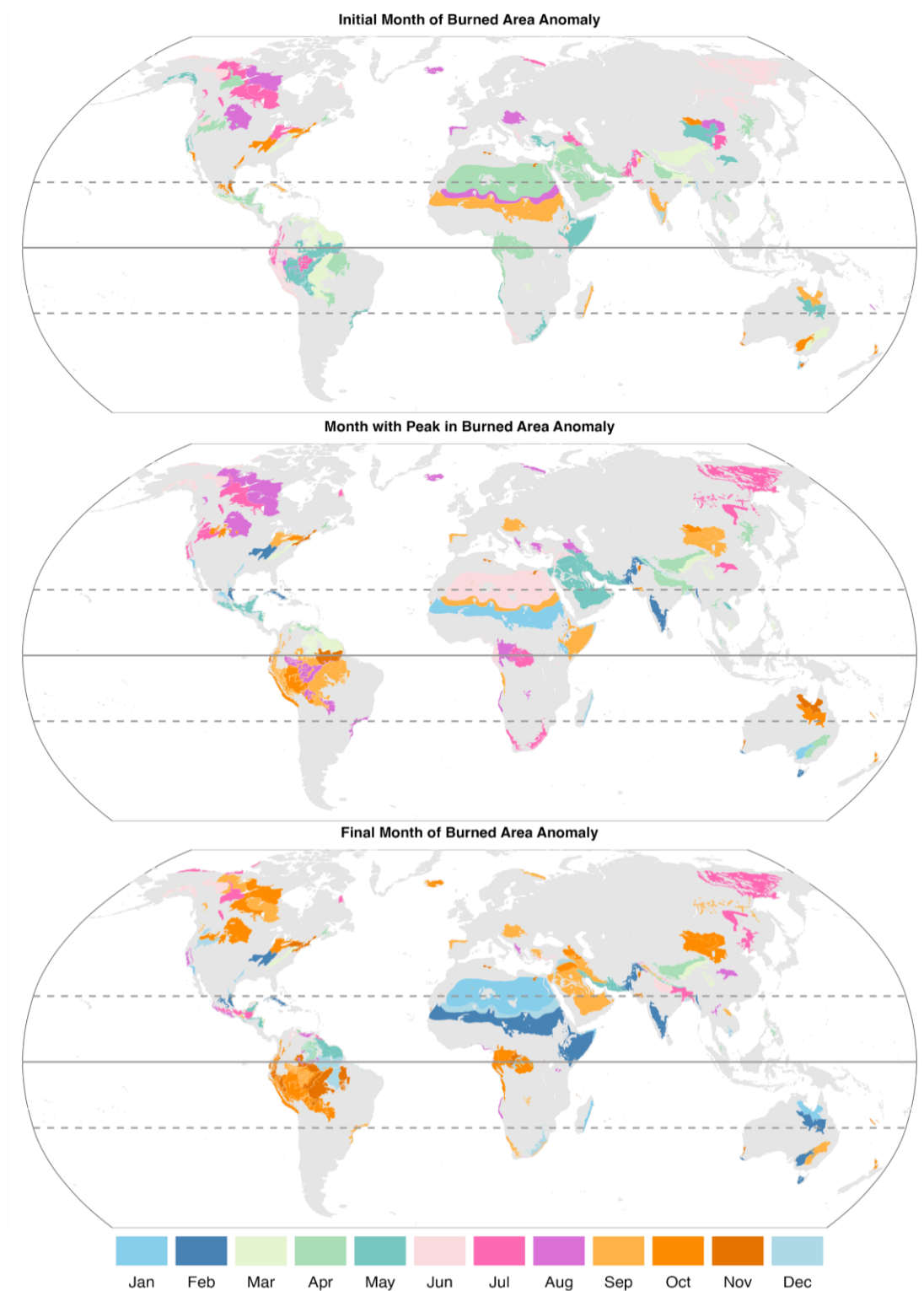
319
320 **Figure S4: (Top panel)** first month, **(middle panel)** peak month, and **(lower panel)** final
321 month of positive BA anomalies at Global Administrative Level 1 during March 2024-February
322 2025. Peak anomalies are identified relative to the monthly climatology in 2001-2024. The first
323 and final months of the BA anomaly incorporate the period when BA was continuously above
324 the climatological mean. Graduated colours are separated seasonally.
325
326

Northeast Amazonia Burnt Area Anomaly Sep 23 - Feb 25

Burned Area (% burnable land)
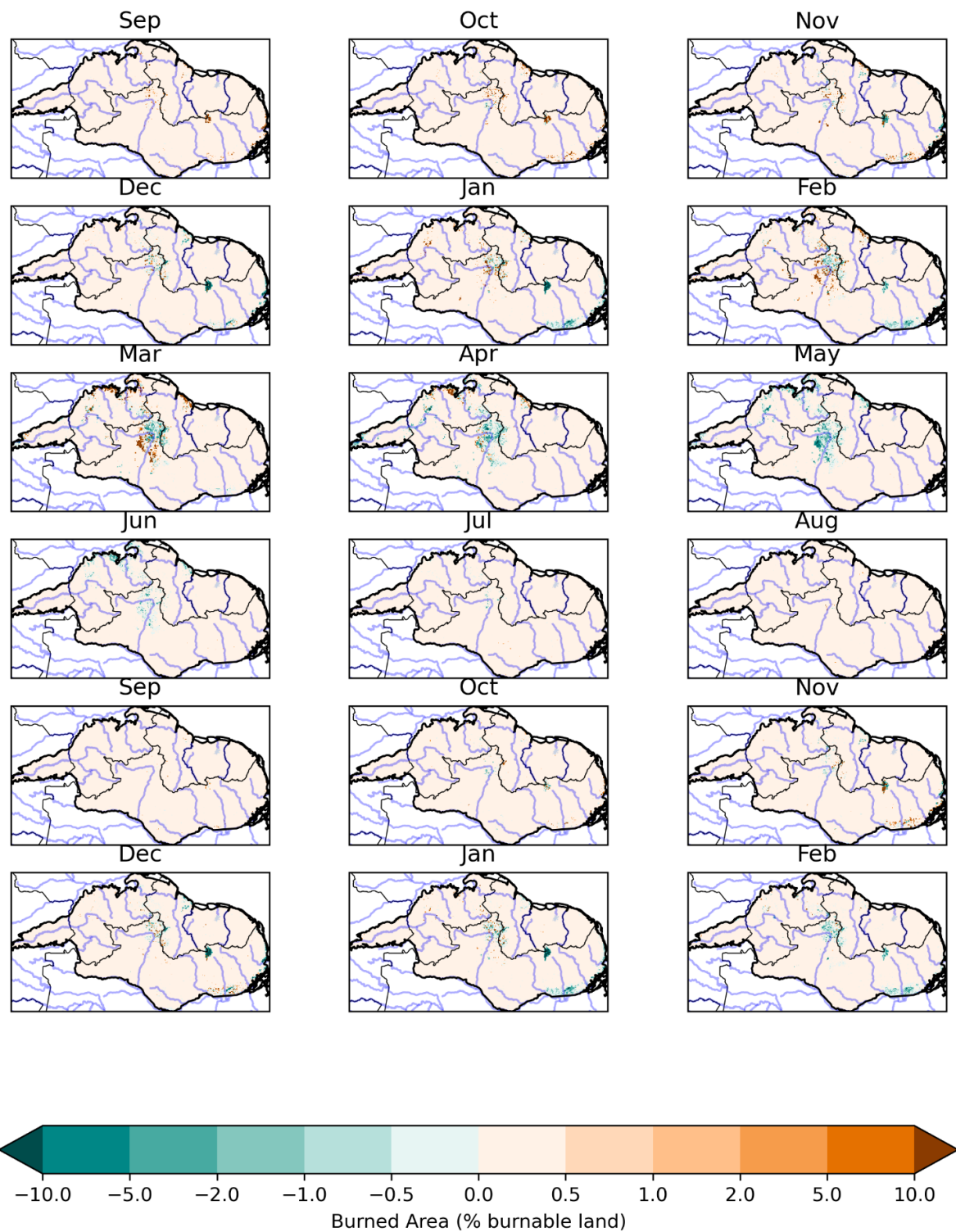
Figure S5: Monthly anomalies in absolute BA fraction (unit: additional % of cell area burned) at 0.25° for Northeast Amazonia throughout the 2024-25 fire season compared with the 2001-2024 climatological mean.

332

Pantanal & Chiquitano Burnt Area Anomaly Sep 23 - Feb 25

333

334
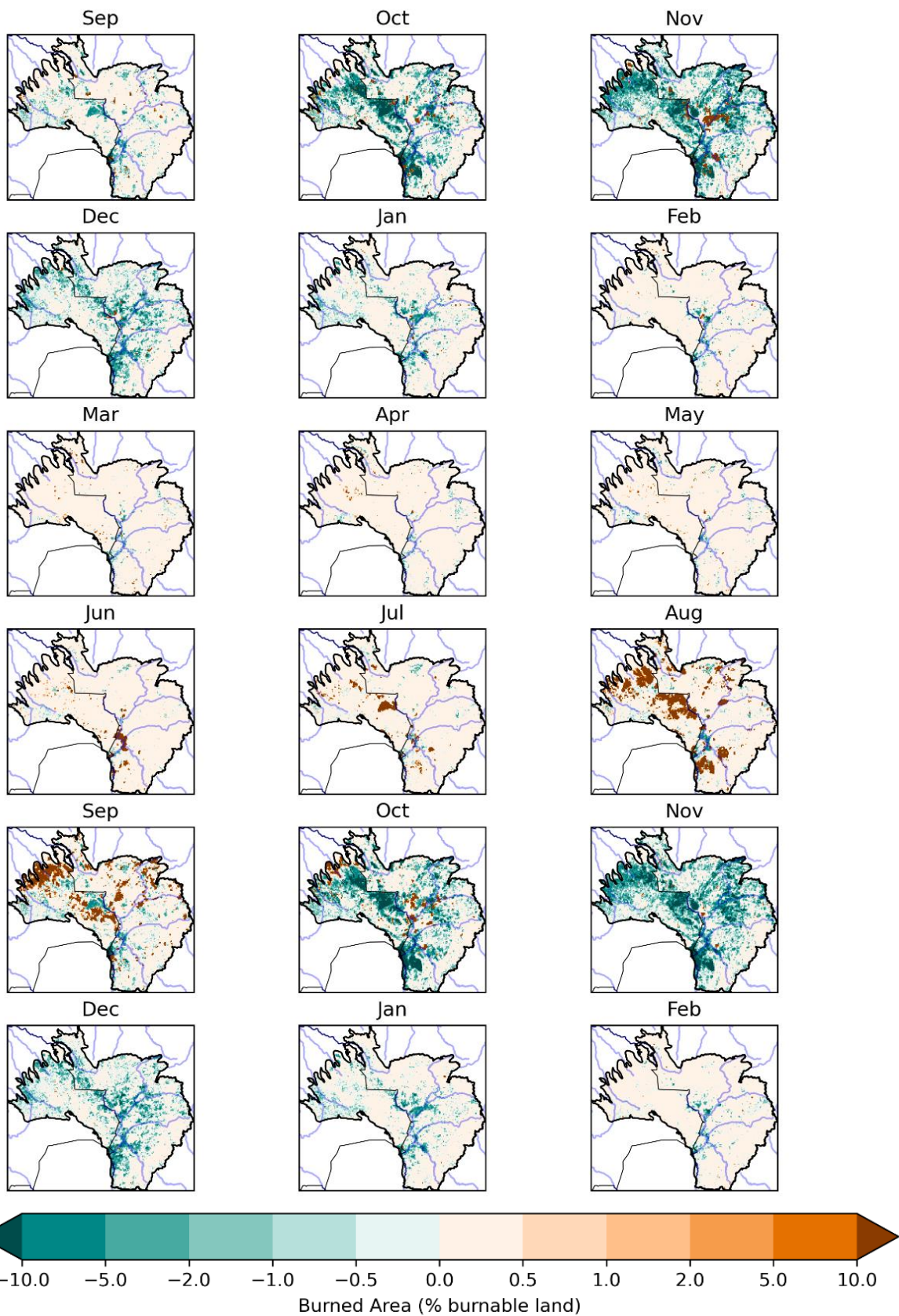
Figure S6: Same as **Figure S5** but for the Pantanal & Chiquitano.

335

336

Southern California Burnt Area Anomaly Sep 23 - Feb 25
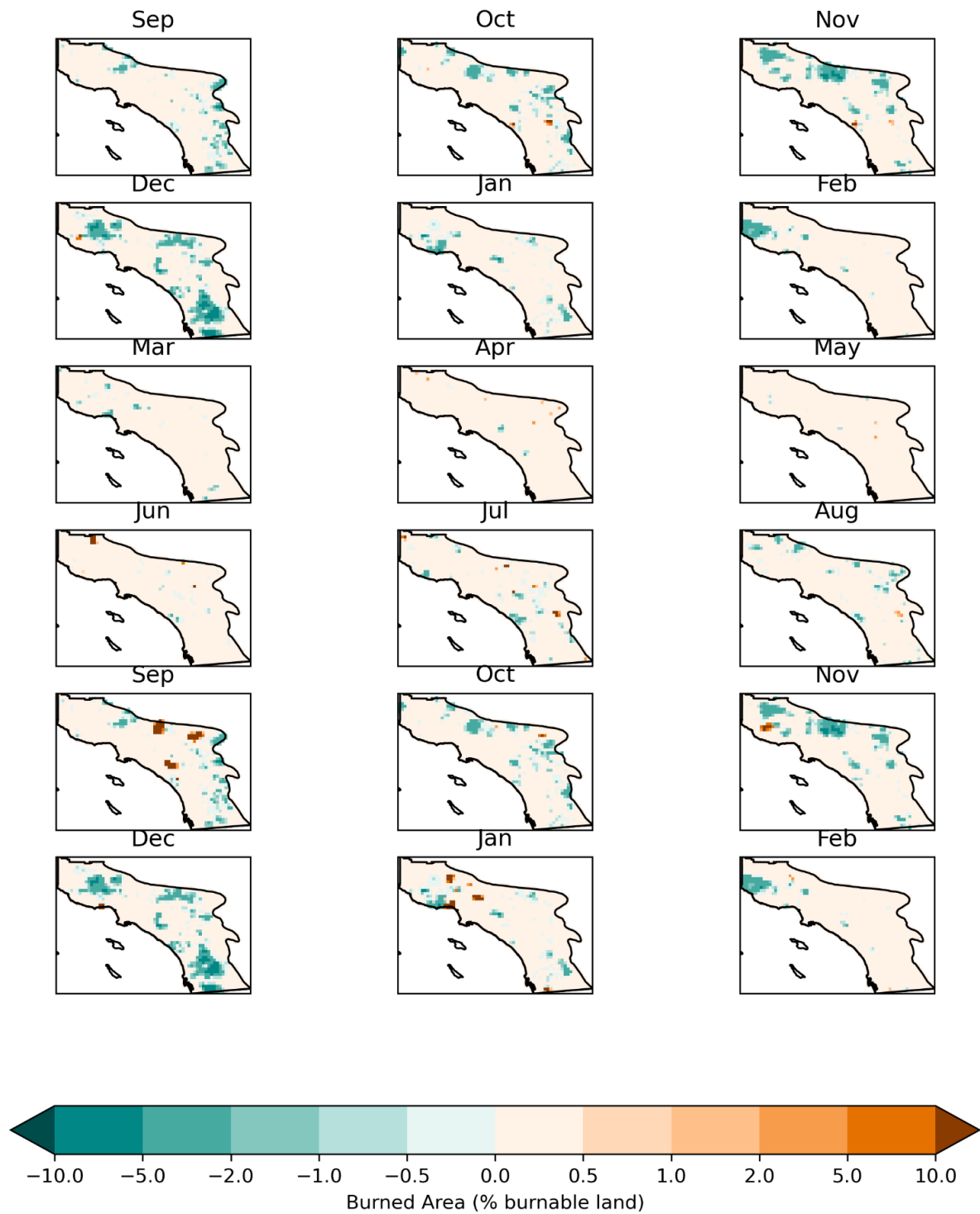
338 **Figure S7:** Same as **Figure S5** but for Southern California.

Congo Basin Burnt Area Anomaly Sep 23 - Feb 25

Burned Area (% burnable land)
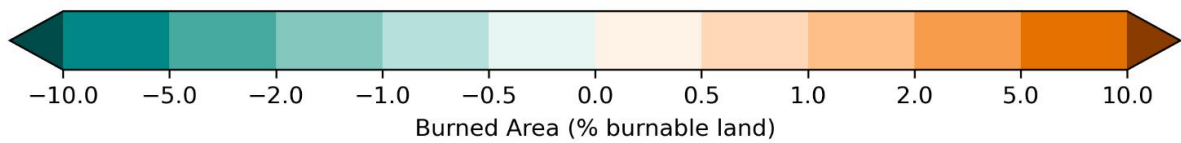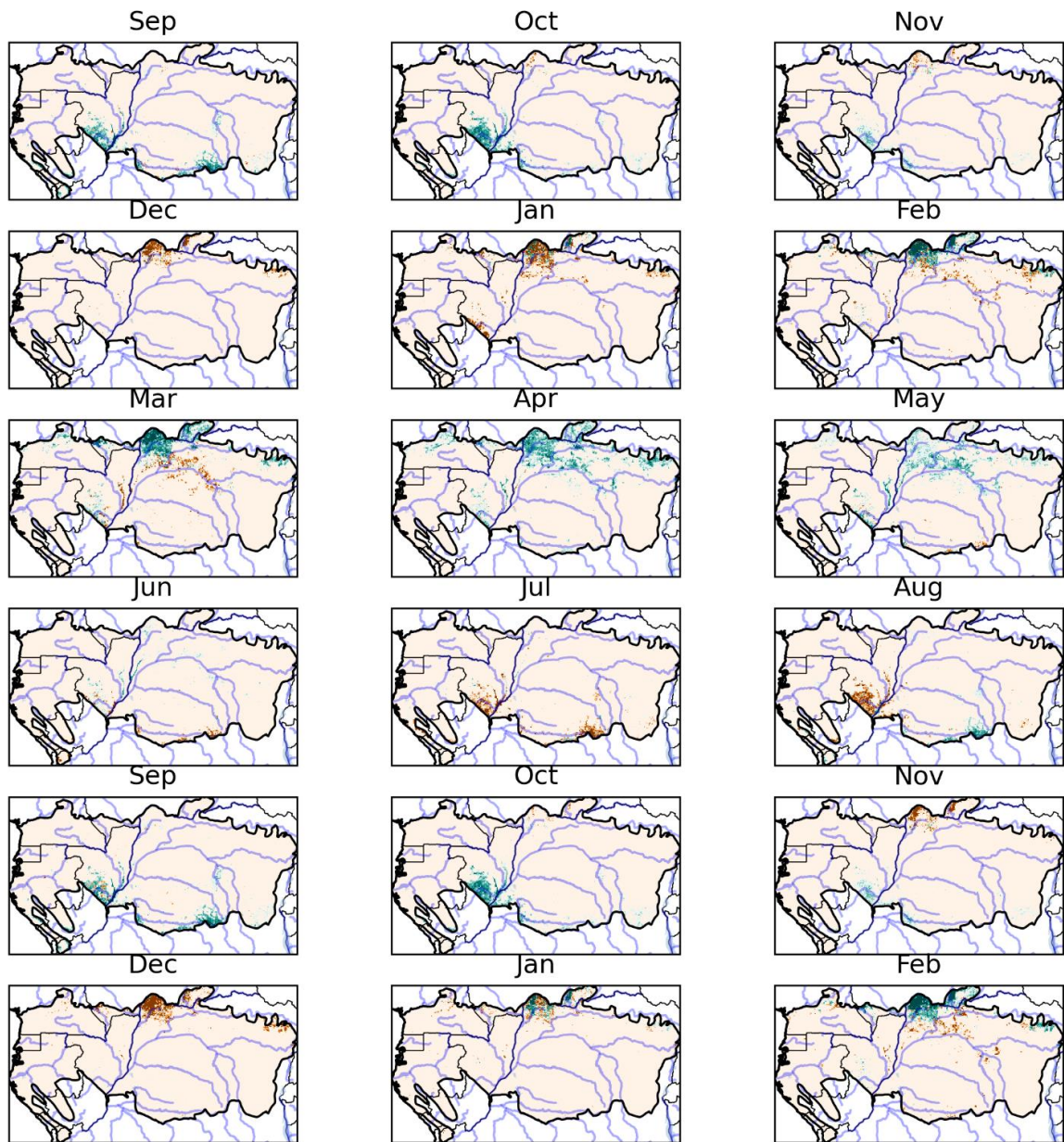
Figure S8: Same as **Figure S5** but for the Congo Basin.

S3 Supplementary Material for Section 3
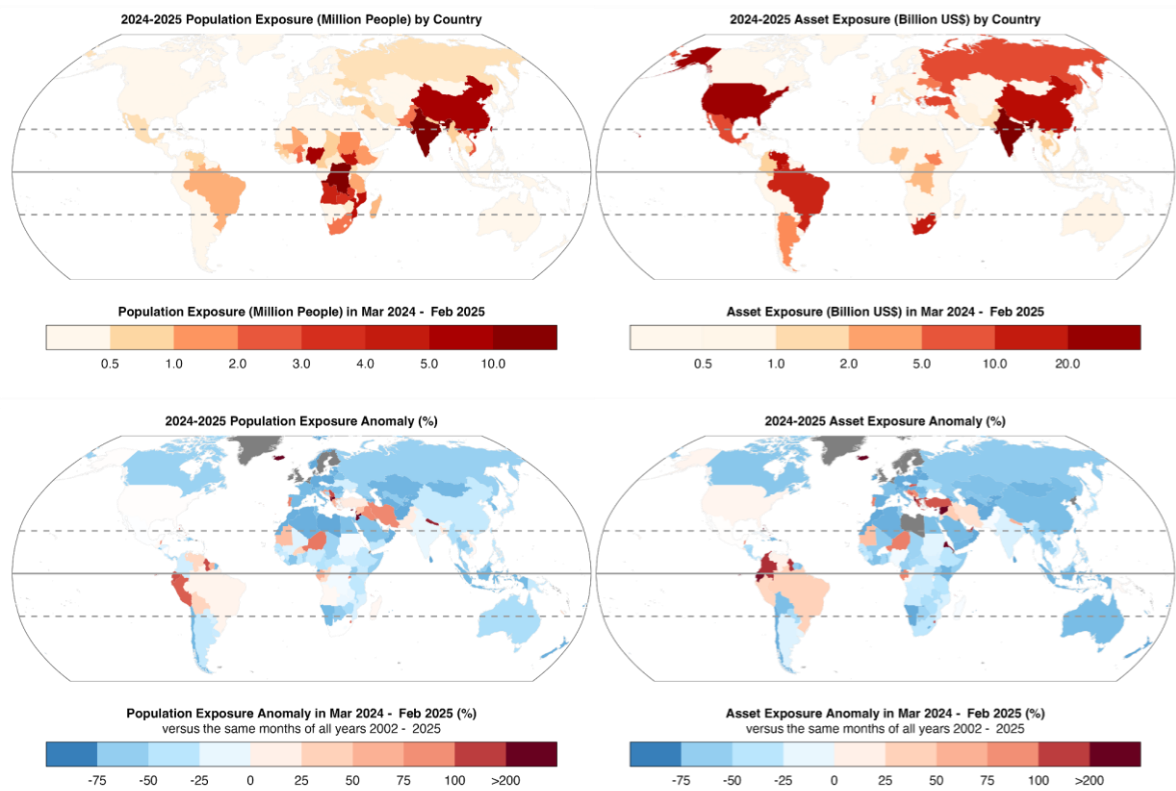
Figure S9: (left panels) Population and **(right panels)** physical assets exposed to burned area (BA) during the 2024-25 global fire season. The figure shows **(top panels)** the number of people or the asset value (billion US$) exposed to fire and **(bottom panels)** the relative anomaly versus all years since 2002.
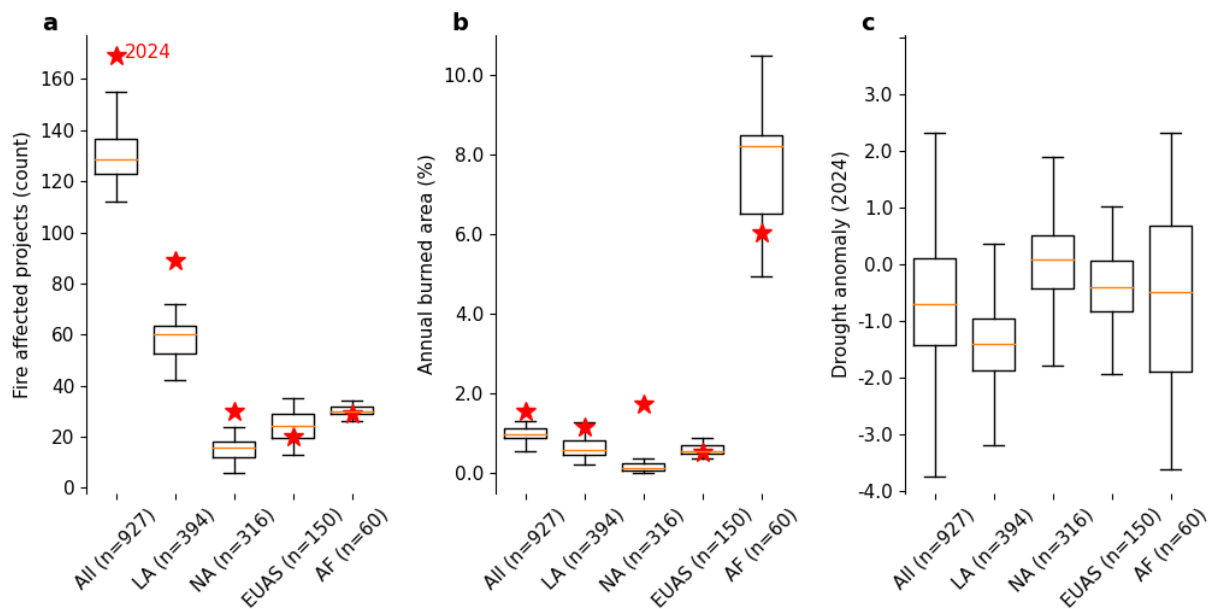
Figure S10: Exceptional 2024 fire activity in carbon projects can be explained by regional drought extremes and a long-term increase in drought and forest fire risk. (a) Number of projects with burned area (BA) in each year, (b) average annual percentage of project area burned, (c) 2024 drought anomaly for all projects (12-month SPEI; negative values indicate drier conditions). In (a) and (b), the red star indicates the 2024 ranking among other years. Data are shown for all projects (all), Latin America (LA), northern America (NA), Eurasia (EUAS), and Africa (AF).

S4 Supplementary Material for Section 4

S4.1 Methods

S4.1.1 Probability of Fire

To model the probability of active fire occurrence at high spatial and temporal resolution, Sparky is trained on daily, gridded observations of satellite-detected active fires from the MCD14ML fire location product, produced by the University of Maryland (Giglio et al., 2020). This dataset contains point-based fire detections from the MODIS instruments aboard the Terra and Aqua satellites. We first aggregated these fire detections onto the model's regular latitude–longitude grid at approximately 9 km resolution, using a daily time step. For each grid cell and day, the target variable was assigned a binary value: 1 if at least one MODIS active fire detection was present in that cell on that day, and 0 otherwise. The model was then trained to predict the probability of observing at least one active fire in a given grid cell on a given day. After training, we applied the model globally to generate daily, grid-based probability maps. While the model outputs the likelihood of at least one fire occurring per grid cell per day, we interpret the sum of predicted probabilities across all grid cells within a domain as an estimate of the expected number of active fire-affected grid cells. This interpretation is consistent with the probabilistic nature of classification outputs in ensemble tree models and is particularly suitable for modelling sparse events such as fire occurrence (Gneiting and Katzfuss, 2014).

379 **S4.1.2 ConFLAME**

380 ConFLAME (Controlar Fogo Local Analise pela Máxima Entropia, or "Local Fire Control
381 Analysis by Maximum Entropy' in English) is a probabilistic, control-based fire model designed
382 to evaluate and attribute burned areas under diverse climate and socio-environmental
383 scenarios. It directly builds upon the established ConFire and FLAME models (Barbosa et al.,
384 2025; Kelley et al., 2019, 2021), integrating ConFire's control-structured approach with
385 FLAME's Bayesian inference framework based on the Maximum Entropy principle. Full details
386 can be found in Barbosa et al. (submitted). ConFLAME is specifically developed for attribution
387 purposes, including compatibility with satellite-derived burned area data. This hybrid model
388 allows for spatially explicit, event-scale attribution, making it applicable across different
389 timeframes and regions. This means that, new to this year's report, our burned area (BA) driver
390 and attribution assessments can now target both high burned area zones within subregions
391 and the overall burned area across our entire focal region.

392 ConFLAME simulates monthly fractional burned area at grid-cell level using a set of
393 environmental and anthropogenic *controls*, each representing a key dimension of fire
394 regulation. These controls capture the limitations imposed by factors such as:

395 ● Fuel availability and continuity
396
397 ● Fuel dryness
398
399 ● Fire weather (including temperature and relative humidity)
400
401 ● Wind speed
402
403 ● Ignition sources (both natural and human-caused)
404
405 ● Fragmentation and suppression (e.g., from land use, roads, or firefighting)
406
407 ● Stochastic influences (unmodelled or residual variation)
408

409 Each control predicts the maximum possible burned area under ideal conditions for that
410 specific factor. For instance, the "fuel dryness" control estimates the area that *could* burn if all
411 other factors, such as fuel, ignition or suppression, impose no limitations. These controls are
412 derived as linear combinations of their respective drivers (see Table S1 for assignment
413 details), which are then transformed using the logistic function to produce a value between 0
414 and 1. The individual control outputs are multiplied together to give a final burned area
415 estimate, capturing the combined effects of all constraints (Kelley et al., 2021). This
416 multiplicative structure allows interactions between drivers to influence fire outcomes and
417 accommodates compound extremes where multiple drivers align to produce extreme BAs. As
418 per Barbosa et al. (2025), this BA is corrected for sub-grid spatial/temporal autocorrelation
419 that may alter overall fire spread and therefore BA.

420 ConFLAME uses a Bayesian inference approach following a similar protocol to (Barbosa,
421 2024). We use the PyMC (v5) Python package with the Metropolis-Hastings MCMC sampler
422 (Hoffman and Gelman, 2011). Optimisation runs over 10 parallel chains with 1,000 tuning and
423 1,000 sampling iterations per chain to determine the probability distribution of model
424 parameters, such as those describing driver combination control strength and BA
425 autocorrelation. The model employs a Maximum Entropy update function to avoid
426 unnecessary assumptions beyond data constraints (Barbosa et al., 2025). Training utilising
427 50% of the data or a minimum of 4000 grid cells. Instead of a single outcome. This approach
428 produces a full distribution of possible burned area results for each grid cell and month,

429 capturing uncertainty in parameters and fire variability. This allows rare but plausible
430 outcomes, such as unusual BA levels, to emerge when multiple conditions favour fire.

431 Once trained, ConFLAME is run in large ensembles to approximate the posterior BA
432 probability distributions:

433 ● For attribution experiments (e.g., climate vs human vs combined forcing), we randomly
434   sample 400 simulations from each chain (so 4000 samples), each using parameter
435   samples drawn from the posterior distribution. For climate or human attribution, we pair
436   each of these with an additional sample using counterfactual (either without
437   anthropogenic forcing, without climate change or without people) inputs.
438

439 ● For future projections, a smaller ensemble of 1000 sampled (100 for each chain)..
440

441 ● As per (Barbosa, 2024), for evaluation we trained the first half of the period and test
442   on the second half using 1000 samples. For the rest of the results, we trained on the
443   full period.

444 Each simulation in the ensemble represents one possible realisation of fire behaviour,
445 conditioned on a plausible combination of parameters and driver inputs. The ensemble as a
446 whole approximates the posterior distribution of burned area for each grid cell and time step.

447 When analysing outputs across time (e.g., seasonal totals) or space (e.g., regional
448 aggregates), probability metrics (mean, median, percentiles) are computed per ensemble
449 member first, and then the distribution of these metrics is used to reconstruct a consistent
450 posterior for the aggregated quantity. This preserves the dependencies within each realisation
451 and avoids artificial narrowing of uncertainty that would result from averaging across
452 distributions rather than ensembles.

453

454 **Table S1:** Overview of predictors used in the two fire attribution models (PoF and ConFLAME).
455 Predictors are grouped into four control categories. ✓ indicates inclusion in the model, with (+)
456 or (−) signs representing positive or negative influence over fire occurrence in ConFLAME.
457 Resolution and temporal coverage refer to the dataset version used during model training.

Category	Predictor	PoF	Con-FLAME (section 4)	Con-FLAME (section 5)	Spatial Resolution	Temporal Coverage	Reference
Weather	2m Temperature	✓	✓ (+)	✓ (+)	~9 km (0.1°)	2003–2025	(Muñoz-Sabater et al., 2021)
	2m Dewpoint Temperature	✓	✓ (−)	✗	~9 km (0.1°)	2003–2025	(Muñoz-Sabater et al., 2021)
	Relative Humidity	✗	✗	✓ (−)	(0.25°)	2003–2025	(Muñoz-Sabater et al., 2021)
	10m Wind Speed	✓	✓ (+)	✓ (+)	~9 km (0.1°)	2003–2025	(Muñoz-Sabater et al., 2021)
	Precipitation	✓	✓ (−)	✓ (−)	~9 km (0.1°)	2003–2025	(Muñoz-Sabater et al., 2021)
Fuel	Live Leaf Fuel Load	✓	✓ (+)	✓ (+)	~9 km (0.1°)	2003–2025	(McNorton and Di Giuseppe, 2024)
	Live Wood Fuel Load	✓	✓ (+)	✓ (+)	~9 km (0.1°)	2003–2025	(McNorton and Di Giuseppe, 2024)
	Dead Foliage Fuel Load	✓	✓ (+)	✓ (+)	~9 km (0.1°)	2003–2025	(McNorton and Di Giuseppe, 2024)
	Dead Wood Fuel Load	✓	✓ (+)	✓ (+)	~9 km (0.1°)	2003–2025	(McNorton and Di Giuseppe, 2024)
	LAI – Low/High Vegetation	✓	✓ (+)	✓ (+)	~9 km (0.1°)	2003–2025	(Boussetta et al., 2021)
	Live Fuel Moisture Content	✓	✓ (−)	✗	~9 km (0.1°)	2003–2025	(McNorton and Di Giuseppe, 2024)
	Dead Foliage Moisture Content	✓	✓ (−)	✗	~9 km (0.1°)	2003–2025	(McNorton and Di Giuseppe, 2024)

	Dead Wood Moisture Content	✓	✓ (–)	✗	~9 km (0.1°)	2003–2025	(McNorton and Di Giuseppe, 2024)
Ignition	Pasture Fraction	✗	✓ (+/–)	✓ (+/–)	~25 km (0.25°)	2007–2025	(Klein Goldewijk et al., 2010)
	Cropland Fraction	✗	✓ (+/–)	✓ (+/–)	~25 km (0.25°)	2007–2025	(Klein Goldewijk et al., 2010)
	Urban Population	✗	✓ (+/–)	✓ (+/–)	~25 km (0.25°)	2007–2025	(Klein Goldewijk et al., 2010)
	Rural Population	✗	✓ (+/–)	✓ (+/–)	~25 km (0.25°)	2007–2025	(Klein Goldewijk et al., 2010)
	Population Density	✓	✗	✗	~9 km (0.1°)	2005, 2010, 2015, 2020	(Center for International Earth Science Information Network (CIESIN), 2025)
	Road Length	✓	✗	✗	~9 km (0.1°)	2015	(Meijer et al., 2018)
	Cloud-to-ground lightning	✗	✓ (+)	✓ (+)	~25 km (0.25°)	2019-2025	(Qu et al., 2025)
	Lightning	✓	✗	✗	~9 km (0.1°)	2019-2025	(Lopez, 2016)
	Vegetation Type	✓	✗	✗	~9 km (0.1°)	2003-2021	(Boussetta et al., 2021)
	Urban Fraction	✓	✗	✗	~9 km (0.1°)	2010	(McNorton et al., 2023)
	Orography	✓	✗	✗	~9 km (0.1°)	Static	(Boussetta et al., 2021)
Missed Prediction Term		✓	✓	✓	Model-defined	2007–2025	(Barbosa et al., 2025) This study

458

S4.2 Results
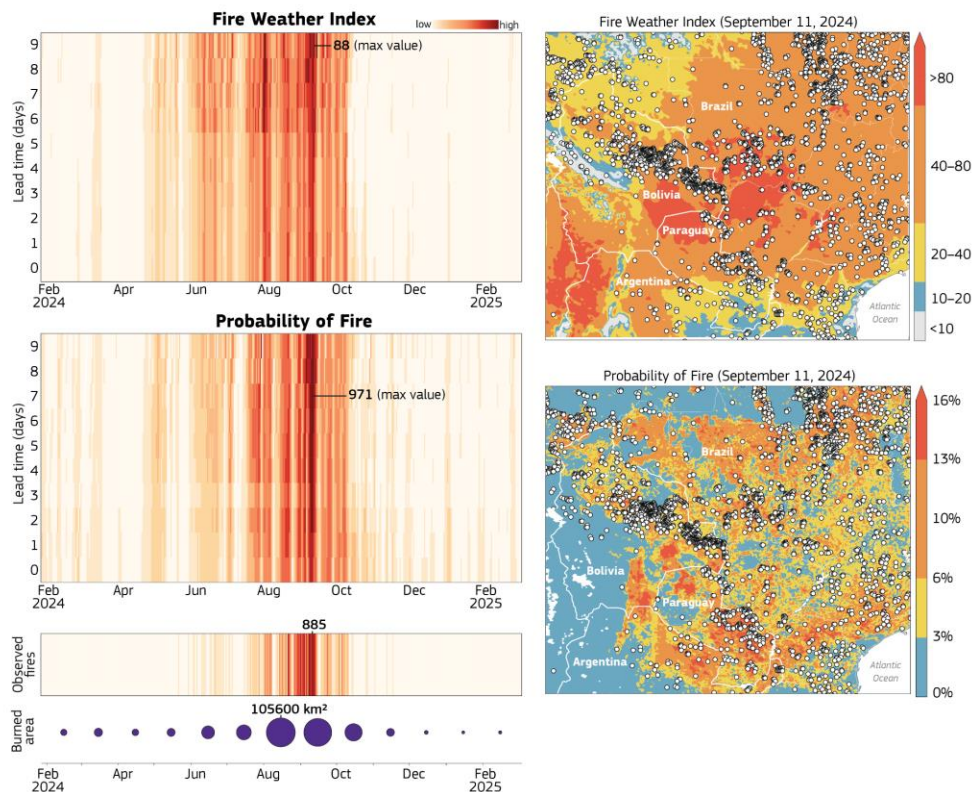
Figure S11: Pantanal and Chiquitano fire forecast (as for **Figure 8 in the main text**). Chicklet plots displaying seamless FWI and POF fire predictions over 10 days forecast. The x-axis corresponds to specific dates throughout the year, while the y-axis denotes either observations or the time leading up to the date when a forecast was generated. The vertical colour coherence allows for quick identification of the time windows of predictability associated to the observed fire activity both provided in terms of number of detected active in a day fires and total BA in a month (circles). The maps represents a snapshot in time at day 0 to allow the comparison of the spatial distribution of the forecasts and the recorded fire activity by MODIS.

469

Figure S12: Southern California fire forecast (as for Figure 8 in the main text). Chicklet plots displaying seamless FWI and POF fire predictions over 10 days forecast. The x-axis corresponds to specific dates throughout the year, while the y-axis denotes either observations or the time leading up to the date when a forecast was generated. The vertical colour coherence allows for quick identification of the time windows of predictability associated to the observed fire activity both provided in terms of number of detected active in a day fires and total BA in a month (circles). The maps represents a snapshot in time at day 0 to allow the comparison of the spatial distribution of the forecasts and the recorded fire activity by MODIS.

478

Figure S13: Congo basin fire forecast (as for **Figure 8 in the main text**). Chicklet plots displaying seamless FWI and POF fire predictions over 10 days forecast. The x-axis corresponds to specific dates throughout the year, while the y-axis denotes either observations or the time leading up to the date when a forecast was generated. The vertical colour coherence allows for quick identification of the time windows of predictability associated to the observed fire activity both provided in terms of number of detected active in a day fires and total BA in a month (circles). The maps represents a snapshot in time at day 0 to allow the comparison of the spatial distribution of the forecasts and the recorded fire activity by MODIS.

487
Figure S14. Forecast and observed burned-area anomalies for four seasons: JFM, MJJ and JJA in 2024, and DJF in 2025. Rows correspond to these seasons and are linked respectively to the case-study regions Amazonia, Congo, Pantanal and Los Angeles (highlighted in green). The columns display (i) the probability of a burned-area anomaly occurring (left), (ii) whether the early-warning system was triggered (centre), and (iii) the anomaly that was actually observed (right). Grey shading marks grid points where the climate-fire model is not statistically significant (p-value ≥ 0.01), while white indicates points where seasonal burned area was zero in less than half of the study period (i.e. BA = 0 in fewer than 11 of the 22 years, 2002–2023; see (i.e. BA = 0 in fewer than 11 of the 22 years, 2002–2023; see Torres-Vázquez et al., 2025).

498
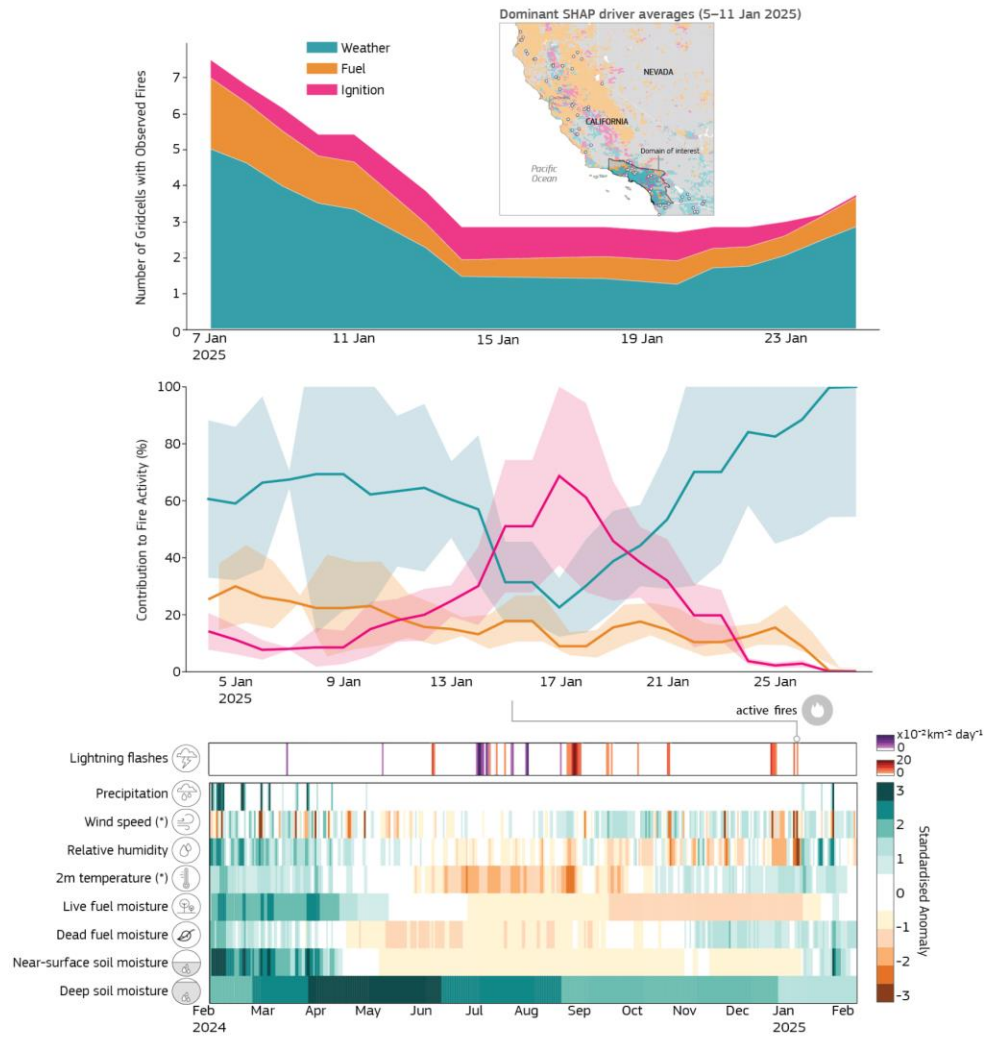
499   **Figure S15:** Drivers explaining fire hotspots in Southern California (as for **Figure 10 in the**
500   **main text**).

501

Congo basin

502

Figure S16: Drivers explaining fire hotspots in the Congo basin (as for **Figure 10 in the main text**).

503
504

505
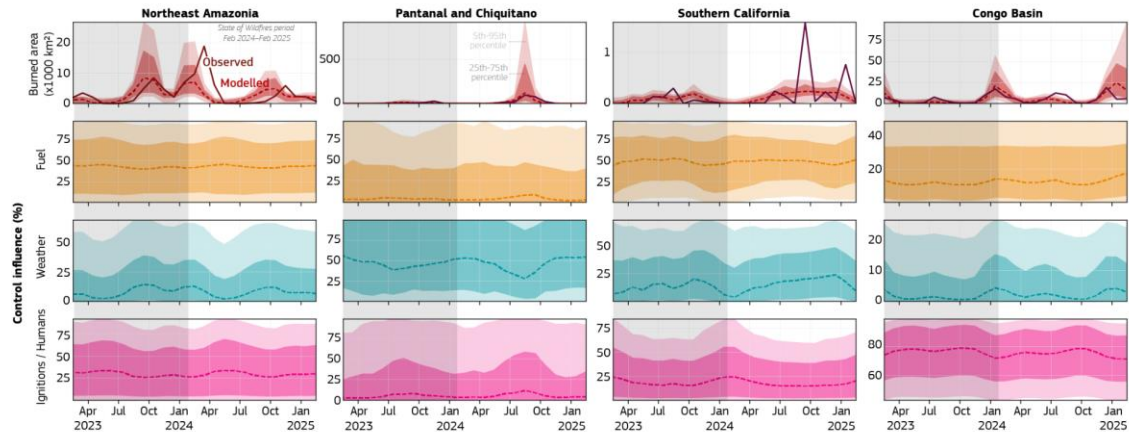
Figure S17. Time series of burned area and key fire drivers for each focus region during 2024. Columns represent different regions; rows show different variables. Top row: Observed burned area (blue) and modelled burned area (red) for each region, with the model median (solid red line), interquartile range (shaded), and 5th–95th percentile range (lighter shading). Second to fourth rows: Modelled contributions from key fire drivers—fuel availability, fire weather, and human/ignition-related factors—with each showing median (solid line), interquartile range (shaded), and 5th–95th percentile range. Together, these panels illustrate the relative influence of climate and human factors on fire activity throughout the year.

514
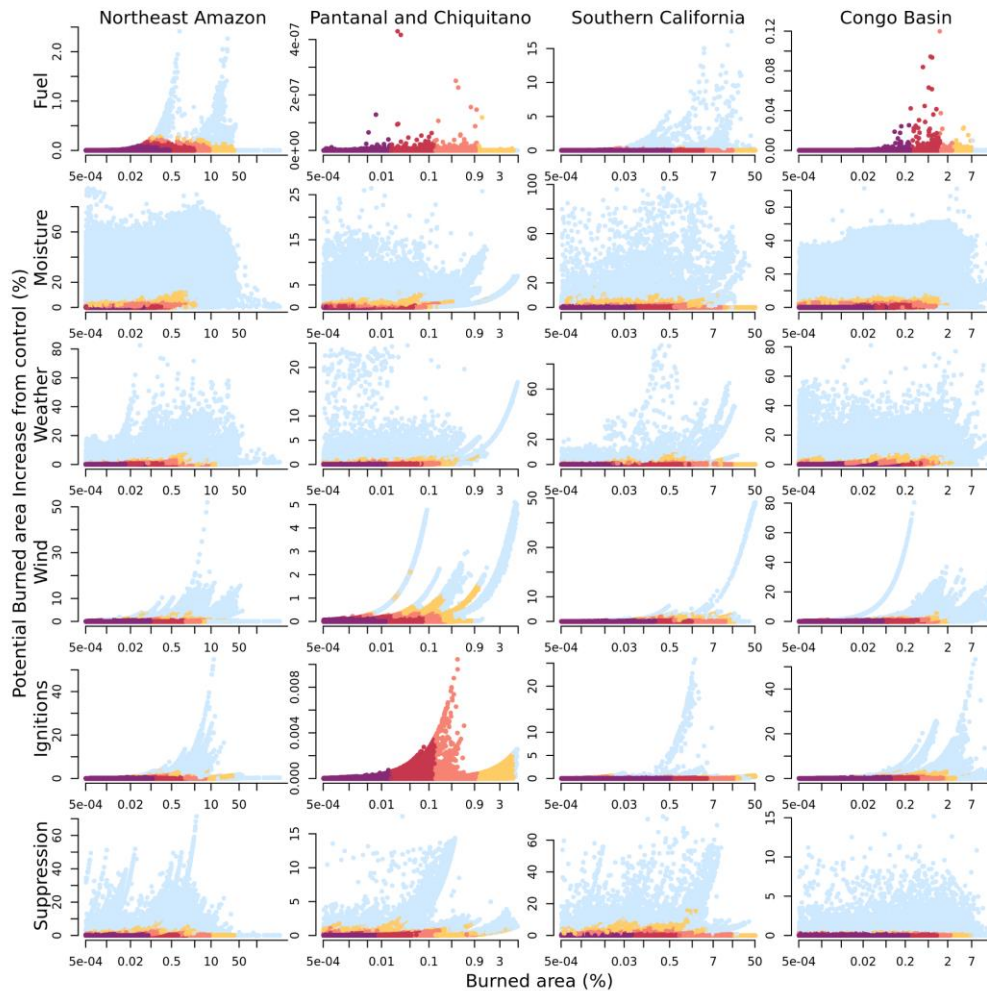
Figure S18. Potential increases in burned area (y-axis) under different fire-controlling factors across varying levels of simulated burned area (x-axis), shown separately by region (columns) and control factor (rows). Results are drawn from the full 5000-member ConFLAME ensemble. Shading indicates the density of grid cells where a given potential increase occurs, with darker areas representing higher density. Each control factor represents a specific constraint on fire activity:

- Fuel: the difference between BA simulated under plentiful fuel loads versus actual fuel loads.
- Moisture: the effect of fuel moisture, comparing perfectly dry to actual moisture conditions.
- Weather: the influence of atmospheric conditions, comparing the most extreme simulated fire weather to observed conditions.
- Wind: the increase in BA expected under maximum wind conditions versus actual winds.
- Ignitions: the difference between saturated ignitions (i.e., unlimited human or natural ignition sources) and observed ignition patterns.
- Suppression: the difference between scenarios with no fire suppression and those reflecting actual suppression efforts.

Together, these estimates illustrate the latent potential for fire spread under different limiting factors, helping to disentangle which constraints most strongly regulate fire activity in each region and at different severity levels.

536
537
538
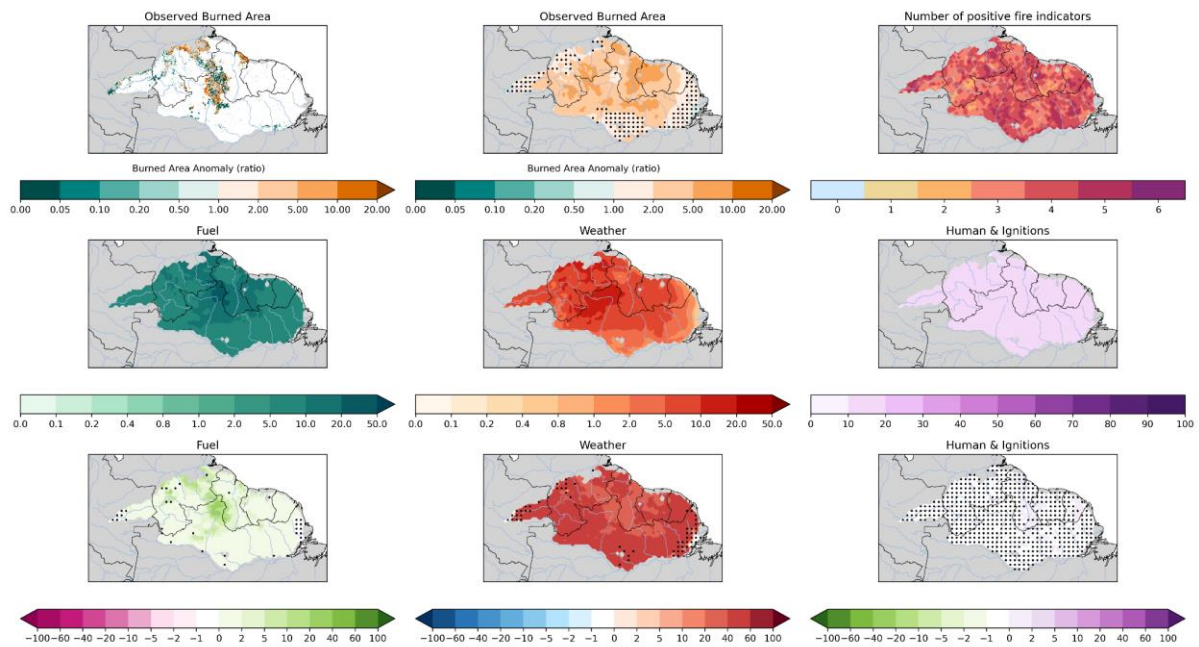
539
540 **Figure S19** Spatial distribution of burned area and fire driver anomalies for January-March
541 2024 in Northeastern Amazonia. Top row: Observed burned area anomalies from MCD64A1
542 (left); ensemble mean burned area anomalies simulated by ConFLAME (middle); and the
543 number of fire-relevant controls (out of seven) showing a positive anomaly during the same
544 period (right). Second row: Mean simulated control strength for each of the three grouped
545 controls, expressed using the "standard limitation" formulation (Kelley et al., 2019), indicating
546 the degree to which each factor constrained or enabled burning. Bottom row: Anomalies in
547 control strength compared to the modelled climatology. Values represent ensemble means
548 across all 4,000 members. Dots on the anomaly maps indicate grid cells with low agreement
549 across ensemble members (<95% agreement in the direction of change), reflecting lower
550 confidence in the sign of the anomaly at those locations.
551
552
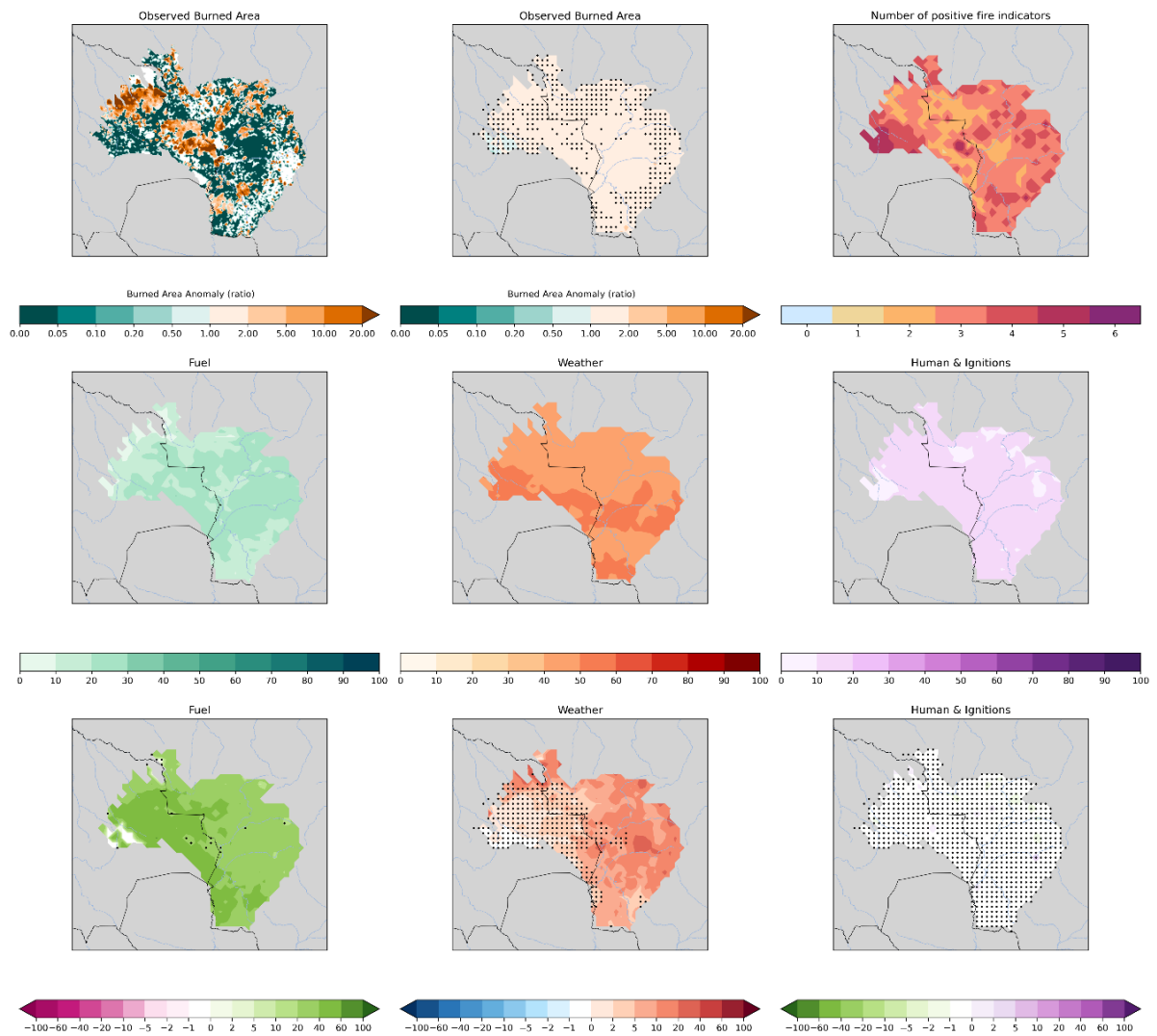
553
Figure S20 As Figure S19 but for Pantanal & Chiquitano, August and September 2024
555
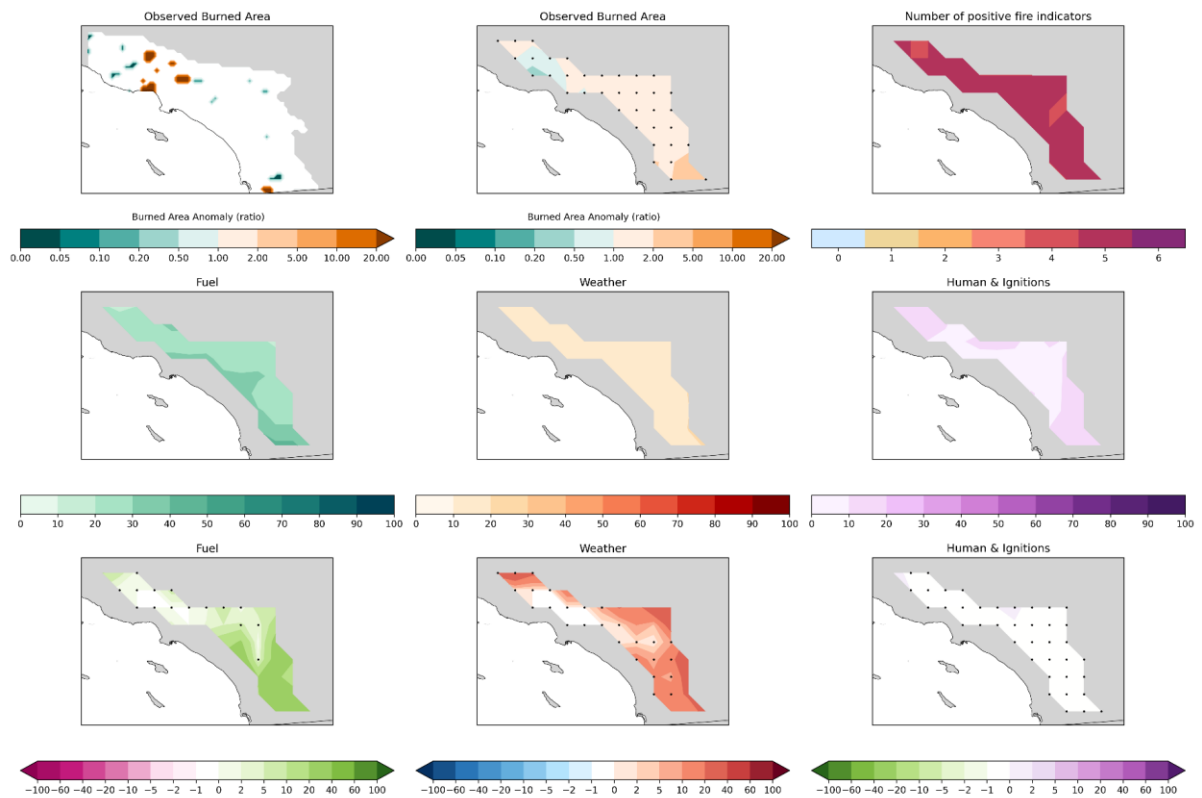
556
557 **Figure S21** As Figure S19 but for Southern California, January 2025.
558
559
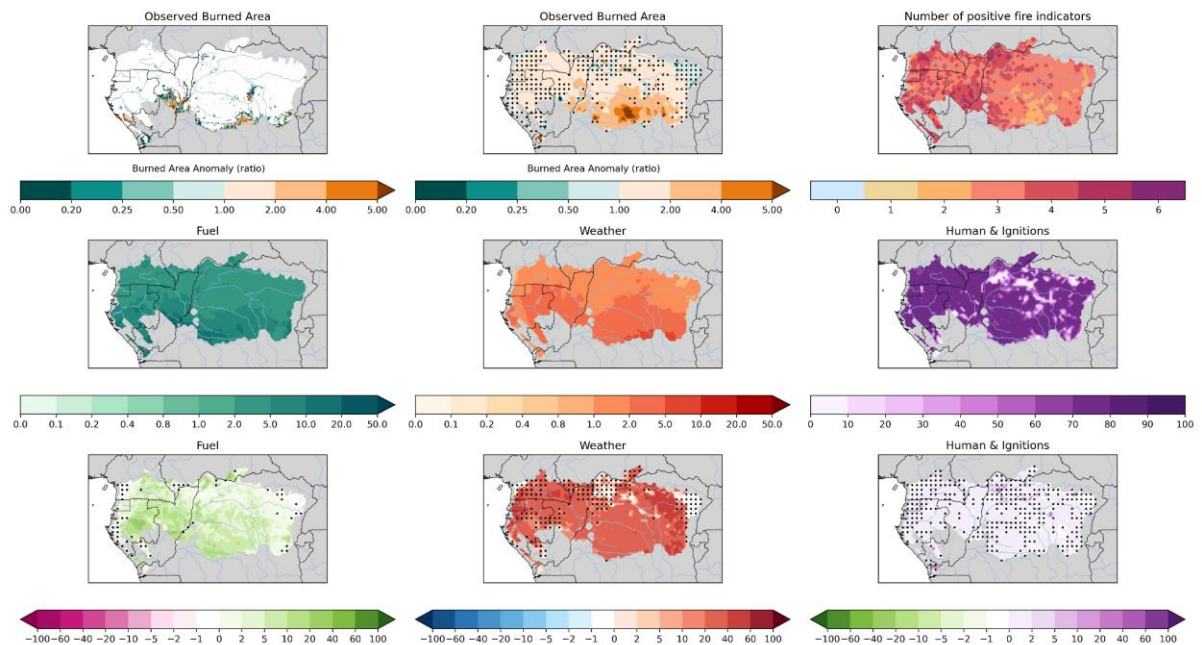
560
561 **Figure S22** As Figure S4.9 but for Congo Basin, July and August 2024

S5 Supplementary Material for Section 5

S5.1 Methods

Table S2: Guide to different attribution comparisons discussed. Coloured boxes indicate what is accounted for in counterfactual comparisons, which variable is targeted or where we look directly as the event or a longer historic record.

Attribution type	Model	**Factual** vs *counterfactual* data sources	Removed in Counterfactual						Target variable			Target period	
			GHG emissions on climate	Aerosols on climate	Land use on climate	Climate & CO2 on fuel	Natural climate trends	Humans on fire	Event FWI	Event BA	Background BA	During the event	Historic
Anthropogenic climate Forcing	Canadian FWI	HaDGEM3-A **All** vs *NAT*	██ (magenta)	██ (pink)	██ (purple)				██ (orange)			██ (dark red)	
	CanESM5 FWI	*CanESM5* **2014-2025** *vs 1850–1859*	██ (magenta)	██ (pink)	██ (purple)	██ (teal)	██ (light blue)		██ (orange)				██ (dark red)
	WWA - sourced from already published material		██ (magenta)	██ (pink)	██ (purple)				██ (orange)			██ (dark red)	
	ConFLAME NRT	**ERA5** vs *merged ERA5/HadGEM3-A*	██ (magenta)	██ (pink)	██ (purple)					██ (orange)		██ (dark red)	
Total climate forcing	ConFLAME ISIMIP	ISIMIP3a GSWP3 **reanalysis** vs *detrended*	██ (magenta)	██ (pink)	██ (purple)	██ (teal)	██ (light blue)			██ (orange)			██ (dark red)
	FireMIP										██ (orange)		██ (dark red)
Socio-economic factors	ConFLAME ISIMIP	ISIMIP3a GSWP3 detrended **2003-2019** vs *1901-1917*						██ (light purple)		██ (orange)			██ (dark red)
	FireMIP							██ (light purple)			██ (orange)		██ (dark red)
All forcings	ConFLAME ISIMIP	ISIMIP3a GSWP3 **reanalysis 2003-2019** vs *detrended 1901-1917*	██ (magenta)	██ (pink)	██ (purple)	██ (teal)	██ (light blue)	██ (light purple)		██ (orange)			██ (dark red)
	FireMIP		██ (magenta)	██ (pink)	██ (purple)	██ (teal)	██ (light blue)	██ (light purple)			██ (orange)		██ (dark red)

566

S5.1.1 Attributing Extremes in Fire Weather during 2024-25 - extended

We applied a bias correction to the 2023 HadGEM3 large ensemble using a linear regression approach, based on comparisons between the model's historical simulations (1960–2013) and the ERA5 reanalysis of fire weather index (FWI). The FWI data were transformed prior to regression to stabilise values at the high end, ensuring extreme fire conditions were accurately captured without distorting the distribution. This correction was anchored to 2023 conditions by extrapolating trends from the historical period to account for recent warming.

Each present-day ensemble member was corrected against all historical ensemble members, producing a large ensemble of bias-adjusted simulations (7875 members in total). This method avoids assumptions about pairwise matching of ensemble members due to the perturbation process used in generating the ensemble.

We then calculated risk ratios (RRs) for extreme fire weather events by comparing the likelihood of exceeding the observed 2023 FWI threshold in the bias-corrected "ALL" (with climate change) and "NAT" (without climate change) simulations. The RR represents how much more likely the event was in today's climate compared to a world without anthropogenic influence. Uncertainty was assessed using bootstrapping.

Full technical details are provided in last years report supplement section S1.2.3 Jones et al. (2024b) and Burton et al. (2025).

S5.1.2 Background changes in fire weather this decade

To complement the HadGEM large-ensemble weather simulations, we also use a fully coupled Earth system model approach to assess the changing probability of extreme fire weather events. This method uses the Canadian Earth System Model version 5 (CanESM5 Swart et al., 2019), developed for the sixth phase of Coupled Model Intercomparison Project (CMIP6; Eyring et al., 2016). CanESM5 provides a 50-member ensemble spanning both the historical period (1850–2014) and high-emission future projections (SSP585, through 2100). By drawing on a physically consistent climate model ensemble, this method offers an independent line of evidence for assessing the role of anthropogenic climate change. Unlike the weather-perturbation ensemble, this method evaluates how often events of similar magnitude to those in 2024/25 would have occurred between 2016-2025.

For each focal region and season, we extract the annual maximum of 7-day average FWI for each ensemble member and apply a statistical model (a time-dependent Generalized Extreme Value distribution), as often used in previous attribution studies (Eden et al., 2016, 2018; Krikken et al., 2021; Liu et al., 2022a, 2023, 2022b; Otto et al., 2018; e.g. Schaller et al., 2014; van der Wiel et al., 2017) to estimate how the probability of extreme fire-conducive conditions has changed over time. In this section, we compare the likelihood of these events under pre-industrial conditions (1850–1859) to their likelihood in the recent past (2016–2025). These comparisons are expressed as a **probability ratio (PR)**. For example, a PR of 10 indicates a tenfold increase in the chance of such an event occurring in the modern climate compared to pre-industrial conditions. In this study, we define 'high fire weather' conditions as the percentile rank of extreme Fire Weather Index (FWI) values during the event period, calculated relative to the full ERA5 historical record. For instance, if the event corresponds to the 95th percentile in the observed record, we assign the 95th percentile value from the model simulations as the representative magnitude of the event within the simulations. Confidence intervals for these PRs are estimated using bootstrapping. This approach, again following a similar approach outlined by (Liu et al., 2022c), allows us to account for uncertainties arising from internal

620 climate variability and limited sample sizes, while leveraging the strength of large ensemble
621 simulations.
622
623 While this approach relies on a more generalised representation of climate and fire-relevant
624 processes — and applies a statistical fit to account for sample size limitations — it adds
625 valuable robustness by providing attribution results from an independent model and that
626 assesses FWI occurrence over a longer period. Together with the HanGEM3-A approach, this
627 approach strengthens confidence in the conclusions drawn by offering a diverse and
628 independent line of evidence for the role of climate change in recent fire weather extremes.

S5.1.2.1 Model and Data

630 We use the Canadian Fire Weather Index (FWI; van Wagner, 1987) calculated from daily
631 ERA5 reanalysis data for 1951–2025, and from the CanESM5 large ensemble simulations for
632 1850–2100 (Swart et al., 2019). The CanESM5 model was selected due to the availability of
633 a 50-member ensemble under the historical (1850–2014) and SSP5-8.5 scenario (2015–
634 2100), providing sufficient sample size for extreme value analysis.

S5.1.2.2 Statistical Framework

636 We follow a time-dependent Generalized Extreme Value (GEV) approach (Eden et al., 2016;
637 Liu et al., 2022a, b; Philip et al., 2020; van der Wiel et al., 2017). For each focal region and
638 fire season, we calculate annual maxima of 7-day average FWI from each ensemble member
639 and fit them to a GEV distribution.

640 The location (μ) and scale (σ) parameters are modelled as linear functions of 4-year smoothed
641 global mean surface temperature (GMST) from the ensemble mean, capturing the externally
642 forced response. The shape parameter (ξ) and the σ/μ ratio are held constant. This yields a
643 time-evolving distribution from which return periods (and hence probabilities) for a fixed event
644 magnitude can be computed across different climate baselines.

S5.1.2.3 Attribution

646 For attribution, we evaluate the return period of a specific observed 2024 event magnitude
647 (e.g., 7-day FWI max) in:

648 ● A pre-industrial baseline: 1850–1859
649
650 ● A recent baseline: 2015–2024

651 We then use the Risk Ratio in **S5.1.1**.

5.1.2.4 Uncertainty

653 We estimate 90% confidence intervals using a non-parametric moving-block bootstrap with
654 1,000 replicates (Efron and Tibshirani, 1998; van der Wiel et al., 2017). This preserves
655 autocorrelation in annual maxima sequences and accounts for interannual variability across
656 the ensemble.

5.1.3 Attributing Region-wide Extreme BA during 2024-25 - extended

658
659 The near real-time configurations test and training follows the same setup as described in
660 **Section 4**, but excludes the fuel moisture variables, as we do not have counterfactuals
661 available for these variables. We use the same training protocol as outlined in **Section 4.2**.
662 The factual climate is based on ERA5 reanalysis, providing physically consistent and

observation-constrained meteorological conditions for the fire event. The counterfactual climate represents a world without human influence on the climate system. It is created by adjusting ERA5 temperature, maximum temperature, precipitation, dry days, consecutive dry days, humidity, and minimum humidity variables using variable-specific adjustment functions ("deltas"). These deltas are derived from differences between the HadGEM3-A ALL-forcings and natural-forcings simulations described in **Section 5.1.2**, with:

$$\omega(CF) = \omega(ERA5) + \omega(NAT) - \omega(ALL)$$

Where CF is the counterfactual climate, ω is the transformation required to remove data bounds of the specific variable, and φ is the inverse of ω. The following transformations are applied to create counterfactual values for each climate variable:

- Temperature (Mean and Max): $\omega(x) = x$
- Precipitation: $\omega(x) = \log(e^x - 1)$
- Windspeed, soil moisture: $\omega(x) = \log(x)$
- Relative Humidity: $\omega(x) = \log(x/(1-x))$

Since relative humidity (RH) is not available directly from ERA5, we will therefore calculate it from 2m temperature (T_s) and 2m dew point temperature (T_d):

$$RH = 100 \times e_d/e_s$$

where e_d is the actual vapour pressure (calculated from the dewpoint temperature) and e_s is the saturation vapour pressure (calculated from the air temperature):

$$e_i = 6.112 \times exp\left(\frac{17.625 \times T_i}{T + 243.04}\right)$$

We perform two types of counterfactual simulations to understand the influence of human-caused climate change: one using all individual members of the HadGEM3-A ensemble, and one using the ensemble mean. The full ensemble captures a wide range of possible weather outcomes and includes natural year-to-year variability, making it a more cautious or conservative estimate of the effect of climate change. The ensemble mean, by contrast, smooths out this variability to isolate the long-term influence of climate forcing, providing a cleaner signal. Since our analysis targets a specific year, the actual role of weather variability should, in theory, matter less. However climate change can interact with this variability in complex, sometimes non-linear ways, thereby making certain extremes more or less likely depending on the background conditions, we don't know exactly where within that range the real-world outcome lies. As a result, the true effect of climate change likely falls somewhere between these two estimates. We therefore report the full ensemble results as our main findings and refer to the ensemble mean where it offers useful additional context or diverges substantially.

We also use an **ISIMIP configuration** of ConFLAME, as used in last year's report. The available data differs from our near real-time setup, so for this configuration we group controls into four categories (**Table S3**):

1. **Fuel load**, represented by total vegetation cover and tree cover.
2. **Fuel moisture**, represented by mean consecutive dry days within each month, the fraction of dry days within the month, daily mean precipitation, mean and maximum monthly temperature, and mean and maximum vapour pressure deficit (VPD).
3. **Ignitions**, represented by climatological lightning, pasture, crop, and population density.
4. **Suppression**, represented by pasture, crop, and population density.
5. **Land use change**, represented by 12 month running mean change in tree, crop, and pasture.

We trained the ConFLAME ISIMIP configuration on observed monthly BA from the MODIS BA product (MCD64A1) during 2003-2019 at 0.5° resolution across the entire region. For model

713 training and for factual, we used Global Soil Wetness Project Phase 3 (GSWP3-W5E5)
714 meteorological forcings, as provided at 0.5° spatial resolution by ISIMIP3a (see Table 5). Land
715 surface information (tree cover and non-tree vegetated cover) was derived from dias corrected
716 JULES-ES-ISIMIP model output (Mathison et al., 2023), which was also driven by GSWP3-
717 W5E5. This model includes dynamic vegetation, accounting for changing vegetation cover in
718 response to climate, growth, competition, and mortality. To avoid double-counting the impact
719 of fire, we disabled the model's interactive vegetation-fire module. The bias in this land surface
720 information is adjusted to the MODIS Vegetation Continuous Fields collection 6.1 remote
721 sensed data (Dimiceli et al., 2015), using a linear scaling approach. This preserves trends
722 between historical and future periods and ensures accurate means and distribution. See
723 **Supplementary Text S2** for details.

724 *S5.1.3.1 Deriving ConFLAME vegetation fraction driving data*
725

726 In **Sections 5.3.1**, and **6.1.2.2,** we drive ConFLAME with tree and non-tree vegetated cover
727 from the Joint UK Land Environment Simulator Earth System impacts model (JULES-ES) at
728 version 5.5 (Clark et al., 2011; Mathison et al., 2023) driven with GSWP3-W5E5 forcings
729 provided at a 0.5° spatial resolution by ISIMIP3a. These runs are freely available at
730 https://www.isimip.org/impactmodels/details/292/. JULES-ES dynamically models vegetation
731 cover in response to meteorology, hydrology, nitrogen availability, and land use change.
732 JULES-ES has been extensively evaluated against snapshots and site-based measurements
733 of vegetation cover and carbon (Burton et al., 2019, 2022; Clark et al., 2011; Mathison et al.,
734 2023; Sellar et al., 2020). JULES-ES-ISIMIP has previously been used as driving data for
735 ConFLAME to perform future projections (UNEP et al., 2022), though using a previous round
736 of ISIMIP climate forcing (ISIMIP2b). As per (UNEP et al., 2022), vegetation responses to
737 JULES-ES's internal fire model were turned off so as not to double-count the effects of burning.
738
739 However, in (UNEP et al., 2022), residual JULES-ES simulated biases in vegetation cover
740 were allowed to persist, increasing the uncertainty range of local vegetation cover and
741 resultant burned area responses. We therefore correct the bias in JULES-ES's vegetation
742 cover using a linear scaling bias adjustment method, implemented using the ibicus software
743 package (Spuler et al., 2024, ibicus).
744
745 The method corrects the bias induced by the JULES-ES model rather than the bias of the
746 climate model, assuming that this has been removed by the ISIMIP3BASD method(Lange,
747 2019). For each surface cover type at each grid cell, the bias adjustment method identifies
748 biases in the mean and variance of the JULES-ES model output relative to MODIS VCF
749 collection 6.0 remotely sensed data (Dimiceli et al., 2015) at this grid cell. These biases in
750 mean and variance are then removed from the surface information output from JULES-ES
751 driven by climate models over the historical (1994-2014) and future (2015-2099) period,
752 ensuring that the resulting model output is still bounded by [0, 1]. This bias adjustment method
753 preserves the trend in mean and variance. While a trend-preserving empirical quantile
754 mapping was used in the State of Wildfires 2023/24 publication, further analysis showed that,
755 given the limited amount of observational data, this simpler method performs equally well while
756 requiring fewer assumptions and parameters to fit, leading to an overall more robust bias
757 adjustment.
758
759 The results were evaluated in terms of the ability of the bias correction method to reduce the
760 model bias over the historical period, as well as preserve the trend between the future and
761 historical periods. It was found that the method corrects the bias well over the historical period
762 for most regions, variables and grid cells in both the mean and 80th percentile at each grid
763 cell. The mean trend between the future and historical period is preserved by definition, but
764 also quantile trends in most regions and grid cells are well preserved.

765 To demonstrate the evaluation conducted, **Figure S27** shows the results for tree cover over
766 the Amazon region. The plots for the remaining regions, including tree and no-tree cover, can
767 be found in a notebook https://github.com/jakobwes/State-of-Wildfires---Bias-Adjustment.
768 Investigating the time series of average tree cover over the region, we find that the correction
769 method reduces the bias over the historical period and matches the future period to the
770 historical period (**Figure S27a**). The cumulative distribution functions of average tree cover
771 merged over all spatial locations in observations and the model matches better after bias
772 adjustment (**Figure S27b**). They do not match perfectly, and we note that this is a non-
773 calibrated aspect that we do not expect to have zero bias, but that is important to evaluate.
774 Furthermore, we find that the improvement in both mean and 80th percentile holds across the
775 region (**Figure S27c**). The trend between future and historical periods is preserved for the
776 majority of grid-cells, with the absolute change in trend being close to zero for most grid-cells.

777

S5.1.4 FireMIP

779
780 For the multi-model ensemble we use simulations from the ISIMIP3a fire sector, as published
781 in (Burton & Lampe et al. 2024). The 7 models reporting BA for ISIMIP3a are shown in **Table
782 S3**. The methodology follows the ISIMIP3a Impacts Attribution protocol, as outlined in (Mengel
783 et al., 2021), where the factual historical simulations are driven with GSWP3-W5E5 reanalysis
784 data, and the counterfactual simulations are the same historical data which has been
785 detrended via quantile mapping (Mengel et al., 2021).

786
787 As outlined in (Hantson et al., 2016), the spread in the absolute BA is large amongst the
788 observations, models and regions and therefore a normalised relative anomaly (RA) rather
789 than absolute BA is used for the analysis. To calculate the RA in present day BA, we subtract
790 the counterfactual mean, and divide by the counterfactual mean. By comparing both factual
791 and counterfactual experiments to the counterfactual mean, we are looking at the fractional
792 increase in BA driven by climate change compared to a baseline without climate change.
793 Based on model performance by AR6 region, a region-specific weighting is also applied
794 following (Knutti et al., 2017). The weighting is based on the model's distance to the observed
795 BA temporal RA using both FireCCI5.1 and GFED5, measured using NME as per Kelley et al.
796 (2013). To measure the uncertainty, random noise is generated and scaled by the
797 climatological RMSE of each model. This noise is then added to the modelled relative
798 anomaly, this process is repeated 1000 times. Then, bootstrapping is applied to the monthly
799 regional BA RA (now with noise added in) according to the weight for each model. Uncertainty
800 is calculated by taking the 2.5-97.5th percentile of the resultant histogram. All results are
801 reported as P50 [P2.5, P97.5]. The methods are explained in full in (Burton & Lampe et al.
802 2024).

803 **Table S3:** FireMIP Models used for attributing median burned area. Table reproduced from (Burton & Lampe et al. 2024)

Model		CLASSIC	INFERNO	LPJ-GUESS-SIMFIRE-BLAZE	LPJ-GUESS-SPITFIRE	ORCHIDEE-MICT-SPITFIRE	SSiB4/TRIFFID	VISIT
Fire Model		CLASSIC	INFERNO	SIMFIRE	SPITFIRE	SPITFIRE	Li	After (Thonicke et al., 2008))
Land / Vegetation		CLASSIC	JULES	LPJ-GUESS	LPJ-GUESS	ORCHIDEE	SSiB	VISIT
Dynamic Veg	Physiology	Yes	Yes, via TRIFFID	Yes	Yes	Yes	Yes, via TRIFFID	Yes
	LAI	Yes	Yes, via TRIFFID	Yes	Yes	Yes	Yes	Yes
	Bio-geography	No	Yes, via TRIFFID	Yes	Yes	Yes	Yes	No
Nitrogen Cycle		Yes	Yes	Yes	Yes	No	Yes	Yes, but C-N coupling is limited
No. PFTs		9	13	17	17	19	7	33 (biome types)
No. Soil Layers		20	4	2	2	11	3	2
Fuel		Vegetation and litter	Vegetation & top soil layer as proxy for litter	Vegetation, litter	Litter	Vegetation and litter	Vegetation and litter	Litter
Ignitions	Natural	Prescribed lightning	Prescribed lightning	SIMFIRE describes annual BA + fire-climatology -> daily BA used as Fire-Probability	Prescribed lightning	Prescribed lightning	Prescribed lightning	Probabilistic based on fuel wetness
	Anthropogenic	Prescribed population density	Prescribed Population density	SIMFIRE includes suppression by humans	Prescribed population density	Prescribed population density	Prescribed population density	No

Suppression	Prescribed population density	Crops, population density	Crops (100%), prescribed population density (Hyde3.1)	Crops, population density	Prescribed population density, crops	Prescribed population density and GDP	Low fuel load
Spread	Wind speed and soil moisture	None	Daily BA (no explicit spread)	Rothermel equations including wind speed, tree fraction, grass fraction, fuel moisture, fuel load and characteristics	wind speed, tree fraction, grass fraction, fuel moisture, fuel load	Wind speed and soil moisture	None
Model inputs	SW & LW radiation, precipitation, air temperature, specific humidity, wind speed, atmospheric pressure, population density, lightning	SW & LW radiation, precipitation, air temperature, specific humidity, wind speed, population density, lightning	SW radiation, precipitation, air temperature (mean, min, max), relative humidity, wind speed	SW radiation, precipitation, air temperature, specific humidity, wind speed, atmospheric pressure, population density, lightning	SW & LW radiation, precipitation, air temperature, specific humidity, wind speed, atmospheric pressure, PFT map, population density	SW & LW radiation, precipitation, air temperature, specific humidity, wind speed, atmospheric pressure, population density, and GDP, peat map, land cover change	Air temperature, precipitation, air vapor pressure, cloudiness, wind
Resolution	1 deg	0.5 deg	0.5 deg	0.5 deg	0.5 deg	0.5 deg	0.5 deg
References	(Melton et al., 2019)	(Burton et al., 2019, 2020; Mangeon et al., 2016)	(Knorr et al., 2014; Rabin et al., 2017; Smith et al., 2014)	(Lehsten et al., 2009; Rabin et al., 2017; Smith et al., 2014; Thonicke et al., 2010)	(Yue et al., 2014, 2015)	(Huang et al., 2020, 2021; Hugelius et al., 2013; Li et al., 2012, 2013)	(Ito, 2019)

804

S5.2 Results

S5.2.1 Background changes in fire weather this decade

S5.2.1.1 Northeast Amazonia

Area/Time: *All region/Jan–Mar 2024*
Variable: *Fire Weather Index*
Attribution Type: *Anthropogenic climate forcing*
Includes: *Changes in climate since Pre-Industrial*

To understand longer-term trends, we estimate how global warming has changed the average likelihood of extreme fire weather over the past decade. Using a statistical fit to the CanESM5 model ensemble, we find that fire weather conditions like those seen in 2024 have become 1.9 times more likely on average since pre-industrial times, with a 95% confidence range of [1.5, 53.3].

While this method gives less event-specific resolution, it supports the conclusion that climate change has increased the background risk of extreme fire weather in the region over the last 10 years reinforcing the HadGEM-based result.

S5.2.1.4 Congo Basin

Area/Time: *All region/Jun-Aug 2014-2025*
Variable: *Fire Weather Index*
Attribution Type: *Anthropogenic climate forcing*
Includes: *Changes in climate since Pre-Industrial*

Using the CanESM5 ensemble, we find that fire weather conditions similar to those observed in July–August 2024 were 1.3 times more likely due to climate change ([0.7, 1.8], 95% CI) over the last decade. While more uncertain than the HadGEM3-A analysis, the findings are not inconsistent: both show a positive central estimate. The difference likely reflects the broader decadable sampling of the CanESM5 method or as well as differences in the underlying model systems. However, both methods suggest that climate change has increased the likelihood of fire-conducive weather in the Congo Basin.

S5.2.2 Region-wide extreme BA during 2024-25.

S5.2.2.1 Northeast Amazonia
Time: *Jan-Mar 2003-2019*
Variable: *Burned Area*
Attribution Type: *Total climate change*
Includes: *All anthropogenic and natural trends in climate*

We also assessed the influence of total climate forcing on the frequency of fire activity in the Northeast Amazonia for all January-March during 2002-2019. The likelihood of a climate-driven increase in regional burned area (BA) during these ~2 decades was just 56% (**Figure 14**), indicating that any long-term trend remains highly uncertain. The central amplification factor was 1.17, with a 90% confidence range of 0.88 to 1.15 (**Table 6**), encompassing the possibility of no change. In contrast to the direct attribution of the 2024 fire season, this analysis shows no clear signal that total climate forcing increased overall BA during this earlier

857 period. A similar picture emerges for sub-regional extremes, with a likelihood of an increase
858 due to climate forcing was 70%, just meeting the IPCC threshold for being considered likely.
859 The amplification factor was modest-1.02, with a 90% range of 0.94 to 1.13-indicating that
860 while climate may have played a role in enhancing the most intense burning, its influence was
861 relatively small and uncertain during this timeframe.
862
863 Together, these results suggest that while anthropogenic climate change had a strong and
864 detectable impact on the 2024 fire season, similar effects were not consistently evident in the
865 decades prior. The relatively low upper bounds on amplification, particularly for sub-regional
866 extremes, imply that large increases in anomalous fire activity were not widespread prior to
867 2020. This interpretation aligns with earlier research (Kelley et al., 2019) showing only a weak
868 meteorological contribution to elevated burning in the southern parts of the region during the
869 large fire anomalies in 2019.
870
871 However, it is important to note that the analysis ends in 2019, excluding a series of major
872 droughts and fire anomalies since 2020. These recent years have shown increasingly frequent
873 and widespread extremes, suggesting that the climate signal may now be strengthening. This
874 is consistent with last year's report, which analysed a Western Amazonia region just southwest
875 of this one. There, long-term trends similarly suggested only marginal increases in sub-
876 regional extremes from 2002–2019, while the risk ratios for specific fire weather events were
877 extremely high. A longer observational window that includes the last five years would help
878 better evaluate whether a persistent shift is emerging.
879
880 **Time:** *Jan-Mar 2003-2019*
881 **Variable:** *Burned Area*
882 **Attribution Type:** *Socioeconomic forcing*
883 **Includes:** *Population density, land use and land cover change*
884
885 For sub-regional extremes, the likelihood that socioeconomic factors increased BA was only
886 slightly higher at 62%. The central Amplification Factor was 1.01, with a narrow range of 0.96
887 to 1.10, indicating only minimal influence. This suggests that in the most fire-affected locations,
888 socioeconomic drivers alone did not strongly amplify the extent of burning during this
889 timeframe. Together, these findings point to a limited or unclear role of socioeconomic change
890 in driving extreme fire activity across the Northeast Amazonia between 2002 and 2019.
891
892 **Time:** *Jan-Mar 2003-2019*
893 **Variable:** *Burned Area*
894 **Attribution Type:** *All forcing*
895 **Includes:** *All anthropogenic and natural trends in climate, population density, land use and*
896 *land cover change*
897
898 We also assessed the combined effect of total forcing, which includes all long-term changes
899 in climate (anthropogenic and natural), land use, land cover, and population density,on burned
900 area (BA). For regional totals, the likelihood that total forcing increased BA was just 47%
901 (**Figure 14**), with a median amplification factor of 0.99 and a 90% confidence interval of 0.81
902 to 1.47 (**Table 6**). This result indicates no clear signal that the combined effects of climate and
903 socioeconomic change had a net impact on fire activity across the region during this two-
904 decade period. For sub-regional extremes,the grid cells with the highest BA in each season,
905 the likelihood of an increase was slightly higher at 62% (**Figure 14**), with a central amplification
906 of 1.01 and a wider confidence interval of 0.96 to 5.1 (**Table 6**). While this suggests that some
907 influence of combined human and climatic drivers on extreme BA cannot be ruled out, the
908 signal remains modest and uncertain overall.
909
910 Together, these findings imply that, even when considering all major sources of long-term
911 change in climate and land use together, there is insufficient evidence to attribute a consistent

912 trend in BA or its extremes across the region for 2002–2019. The relatively wide range for the
913 sub-regional extremes, compared to regional totals, highlights a possibility that landscape
914 modification or localised climate feedbacks could have amplified fire activity in specific
915 hotspots, but the model does not provide enough resolution to identify or confirm such
916 patterns.
917
918 ### S5.2.2.2 Pantanal and Chiquitano
919
920 **Time:** *Aug-Sep 2003-2019*
921 **Variable:** *Burned Area*
922 **Attribution Type:** *Total climate change*
923 **Includes:** *All anthropogenic and natural trends in climate*
924
925 Over the longer-term 2003–2019 period, our analysis suggests that it was virtually certain that
926 total (99%; **Figure 14**) that climate change very likely increased the likelihood of fire events
927 with comparable burned area to August–September 2024 in the Pantanal & Chiquitano region.
928 The median likely amplification factor greater than 100 [90% confidence range of 4.92 >100]
929 (**Table 6**). This suggests that a substantial portion - and possibly the vast majority, of the
930 burned area associated with 2024-like events is attributable to long-term anthropogenic
931 changes in the climate system. The sub-regional attribution signal is consistent with the
932 regional-scale result, which also shows >99% likelihood of an increase (**Figure 14**), with an
933 amplification factor >100 [2.72 to >100] (**Table 6**). While both estimates exhibit wide
934 uncertainty ranges, their overlapping confidence intervals point to a consistent climate signal
935 rather than a statistically clear difference in impact strength between regional and sub-regional
936 scales.
937
938 This analysis provides additional confidence in the role of anthropogenic climate change by
939 situating the 2024-type fire conditions within the broader distribution of fire-weather years over
940 the past two decades. By extending the analysis beyond the specific year of 2024, it helps to
941 identify a persistent fingerprint of climate forcing in driving elevated fire risk.
942
943 By drawing on multiple years of climate and fire conditions, this longer-term approach
944 increases the sample size available for evaluating the likelihood of 2024-like fire events. This
945 may help separate the structural influence of climate forcing more clearly than near-real-time
946 (NRT) event-based attribution. Further analyses comparing NRT and multi-year setups could
947 help explore whether recent variability has masked or amplified long-term trends in fire
948 likelihood.
949
950 **Time:** *Aug-Sep 2002-2019*
951 **Variable:** *Burned Area*
952 **Attribution Type:** *All forcing*
953 **Includes:** *All anthropogenic and natural trends in climate, population density, land use and*
954 *land cover change*
955
956 When assessing the combined influence of all anthropogenic and natural forcings, we find
957 limited attribution power for 2024-like events in the Pantanal and Chiquitano region. At the
958 regional scale, the likelihood that all forcings increased burned area is 61%, with an
959 amplification factor (AF) of 1.05 [0.26–64.3]. This wide uncertainty range suggests that internal
960 variability and counteracting drivers may obscure the net effect of all forcings. For sub-regional
961 extremes, confidence is slightly higher: 84% likelihood, with an AF of 1.00 [0.68–12.16]. This
962 points to a potential increase in burned area, though again with considerable uncertainty.
963
964 While these results do not offer conclusive evidence of a net anthropogenic effect, they
965 underscore the complexity of attributing fire outcomes to the combined influence of climate

and human activity. The limited confidence in these findings highlights the need to improve methodologies capable of capturing interactions and feedbacks between land use, climate, and fire, particularly in regions such as Pantanal and Chiquitano, where these relationships are highly complex. Future reports should move beyond treating climate and socioeconomic drivers in isolation. As interactive and compounding effects become more likely, attribution frameworks that separate human and climate influences risk overlooking critical synergies that are most relevant for effective policy and risk management.

S5.2.2.3 Southern California

Time: *Jan 2003-2019*
Variable: *Burned Area*
Attribution Type: *Total climate change*
Includes: *All anthropogenic and natural trends in climate*

There is limited evidence from this framework that total climate change increased the likelihood of January 2025-like regional burned area in Southern California during the 2003–2019 period. The likelihood of an increase is estimated at 63% (**Figure 14**) with an amplification factor (AF) of 1.07 [0.68–2.83] (**Table 6**), suggesting that total climate change could have played a role, but the model does not provide a confident answer either way. This large range of uncertainty partially stems from the small geographic size of the region, which limits signal-to-noise ratios in long-term attribution frameworks. A similar issue was observed for Greece in last year's report (Jones et al., 2024b), where a confident climate signal was also absent in long-term regional attribution, despite strong evidence emerging from event-specific analysis. Interestingly, while the long-term climate signal here is weak, the near-real-time (NRT) attribution for the 2025 event itself shows a much stronger likelihood of anthropogenic influence, suggesting that climate signals may emerge more clearly during specific extremes than across broader multi-year variability.

As the amount of burned area in January in Southern California is historically nominal given that this is the traditional wet season when flammability is low, some of the elevated uncertainty may stem from local calibration. Likewise, these were principally wind-driven fires due to synoptic-mesoscale features with Santa Ana downslope winds whose features are poorly resolved in the coarse reanalysis data used here. Climate projections show a weak attenuation of the frequency of Santa Ana winds with anthropogenic climate change (Guzman-Morales and Gershunov, 2019; Hawkins et al., 2022), but also an extension of critically dry fuels into winter due to delayed onset of winter precipitation (Goss et al., 2020). The degree to which these two factors alongside the direct thermal influence of climate change on fuel desiccation altered the odds of such extremes requires additional analysis and may not be realized through the approaches used here.

Time: *Jan 2002-2019*
Variable: *Burned Area*
Attribution Type: *All forcing*
Includes: *All anthropogenic and natural trends in climate, population density, land use and land cover change*

There is no clear signal for the impact of all forcing for January 2025-like burned area in Southern California during 2002–2019. The likelihood of an increase is estimated at 55%, with an amplification factor of 1.05 [0.26–64.26], nearly identical to the socioeconomic-only result. This further highlights the challenge of drawing confident conclusions in small regions with limited signal.

S2.2.2.4 Congo Basin

Time: *Jun-Aug 2024*
Variable: *Burned Area*
Attribution Type: *Total climate change*
Includes: *All anthropogenic and natural trends in climate*

Total climate change likely increased the amount of burned area in areas with the height levels of burning, though with limited confidence in the size of this effect. The likelihood of an increase was estimated at 75%, with an amplification factor (AF) of 1.29 [0.96–3.32]. This implies that while a contribution from climate change is more likely than not, the possibility of little to no effect cannot be ruled out. The risk ratio was 1.8, suggesting that events of this severity were nearly twice as likely under current climate conditions than they would have been in a pre-industrial climate.

Time: *Jun-Aug 2024*
Variable: *Burned Area*
Attribution Type: *All forcing*
Includes: *All anthropogenic and natural trends in climate, population density, land use and land cover change*

For the region as a whole, the likelihood of all human and climate forcing increased burning was 55%, with an amplification factor (AF) of 1.01 [0.86–1.42], indicating no clear signal. In the areas most severely affected by fire, the likelihood rose slightly to 63%, with an AF of 1.06 [0.73–4.44]. While this suggests that the combined effect of all forcings could have contributed to the sub-regional extremes, the wide range and low confidence highlight the challenge of attributing fire outcomes in regions where both data and model constraints remain significant.

S5.2.3 Sub-regional extreme burned area during 2024-25

S5.2.3.1 Northeast Amazonia

Area/Time: *Sub-regional extremes/Jan-Mar 2024*
Variable: *Burned Area*
Attribution Type: *Anthropogenic climate forcing*
Includes: *Greenhouse gases, aerosols, and land-use change effects on climate*

Anthropogenic climate forcing also very likely caused increased burned area (BA) in the sub-regional extremes with a likelihood of 96% (**Figure 14; Table 6**). The amplification factor in these areas was smaller than for the region as a whole: fires in these high-BA zones were on average 1.17 times larger, with a 90% confidence range of 1.01 to 5.13. This means that anthropogenic climate forcing likely contributed to increased burning in these areas, though the amplification was more modest than across the broader region. The risk ratio was 2.2, indicating that fire seasons with this spatial pattern of extreme burning are now more than twice as likely due to climate change.

This difference between regional and sub-regional extremes is consistent with earlier findings in **Section 4**, which showed that climate-driven weather anomalies - more directly linked to the influences considered in our attribution, increased the potential for burning across much of the region, while fuel conditions (fuel load and moisture) shaped the location and timing of the most severe burning. The moderate amplification factor in the highest-BA grid cells likely reflects the local interplay between fire weather and fuel constraints, where factors such as fuel limitations or ignition variability may have restricted how much additional burning occurred, even under climate driven more fire conducive weather conditions.

1074
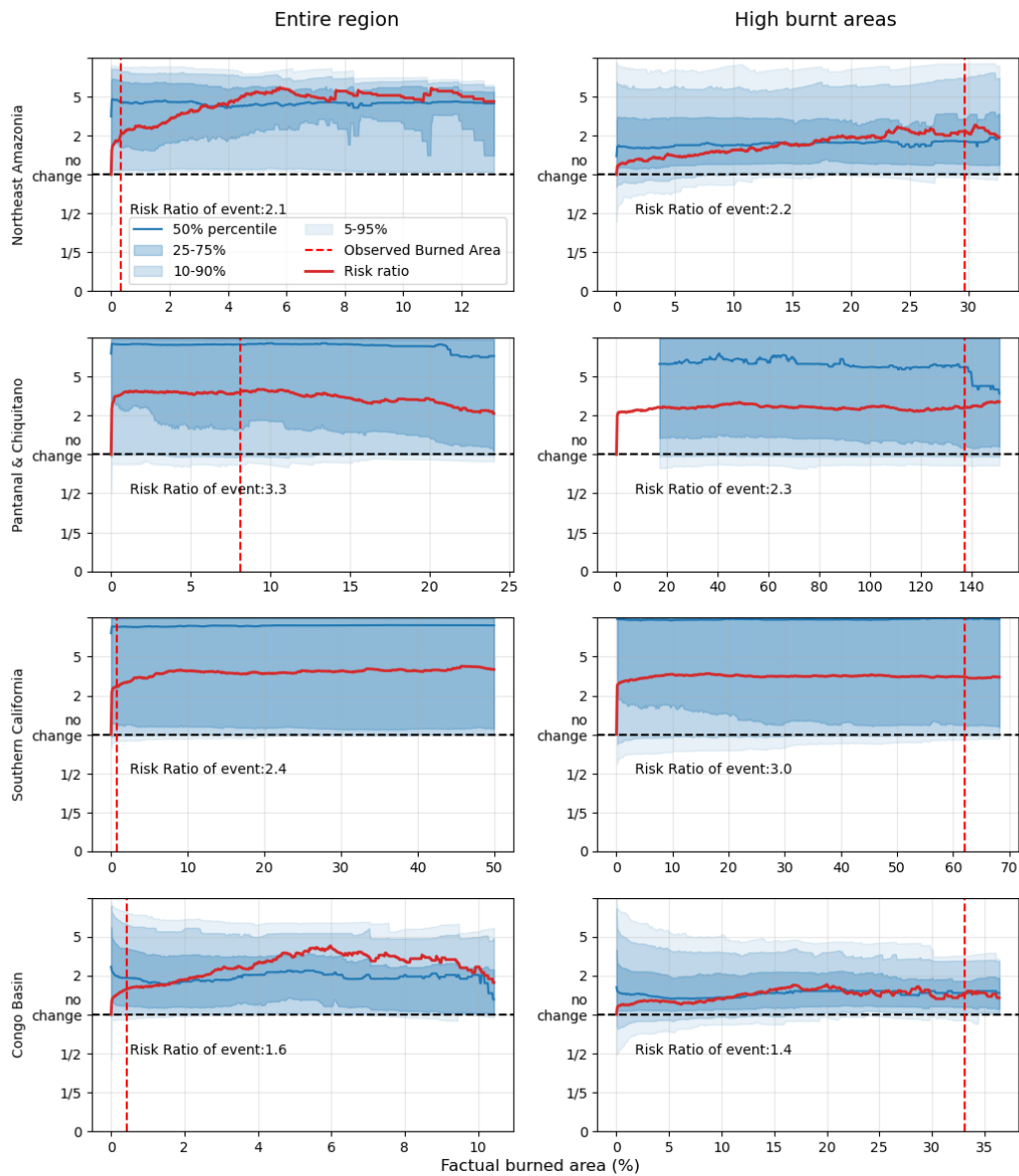
1075
1076 **Figure S23** Risk ratio and amplification factor for different levels of total (left) and sub-regional
1077 extreme (right) burned area, simulated using ConFLAME-NRT for each region (rows).
1078 Percentile ranges for the amplification factor are taken across ensemble members. The red
1079 dashed vertical line indicates observed levels of burned area, for which the corresponding risk
1080 ratio is reported in each panel.

1081

1082

1083 **S5.2.3.2 Pantanal and Chiquitano**

1084

1085 **Area/Time:** *Sub-regional extremes/Aug-Sep 2024*
1086 **Variable:** *Burned Area*
1087 **Attribution Type:** *Anthropogenic climate forcing*
1088 **Includes:** *Greenhouse gases, aerosols, and land-use change effects on climate*
1089

1090 Anthropogenic climate forcing was very likely to have increased BA for the sub-region with the
1091 highest burned areas in August-September 2024, with a 90% likelihood of increased burned
1092 area in the factual simulations compared to the counterfactual (**Figure 14**). The amplification

factor (AF) was 1.91, albeit with a wide uncertainty range [0.98–>100] (**Table 6**), suggesting that while the median influence was lower than for regional totals, very large increases in burned area due to climate change cannot be ruled out. A similar likelihood of increase and upper bound was found when using ensemble-mean meteorology for the counterfactual.

The risk ratio for these sub-regional extremes was 2.3 (**Table 6**), indicating more than twice the likelihood of observing similar extreme burned area under current anthropogenic conditions relative to a natural climate.

As with Northeast Amazonia, the anthropogenic influence appears less pronounced for the most severely affected areas than for the region overall. This could reflect local fire–moisture–fuel feedbacks limiting amplification where BA was already high, or shifts in fire-prone zones expanding regional totals without intensifying extremes. Further investigation into local factors such as wetlands and fuel constraints will be key to understanding why the climate signal appears weaker in the areas that burn most. One possible explanation is that wetlands and other moisture-rich ecosystems may help buffer fire activity, even as climate conditions change. Another contributing factor could be land use in these extreme fire areas. For example, fire suppression in human-managed landscapes may interact with climate drivers in ways that reduce the strength of attribution signals.

S2.2.2.2 Southern California

Area/Time: *Sub-regional extremes/Aug-Sep 2024*
Variable: *Burned Area*
Attribution Type: *Anthropogenic climate forcing*
Includes: *Greenhouse gases, aerosols, and land-use change effects on climate*

Due to the relatively small size of the Southern California study region, the identified sub-regional extremes correspond to a single model grid cell thus limiting the ability to capture nuances of the distinct fire regimes and mesoscale factors associated with Santa Ana winds (Kolden and Abatzoglou, 2018). As the attribution results are qualitatively similar to those for the full region for all comparisons (Table 6), we do not discuss a separate analysis of sub-regional extremes here.

S5.2.4 Background Changes in Burned Area this Century - all forcings

S5.2.4.1 Northeast Amazonia

Area/Period: *All region/2003-2019*
Variable: *Background Burned Area*
Attribution Type: *All forcing*
Includes: *All anthropogenic and natural trends in climate, population density, land use and land cover change*

When both climate and socioeconomic forcings are considered together, their effects largely offset one another, leading to a small and uncertain net change in BA of +1% [-6%, +9%]. In this region, we observe that the effects of climate change and socio-economic factors on BA have approximately counteracted to produce no clear overall change in background levels of BA this century.
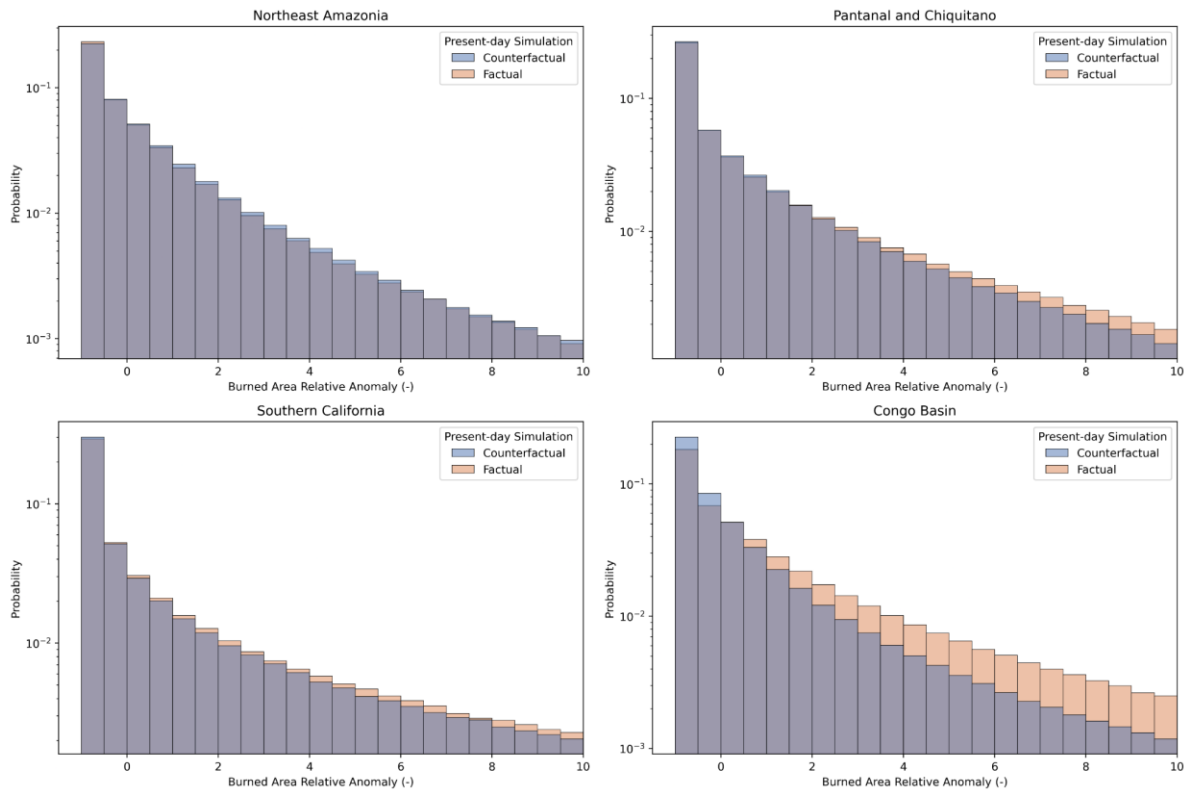
1140
1141 **Figure S24:** Change in median BA due to total climate forcing from FireMIP. Present day BA
1142 (2003-2019) for factual (historical forcing, orange) and counterfactual (detrended climate,
1143 blue). Probability is shown on a log scale.
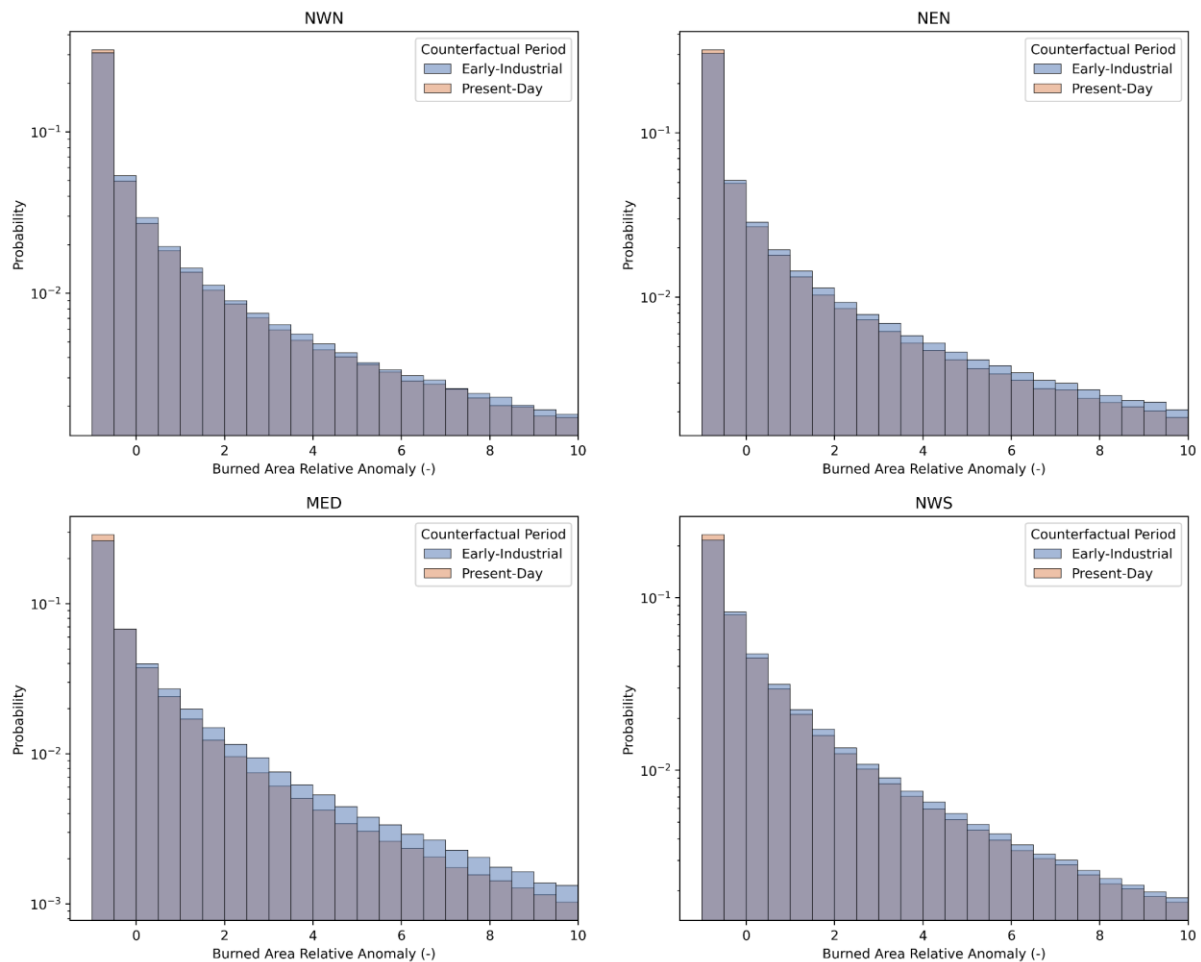
Figure S25: Change in median BA anomaly due to socioeconomic factors (population and land-use change) from FireMIP. Present day BA (2003-2019) for counterfactual (detrended climate, orange) compared to early-industrial (1901-1917) in the counterfactual (detrended climate, blue), for AR6 regions. Top row: North West North America (NWN, LEFT) and North East North America NEN (RIGHT). Bottom row: Mediterranean (MED, LEFT), and North West South America (NWS, RIGHT). Probability is shown on a log scale.

S5.2.4.2 Pantanal and Chiquitano

Area/Period: *All region/2003-2019*
Variable: *Background Burned Area*
Attribution Type: *All forcing*
Includes: *All anthropogenic and natural trends in climate, population density, land use and land cover change*

When considering the combined effects of climate change and socioeconomic drivers, we estimate a net change in background BA at +3% [-2%, 9%]. This modest and uncertain increase likely reflects offsetting influences, where climate-driven increases in fire activity have been partially counteracted by human-driven factors such as land management, suppression practices, or landscape fragmentation. While the net change is close to zero, the underlying drivers may still be highly active in opposing directions, a dynamic that warrants further investigation to support more effective fire policy and adaptation planning.
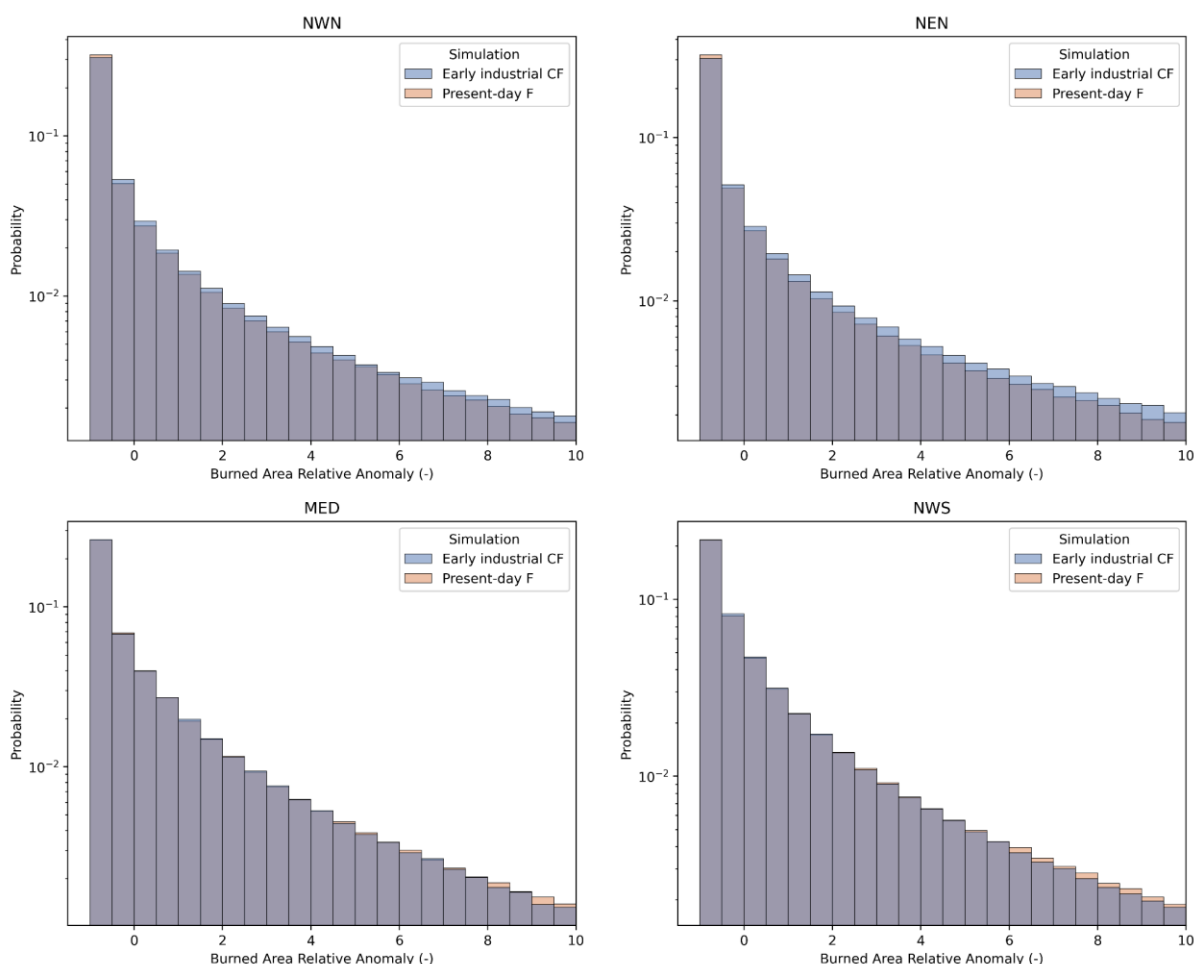
Figure S26: Change in median BA anomaly due to all forcing (climate change and socioeconomic factors) from FireMIP. Present day BA (2003-2019) for factual (historical forcing, orange) compared to early-industrial (1901-1917) in the counterfactual (detrended climate, blue), for AR6 regions. Top row: North West North America (NWN, LEFT) and North East North America NEN (RIGHT). Bottom row: Mediterranean (MED, LEFT), and North West South America (NWS, RIGHT). Probability is shown on a log scale.

S5.2.4.3 Congo Basin

Area/Period: *All region/Jun-Aug 2024*
Variable: *Background Burned Area*
Attribution Type: *All forcing*
Includes: *All anthropogenic and natural trends in climate, population density, land use and land cover change*

When accounting for all anthropogenic and natural trends (i.e. climate change, population dynamics, and land use change) we estimate that total background burned area in the Congo Basin increased by 25% [18%, 33%] over the 2003-2019 period compared to pre-industrial conditions. This result reflects the net outcome of competing influences: while socioeconomic factors appear to have reduced fire activity (as noted in the previous section), climate change has likely increased the underlying fire risk, particularly through changes in temperature, rainfall patterns, and vegetation dynamics.

The net increase in background fire activity does not necessarily imply more fire during extreme years, but it does suggest that the baseline fire environment is shifting. Over time, this could reduce the threshold for extreme events to occur or make recovery between fire seasons more difficult.

S6 Supplementary Material for Section 6

We evaluated the performance of bias-corrected ISIMIP3b climate model data against ERA5 reanalysis in estimating the likelihood of extreme burned area (BA) events across four focal regions.

Northeast   Amazonia:
For the baseline period 2010–2020, reanalysis-based estimates indicate a 0.073% annual probability of experiencing a BA extent comparable to January–March 2024 (Table 7). GCM-based estimates yield a slightly higher likelihood of 0.12%. Although bias correction reduced some discrepancies, differences between GCM and reanalysis data persist.

Pantanal–Chiquitano:
 GCM-based estimates suggest a higher present-day likelihood of August–September 2024-level BA (0.08–0.10% annually) than reanalysis data (0.19%). However, for the most impacted areas (top 5% of grid cells), GCMs and reanalysis align more closely, both indicating a very low annual probability of 0.01–0.03%.

Southern   California:
 During 2010–2020, the annual likelihood of a 2025-scale regional fire event is estimated at 0.38% from reanalysis and 0.34% from bias-corrected GCMs. In the top 5% most affected grid cells, these estimates are slightly lower (0.27% and 0.24%, respectively). This close agreement highlights the effectiveness of bias correction in aligning model projections with observations, supporting confidence in future risk assessments.

Congo   Basin:
 Bias-corrected GCMs closely replicate reanalysis estimates for July 2024-scale fire events, with annual likelihoods of 0.16–0.19% (GCMs) and 0.17% (reanalysis). For the most severely affected areas, both data sources agree on an annual likelihood near 0.01%, indicating strong model fidelity to observed fire risk patterns.
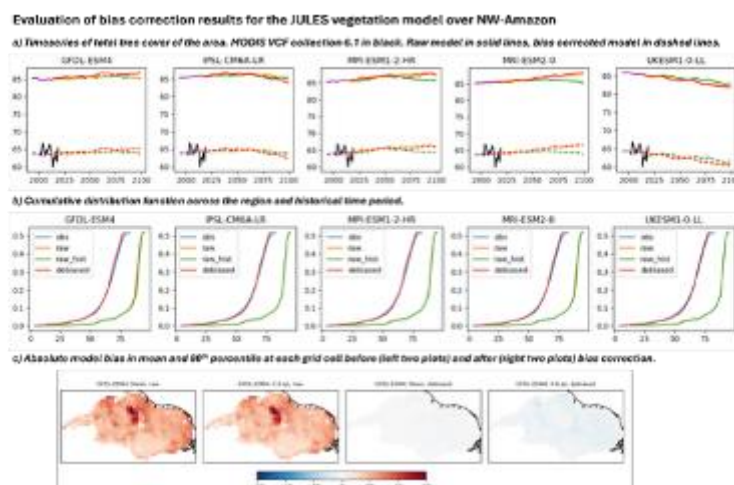
Figure S27: Evaluation of the JULES vegetation model bias adjustment for tree cover over the Amazon region. a) Time series of tree cover over the area (in percent) for different climate models, both with historical and scenario runs, raw model in solid lines, bias corrected models in dashed lines and MODIS VCF in black. b) Cumulative distribution function of tree cover values across region and historical time period for different climate models for observations (blue), raw models (orange), raw historical models (green) debiased models (red). c) Absolute

1231   model bias in mean and 80th percentile for the GFDL-ESM4 climate model before (left two
1232   plots) and after bias adjustment (right two plots).
1233

1234

1235
1236

1237
1238

1239
1240

1241
1242
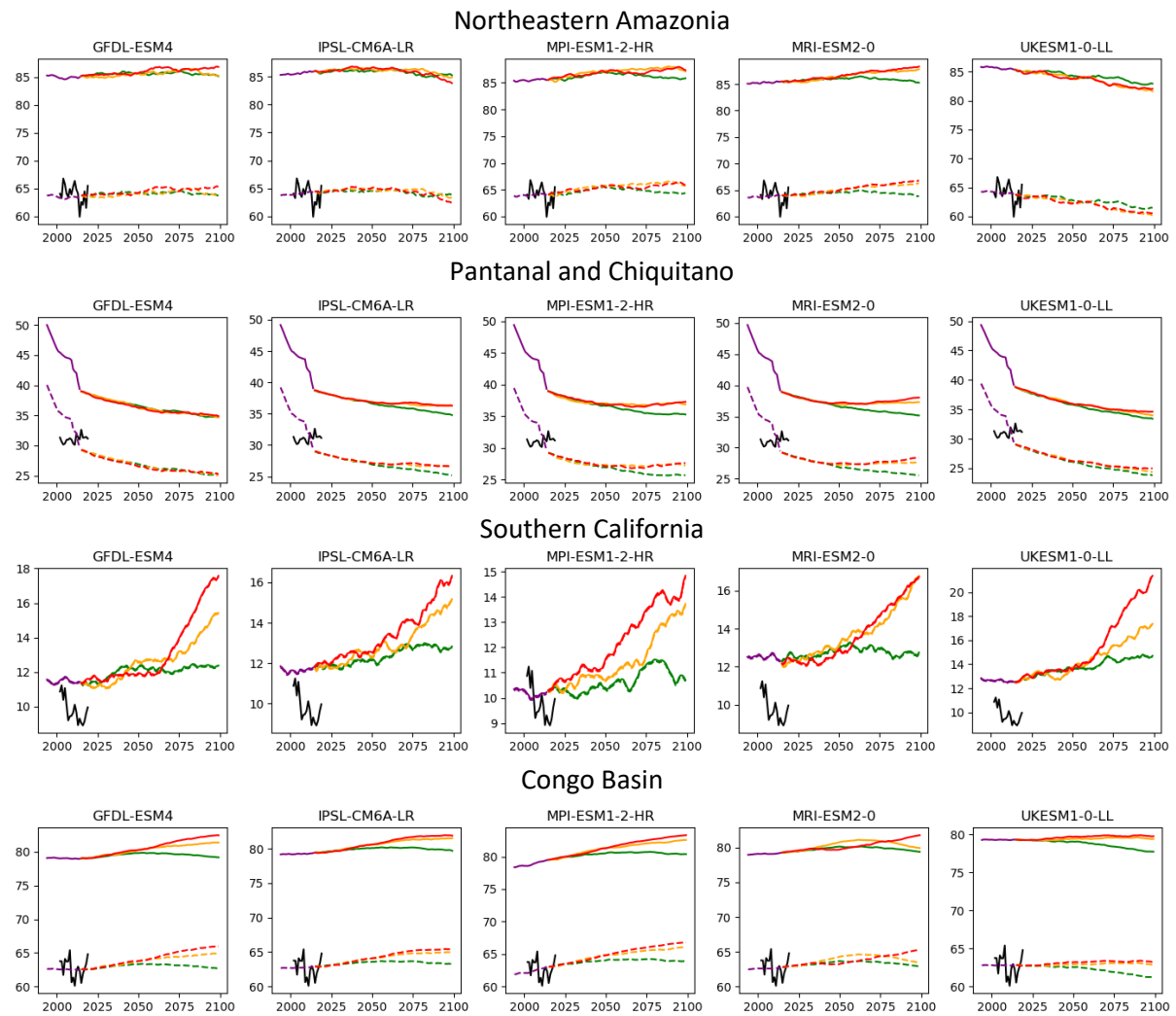
1243 **Figure S28**: Time series of tree cover over each focal region for different climate models,
1244 both with historical and future scenario runs, raw model in solid lines, bias corrected models
1245 in dashed lines and MODIS VCF in black. Note that for Southern California, bias and none-
1246 bias corrected time series overlap one another.
1247
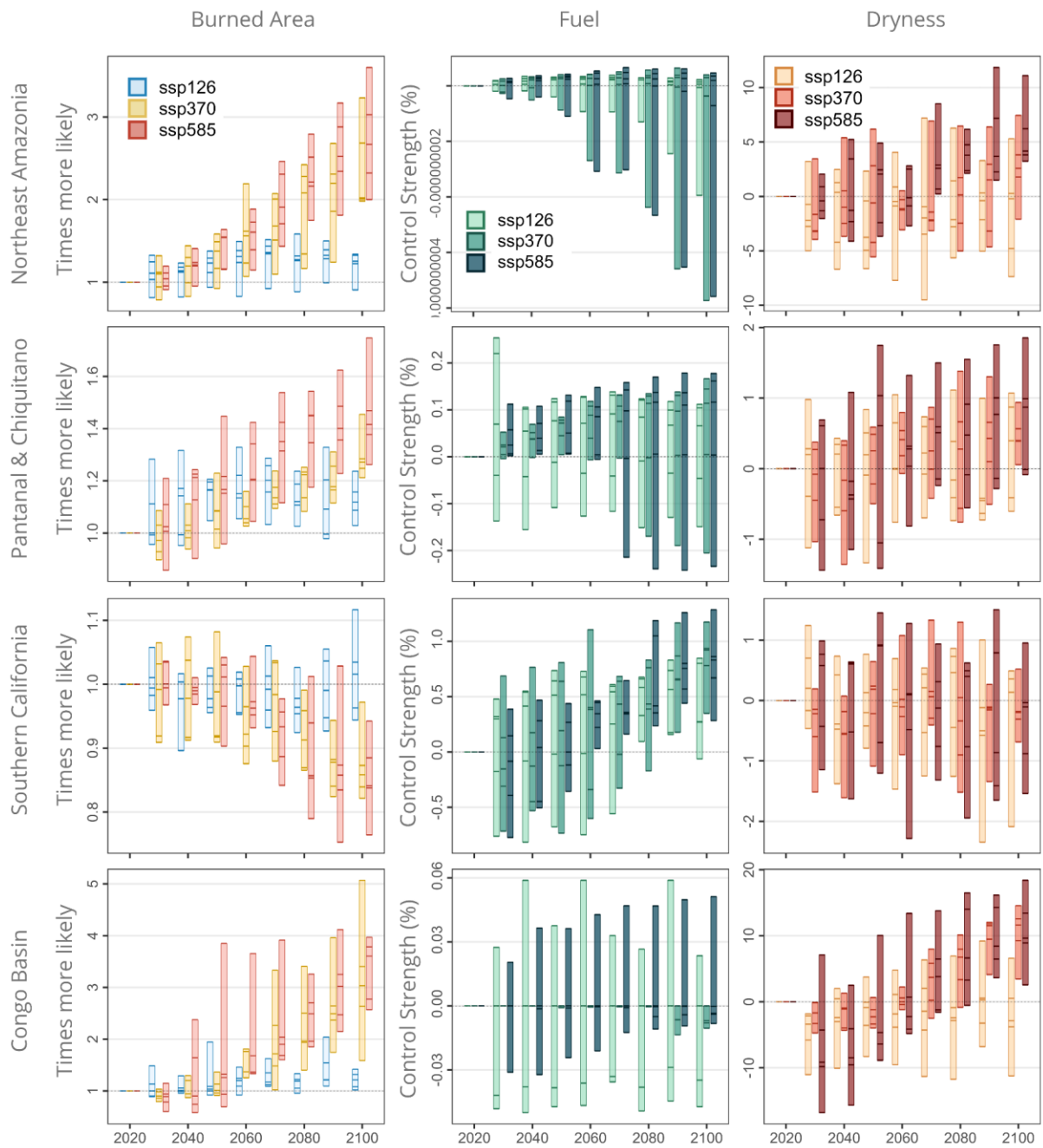
Figure S29: As Figure 18, but for the regions with the highest burned area (at the 95 percentile of burning).

1254
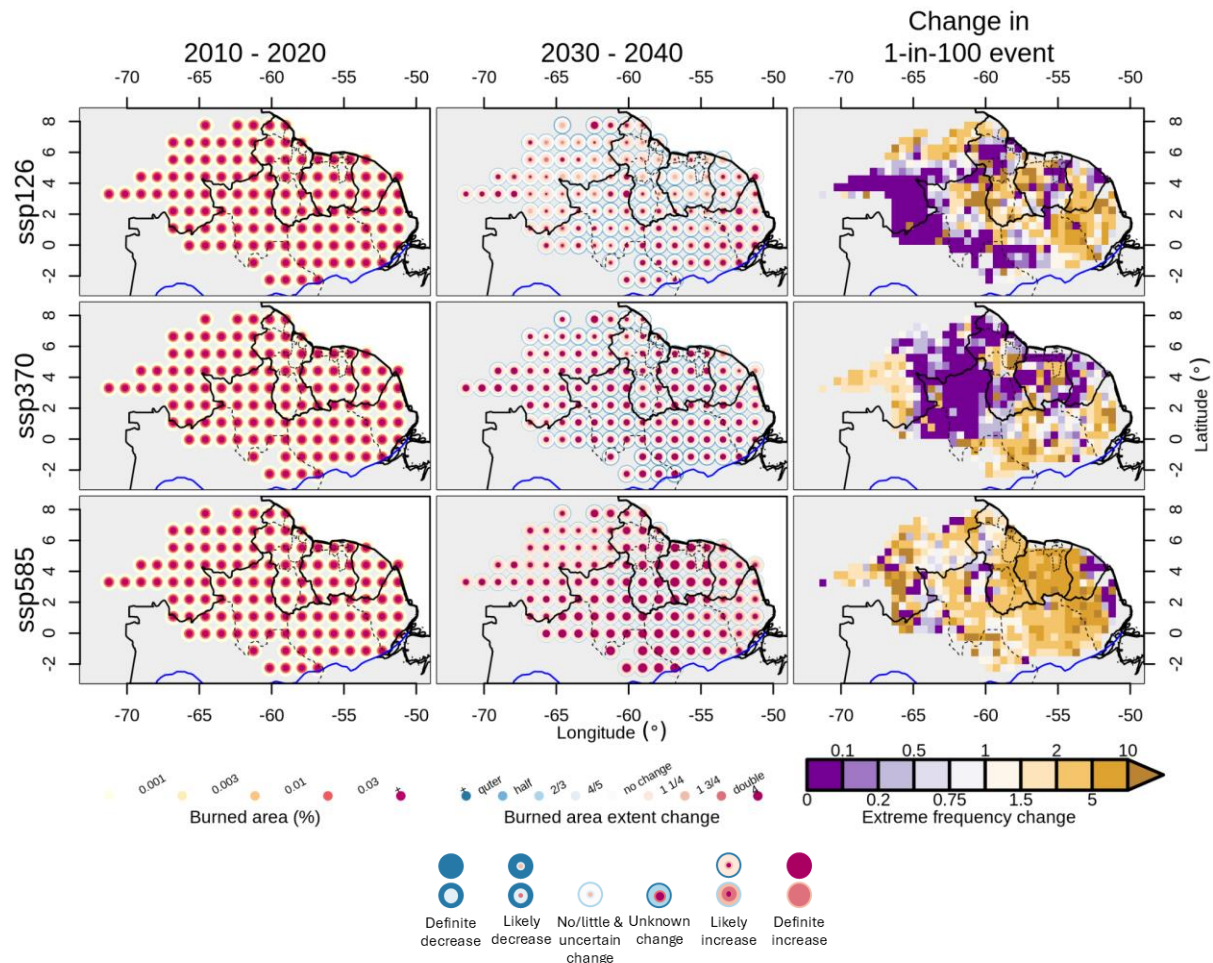
1255
1256 **Figure S30:** Projected changes in January-March 2024 BA over Northeast Amazonia by
1257 2030–2040 under three SSP scenarios, with BA simulated by ConFLAME. **(Left)** Average JFM
1258 BA fraction (%) for 2010–2020. **(Middle)** Relative change in JFM BA extent projected for
1259 2030–2040 period, expressed as a multiplier of 2010–2020 values. **(Right)** Increased (or
1260 decreased) frequency in the 2030s period of a 1-in-100 year event defined for the period
1261 2010–2020, expressed as a multiplier of 2010–2020 values. In the left column, the size of the
1262 dot in each grid cell indicates the likelihood (larger = higher likelihood) of a BA fraction being
1263 greater than the threshold indicated by the coloured dot (see legend at the base). Likewise, in
1264 the middle column the size of the dot varies with likelihood that the BA fraction exceeds the
1265 threshold indicated by the coloured dot (see legend at the base). For example, a large pale
1266 orange dot in the left column indicates a high likelihood of the BA fraction exceeding 0.03%,
1267 whereas a small dark red dot indicates a small (but non-zero) likelihood of the BA fraction
1268 exceeding 0.03%+.

1269
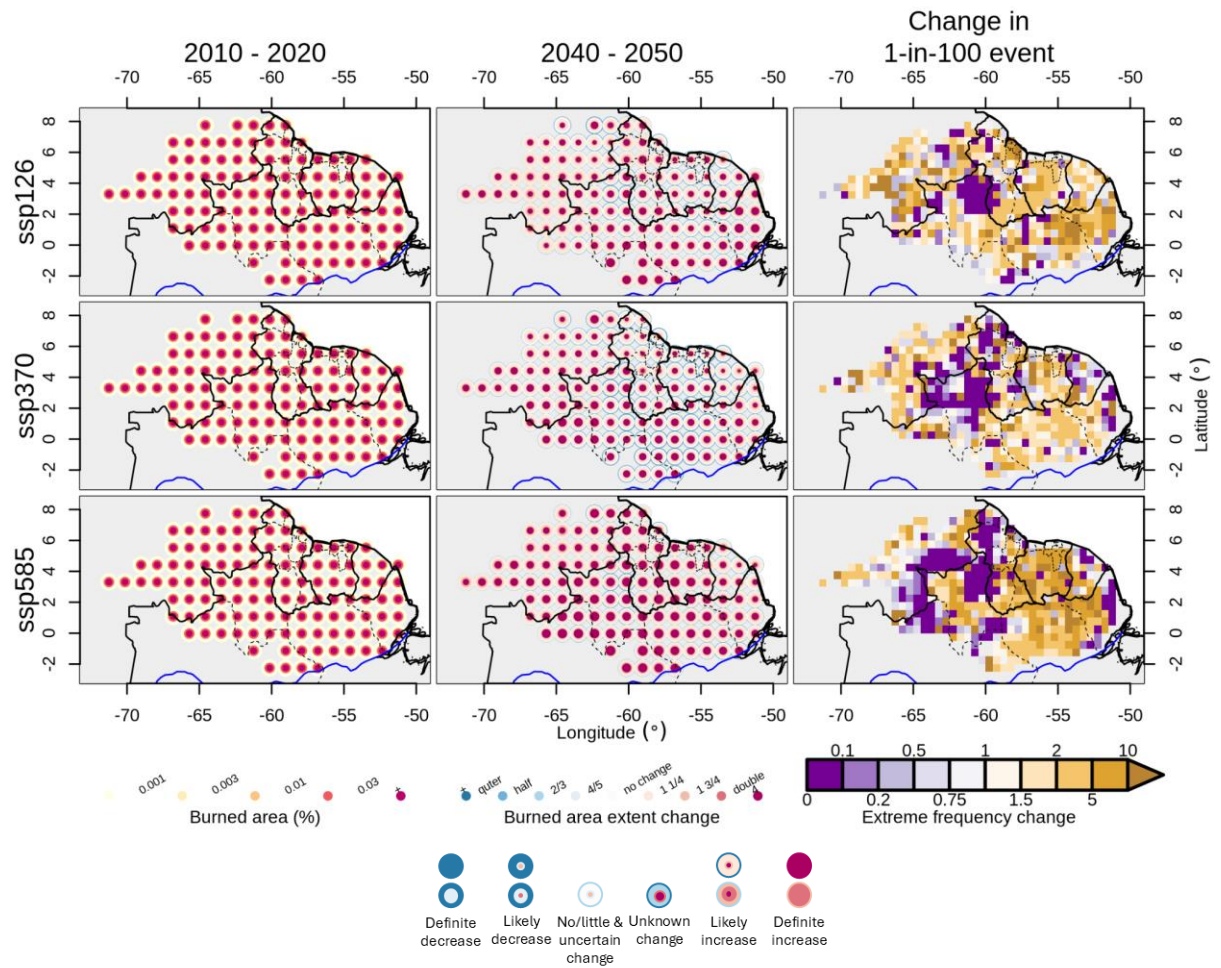
1270
1271 **Figure S31:** Same as **Figure S30** for 2040s.

1272
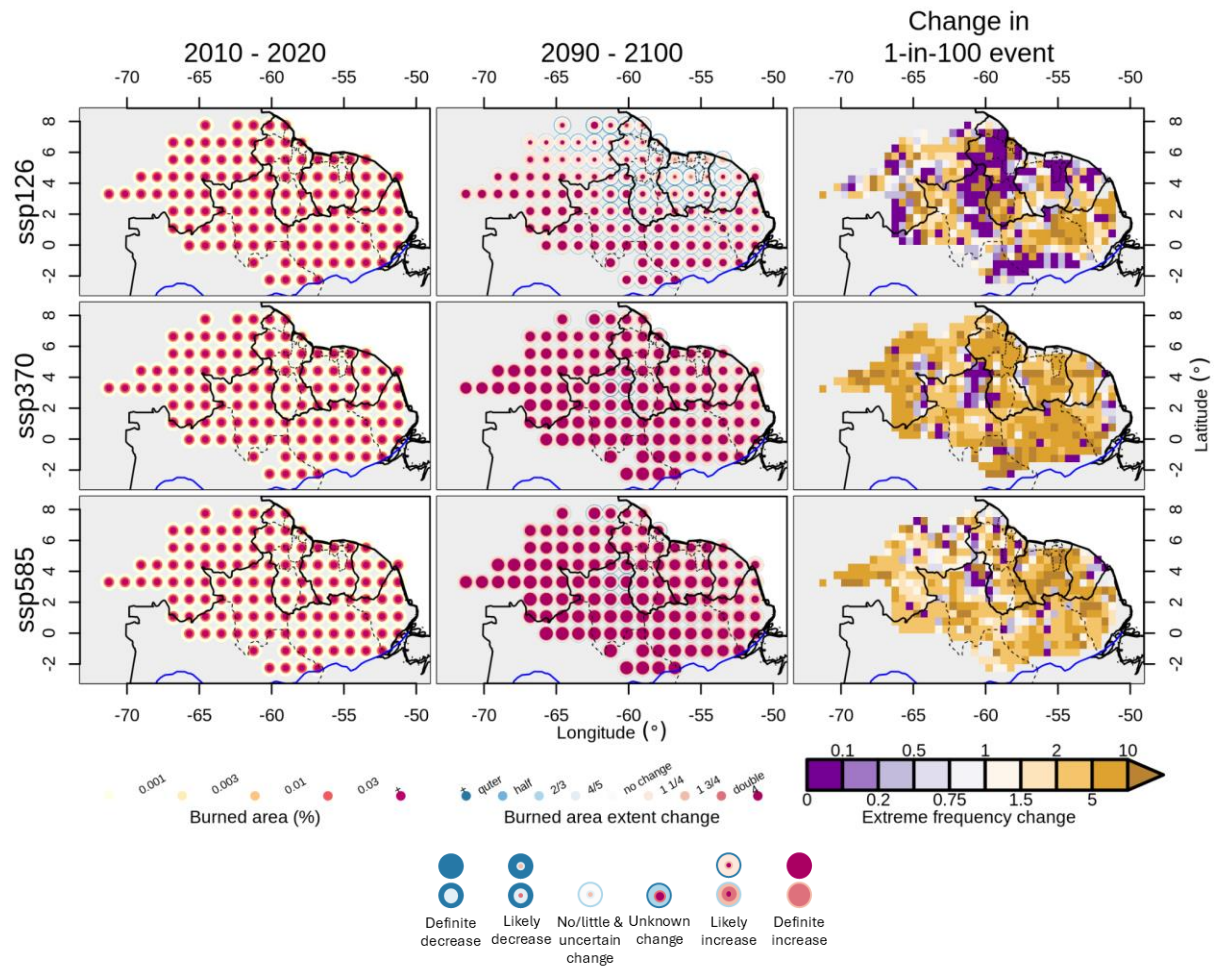
1273
1274 **Figure S32:** Same as **Figure S30** for 2090s.
1275
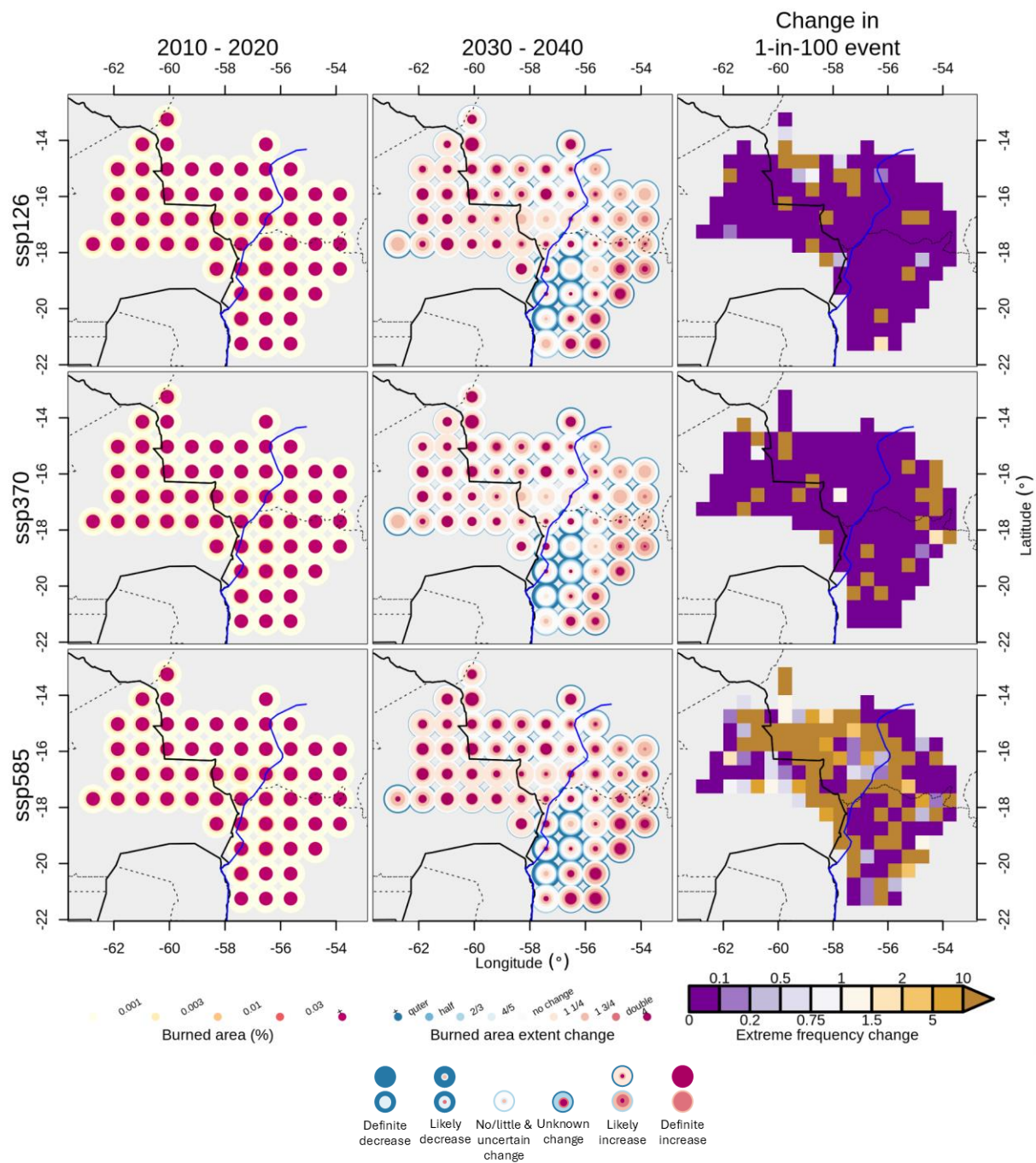
Figure S33: Same as **Figure S30** for August-September 2024, Pantanal and Chiquitano

1281
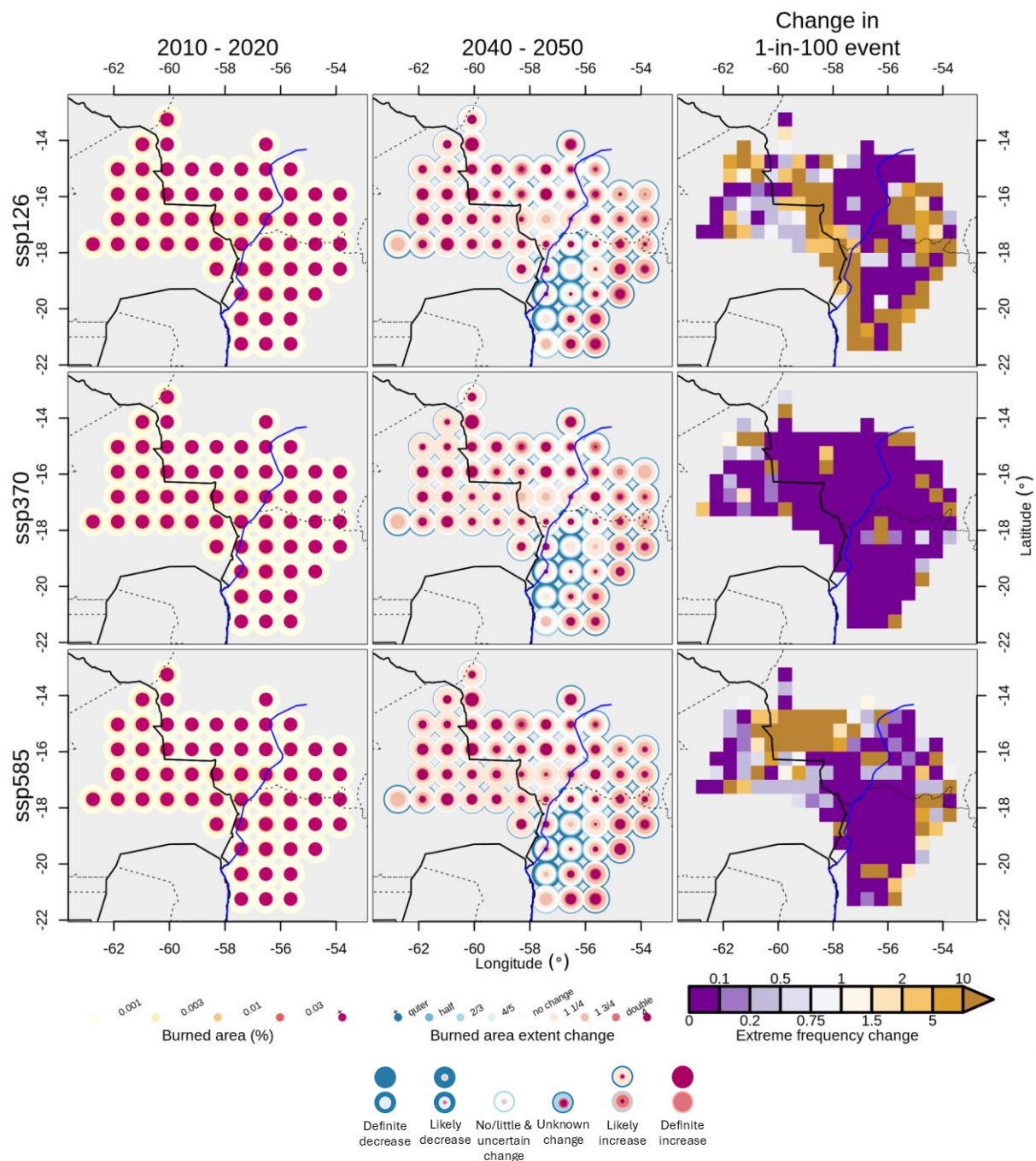
1282
1283 **Figure S34:** Same as **Figure S30** for 2040s.
1284

1285
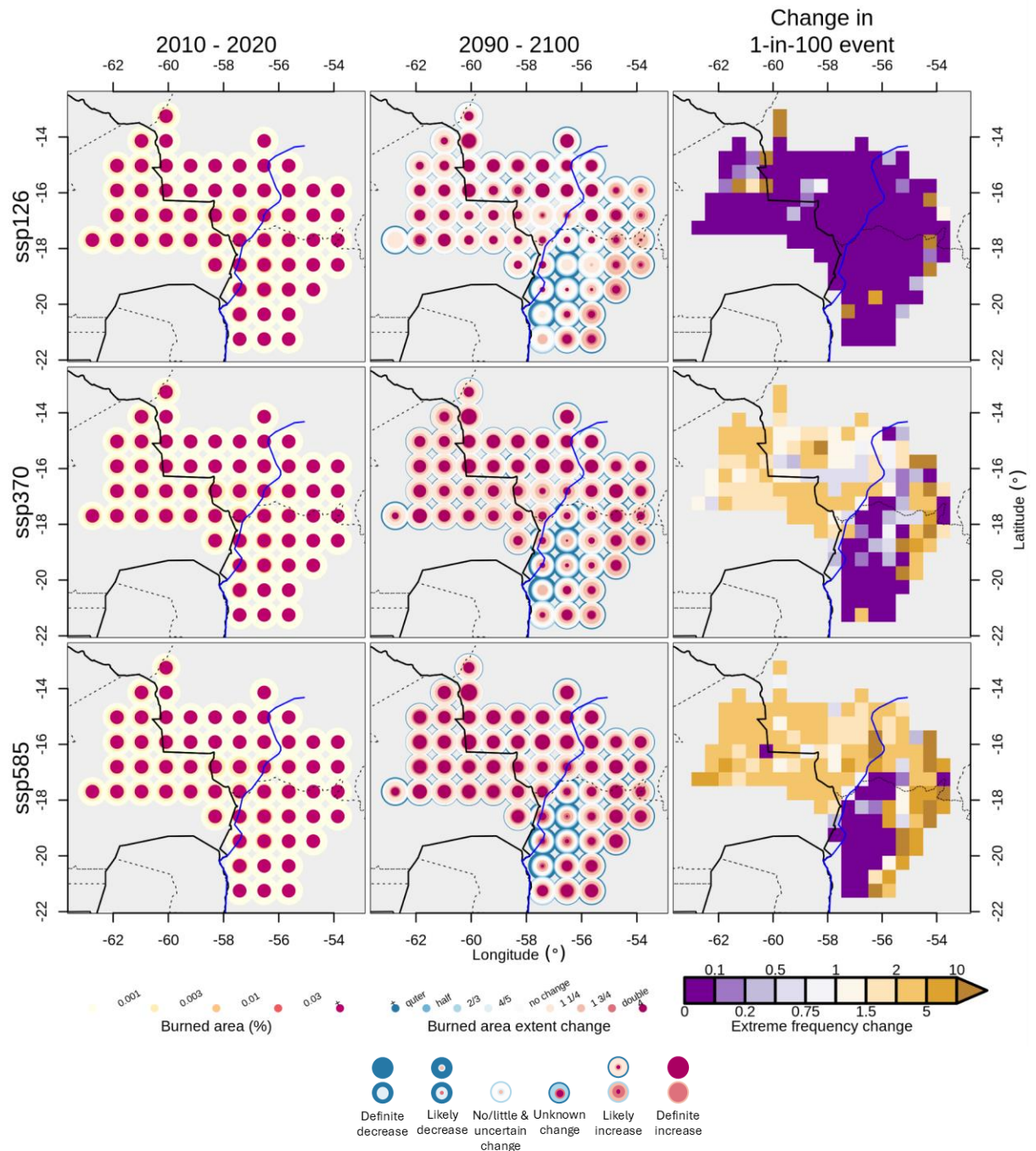
1286
1287 **Figure S35:** Same as **Figure S30** for 2090s.
1288
1289
1290

1291
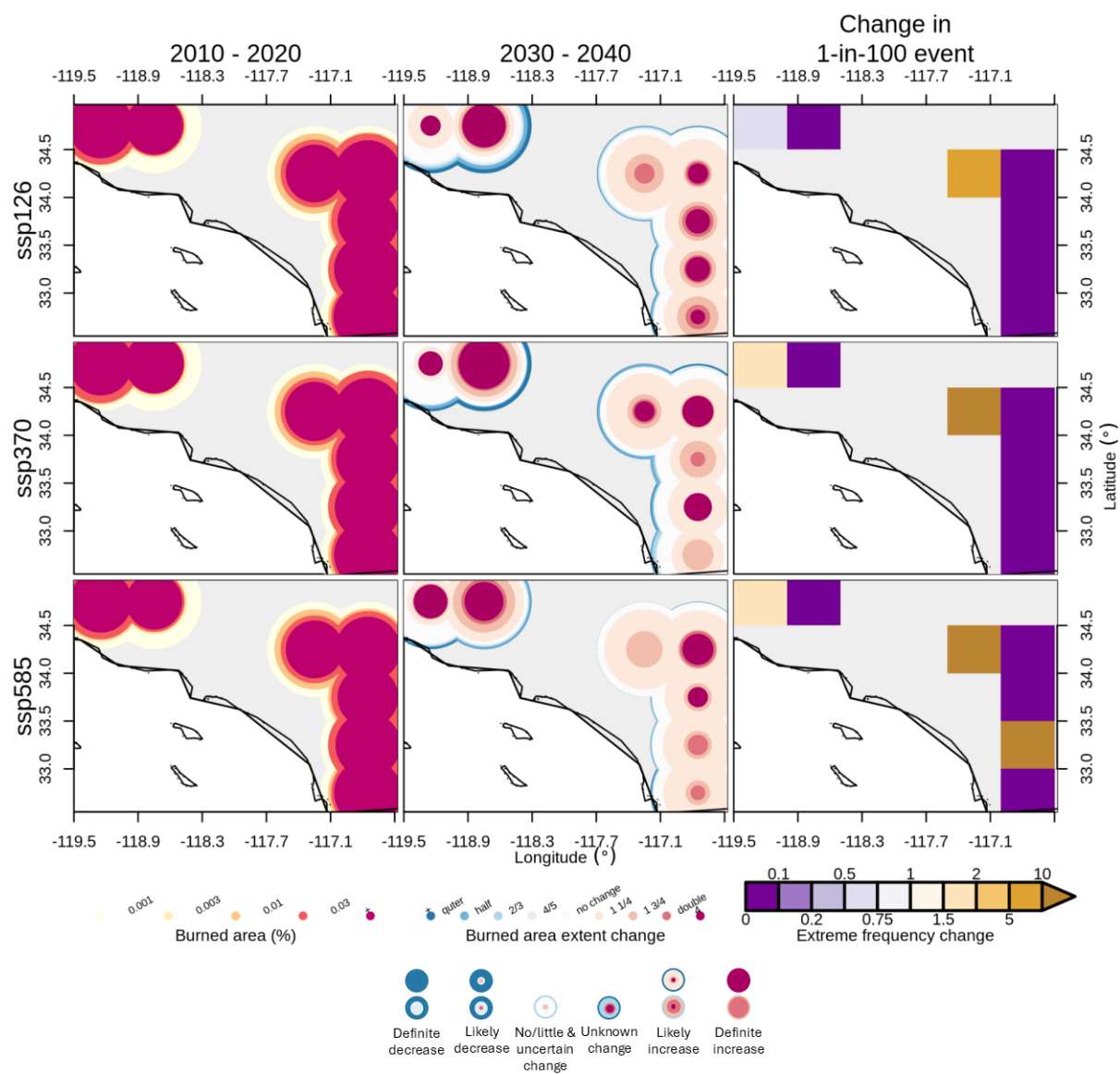
1292

1293
1294 **Figure S36:** Same as **Figure S30** for July 2025, Southern California
1295

1296
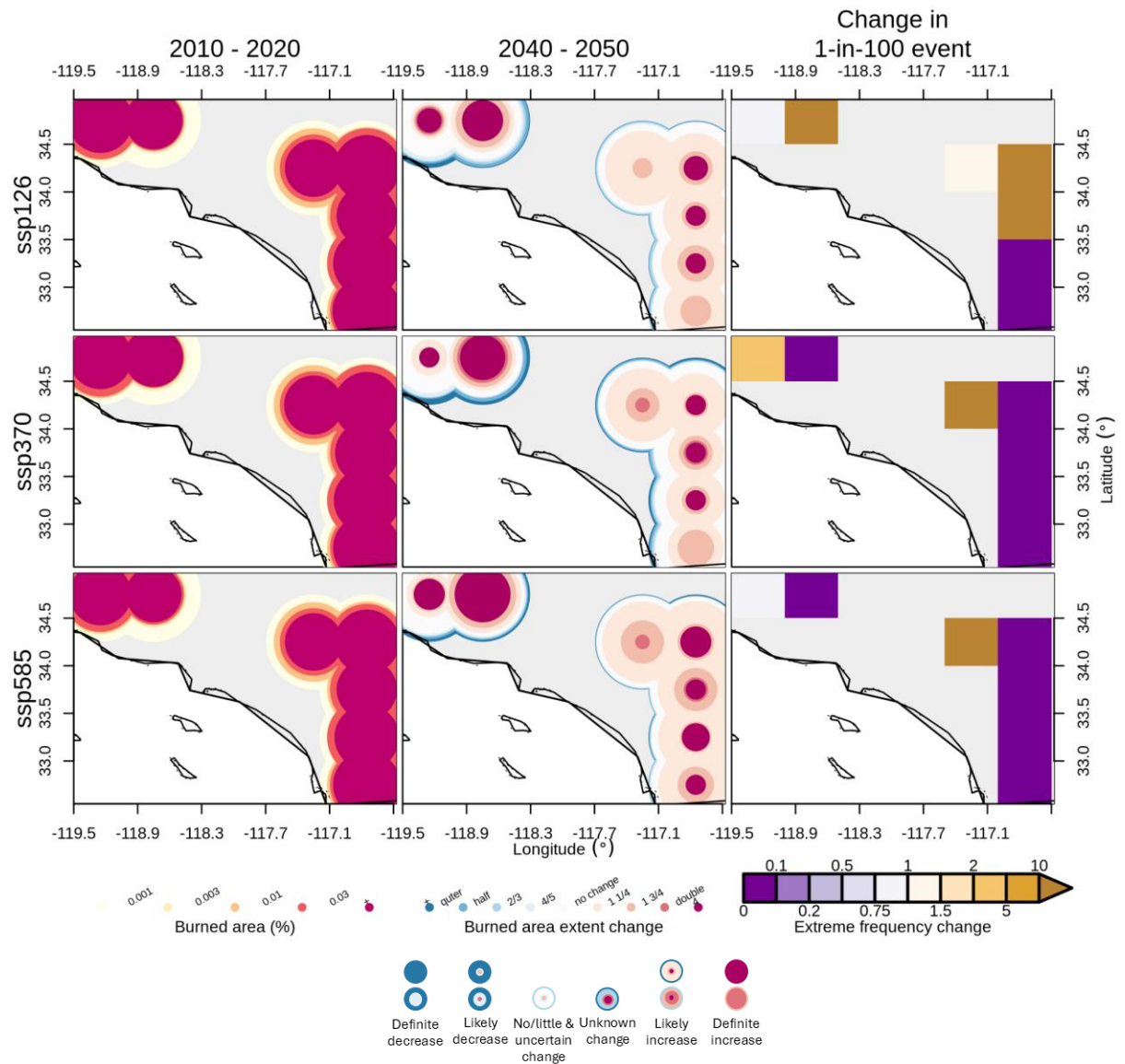
1297
1298
1299 **Figure S37:** Same as **Figure S36** for 2040s.
1300
1301

1302
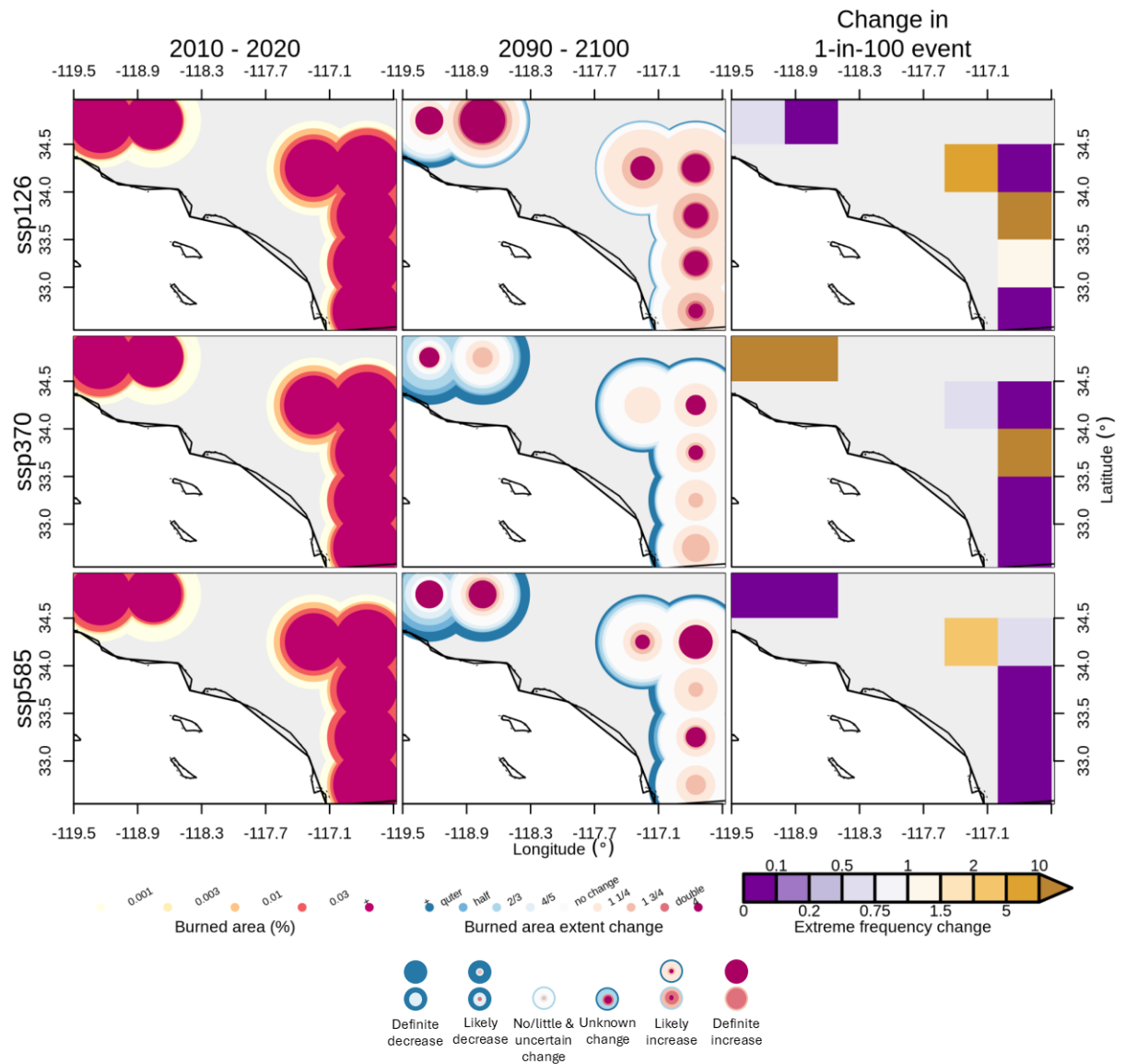
1303
1304 **Figure S38:** Same as **Figure S36** for 2090s.

1305
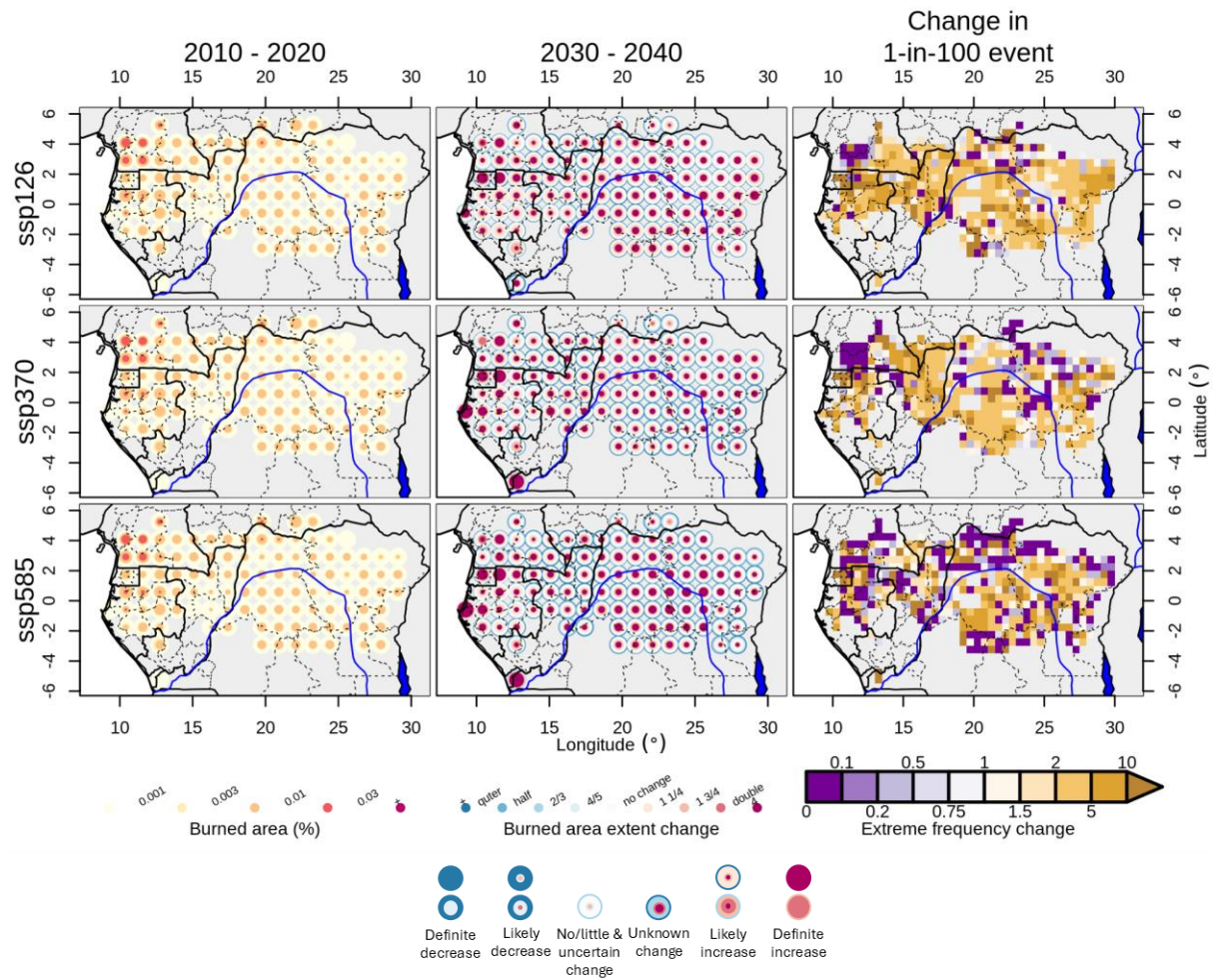
1306
1307 **Figure S39:** Same as **Figure S30** for July, August 2025, Congo Basin

1308
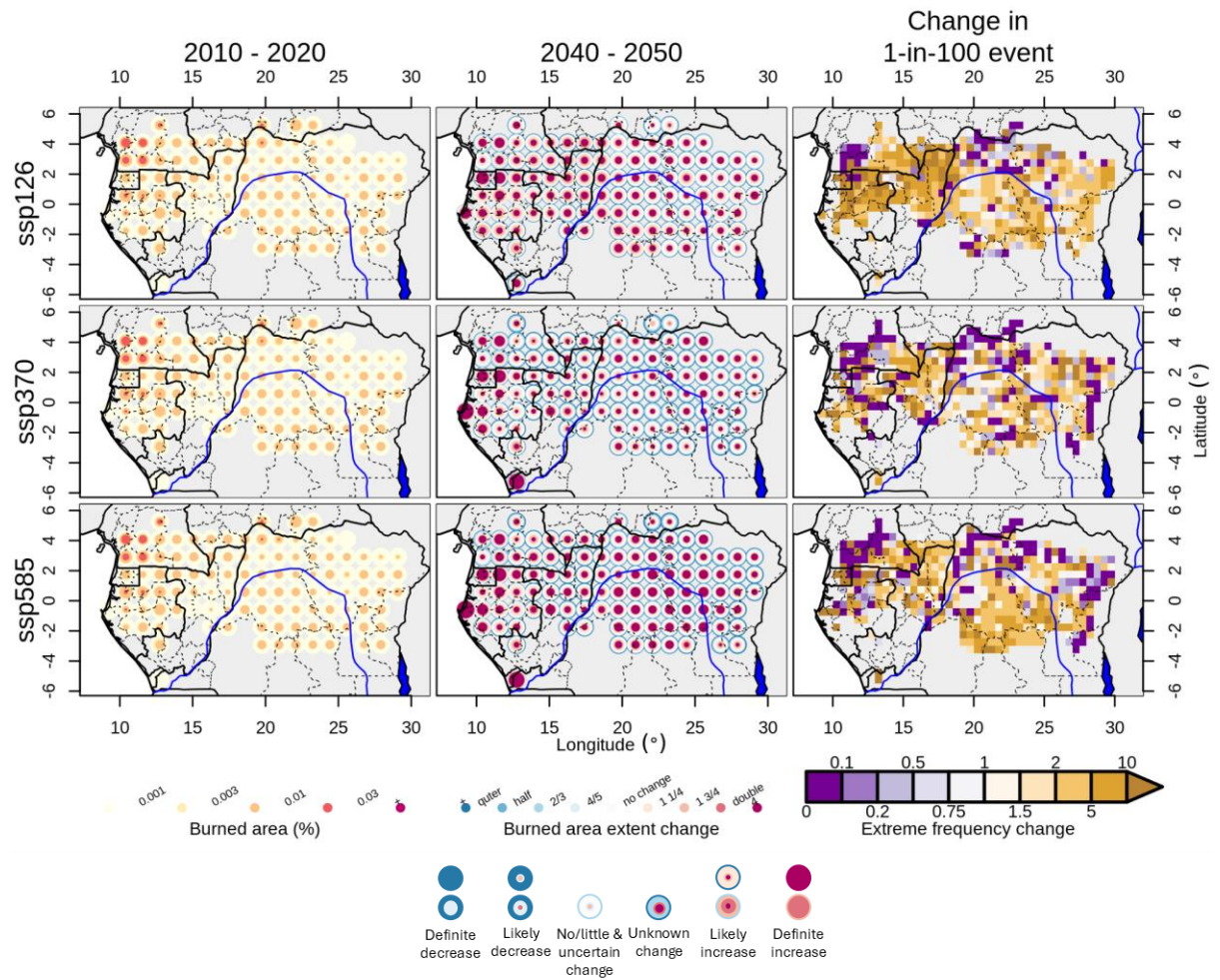
1309
1310 **Figure S40:** Same as **Figure S39** for 2040s.

1311
1312
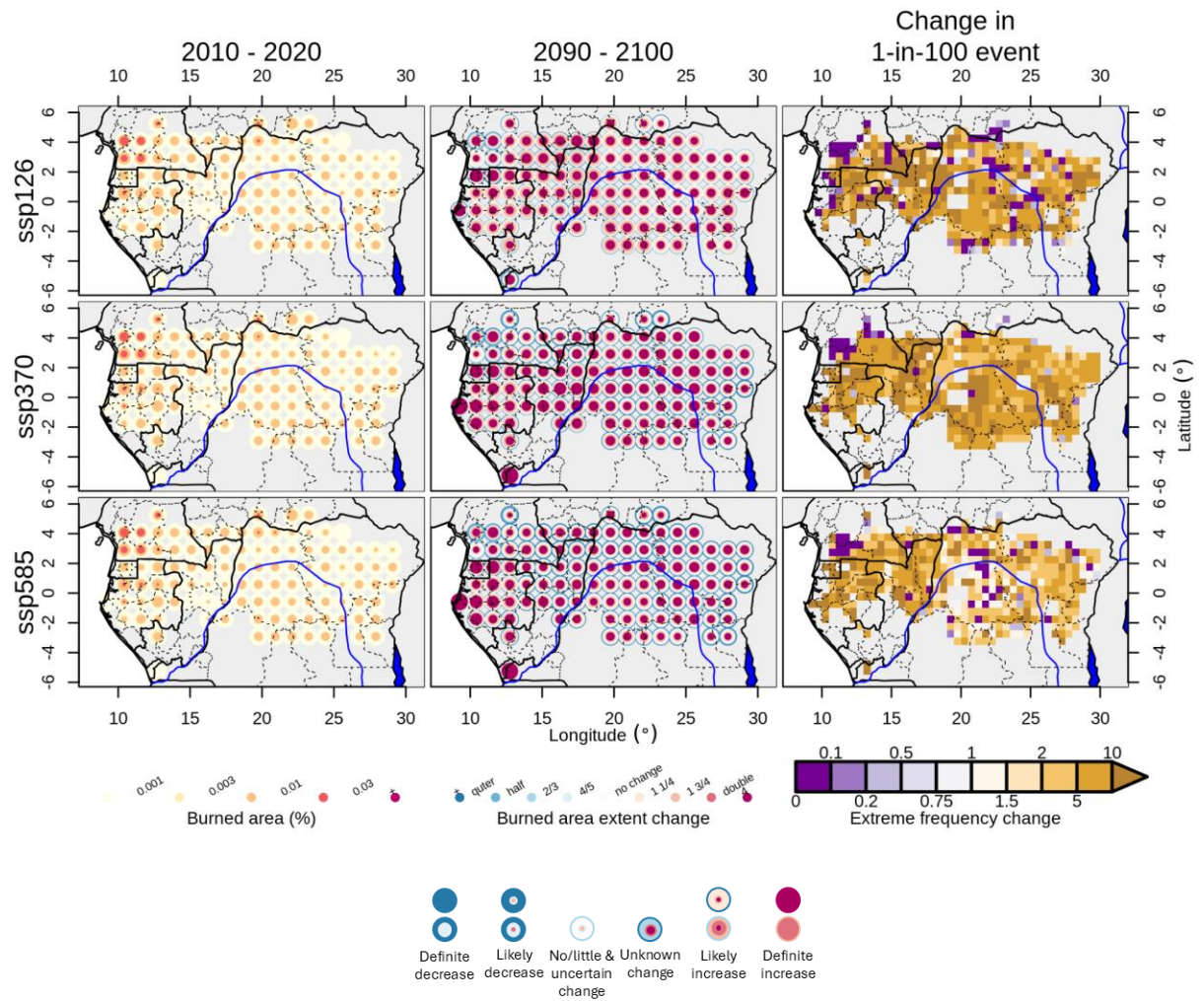
1313
1314 **Figure S41:** Same as **Figure S39** for 2090s.
1315

1316
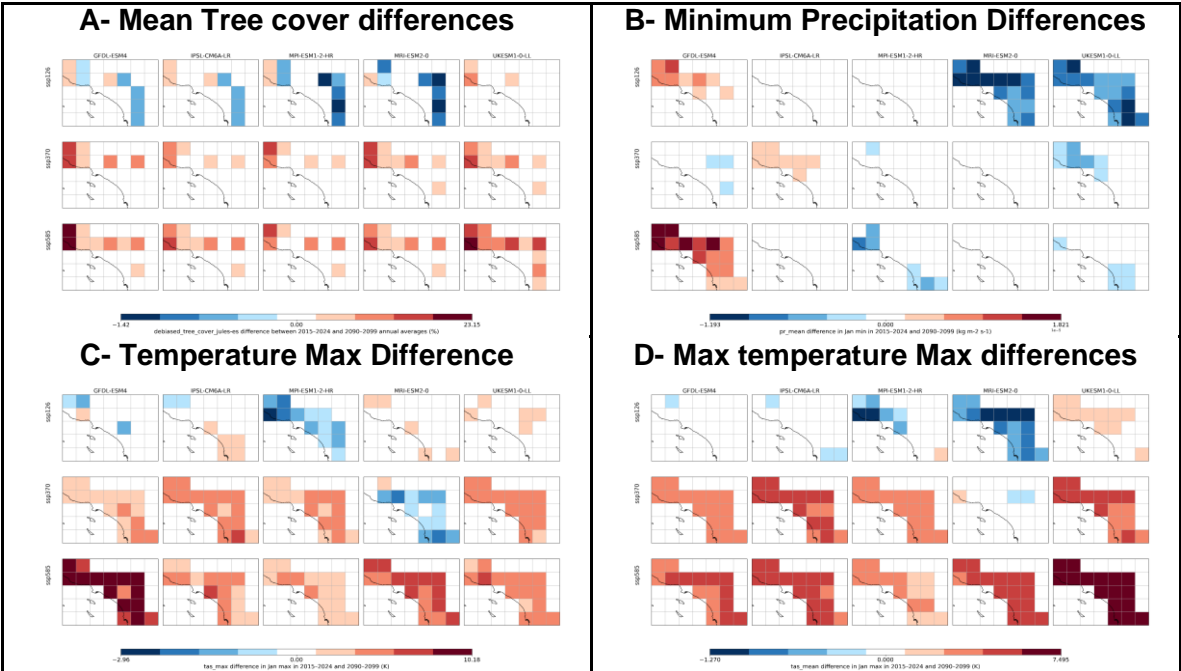
1317 **Figure S42** Future projections of key bioclimate drivers of fire for Southern California,
1318 expressed as difference 2090s vs 2020s. Panels show (A) mean tree cover differences, (B)
1319 minimum precipitation differences, (C) mean maximum temperature differences, and (D)
1320 maximum temperature extremes differences.
1321
1322

S8 Supplementary Material for Appendix A
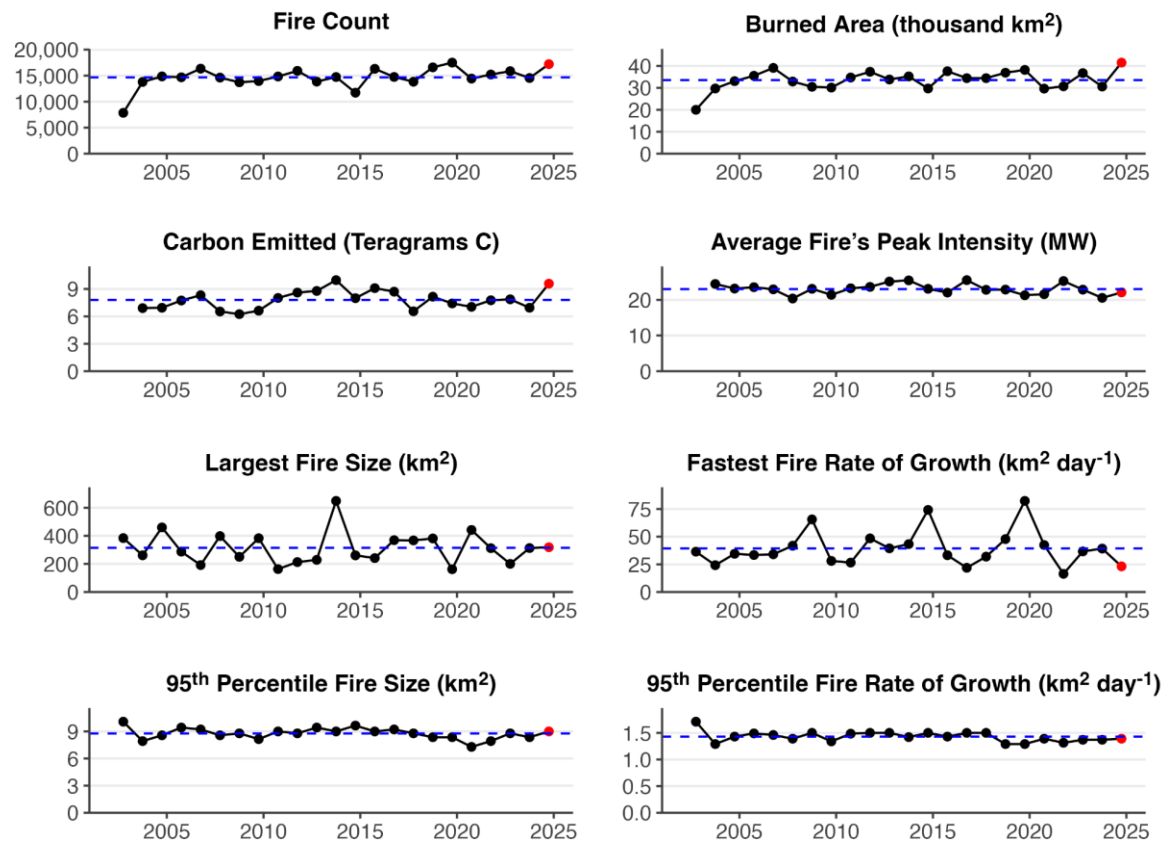
Figure S43: Summary of the 2024-2025 fire season in the Republic of the Congo. Time series show annual fire count, BA, C emissions totals within the region, as well as the average fire's peak fire intensity (95th percentile value of fire radiative power within fire perimeters), the 95th percentile fire size, fastest daily rate of growth, and 95th percentile fire daily rate of growth. Black dots show annual values prior to the latest fire season, red dots the values during the latest fire season, and blue dashed lines the average values across all fire seasons.
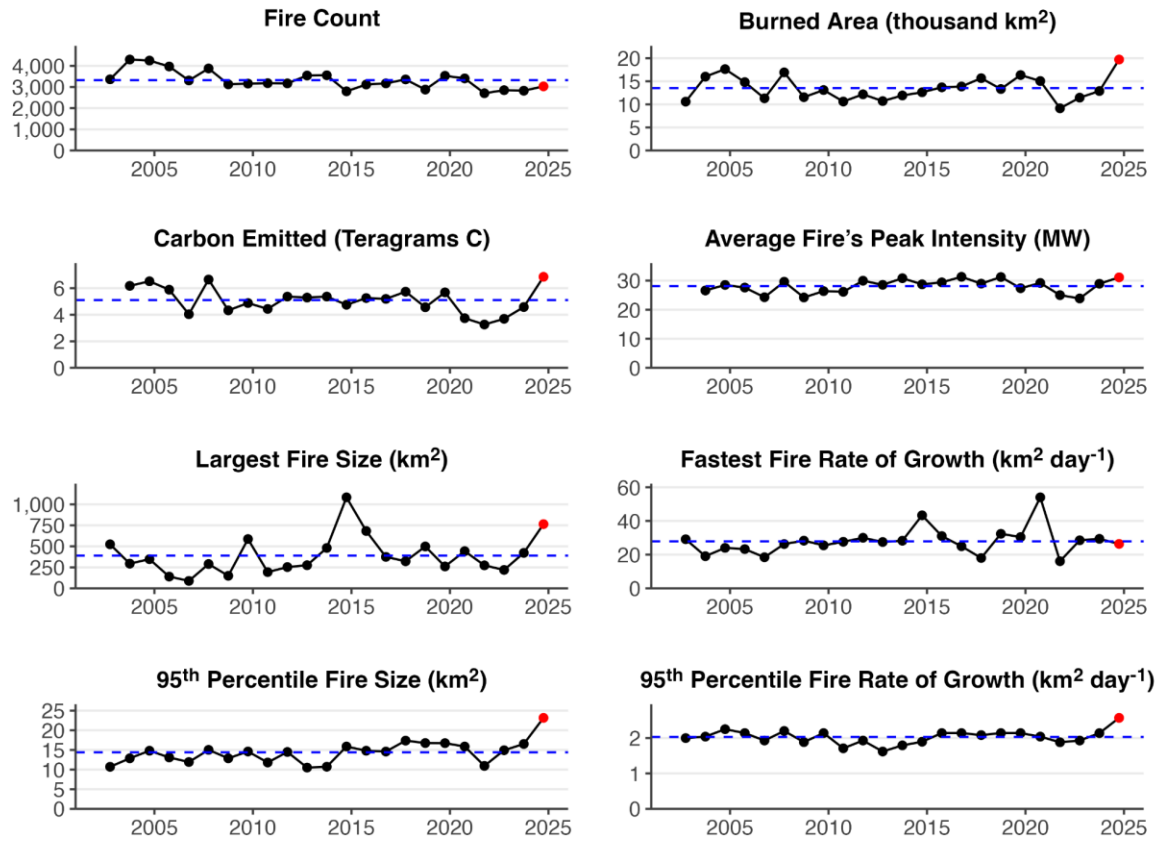
1333
1334   **Figure S44:** Summary of the 2024-2025 fire season in Huíla, Angola, as in Figure A1.
1335
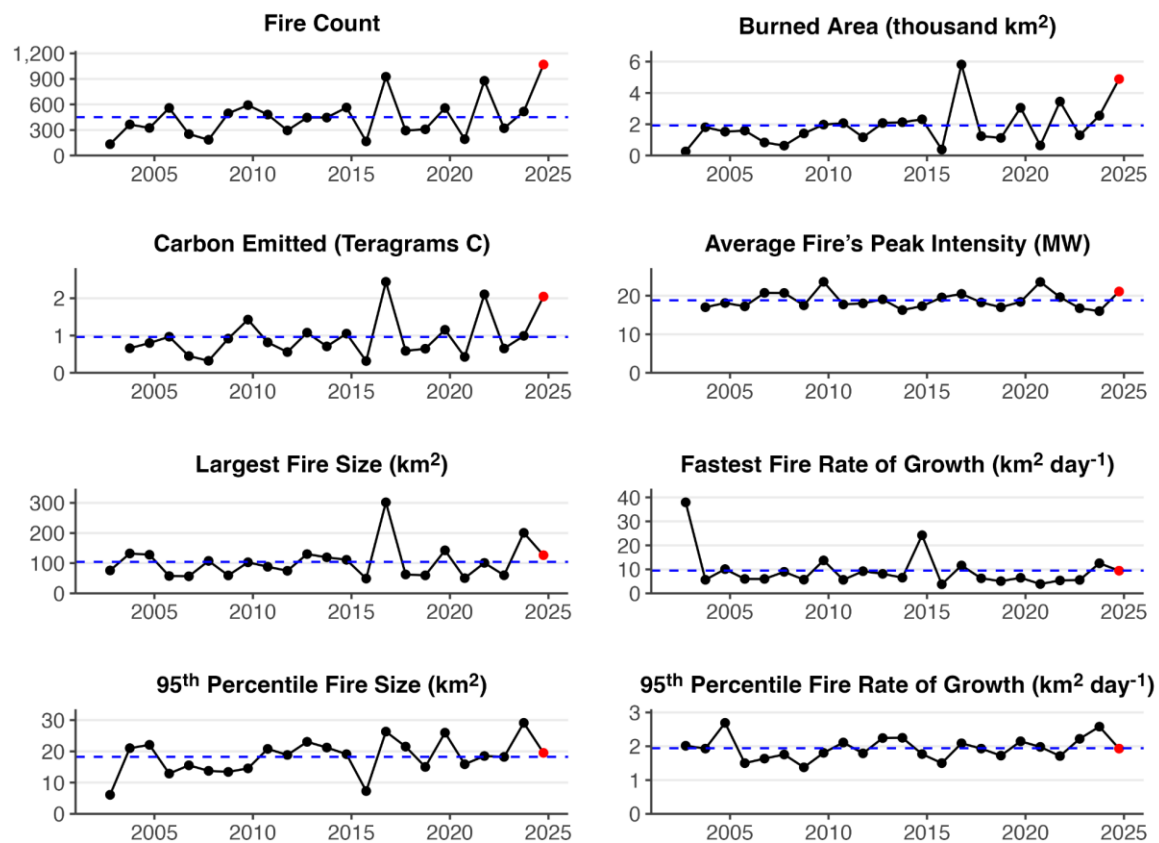
1337 **Figure S45:** Summary of the 2024-2025 fire season in Nepal, as in Figure A1.
1338
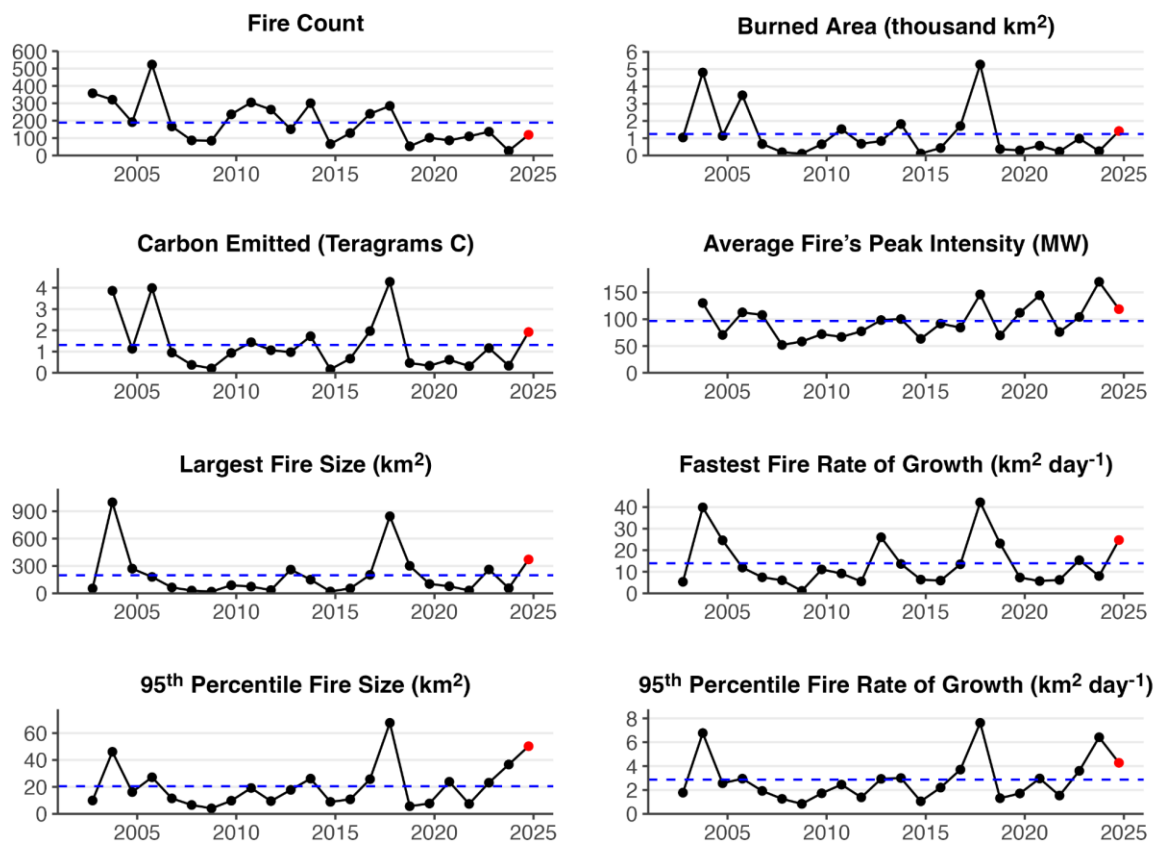
1339
1340   **Figure S46:** Summary of the 2024-2025 fire season in Portugal, as in Figure A1.
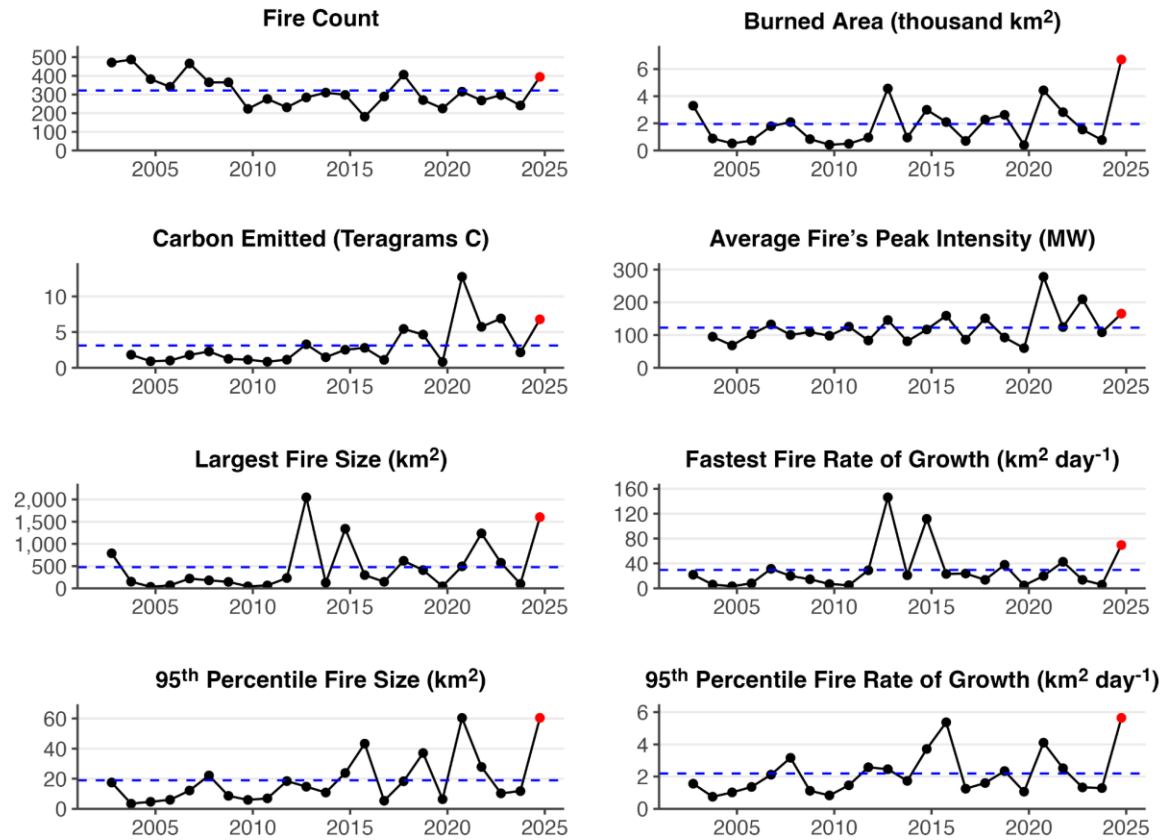
1341

1342   **Figure S47:** Summary of the 2024-2025 fire season in Oregon, USA, as in Figure A1.

S9 Supplementary Material: Extended Model evaluation

HadGEM3-A vs ERA5 meteorology

In this section we present a basic evaluation of the model's performance against ERA5 reanalysis for the physical input variables to the FWI. As the FWI methodology requires a bias correction of the FWI itself, rather than of the input variables, we focus here on assessing the basic physical behaviour of and relationship between those variables. Figures S48- S55 present time series for a number of recent years followed by details of the seasonal cycle over 2024. From these we are able to qualitatively assess the behaviour over these timescales to that in reanalysis, compare any obvious anthropogenic responses to the response to only natural climate forcings and note any clear biases.

Temperature variables typically possess better model performance than those related to precipitation, humidity and wind. For all regions we see that daily mean and maximum temperature possess similar magnitude of variability, absolute values and presence of obvious trends to ERA5. The Amazon and Congo regions see model daily means that are warm biased while daily maximum temperatures are essentially unbiased in all regions, at the relevant part of the seasonal cycle, which is useful for FWI as maximum temperature is the relevant input variable. Temperature is the only variable with significant trends that are obvious over the short period depicted (Congo) but we see that the model captures these, as well as the lack of such in other regions.

For each region the model captures the phasing of the seasonal cycle in precipitation, despite clear biases in magnitude of extremes of the monthly mean. Daily mean surface wind also possess seasonality with features that are captured by the model, generally with high biases. RH anomalies appear to possess both significantly different magnitude of variability and seasonality in more than one region. Together with temperature however these suggest that the appropriate physical relationships between the input variables is present in the model and that the basic meteorology relevant to fire weather events is acceptable.
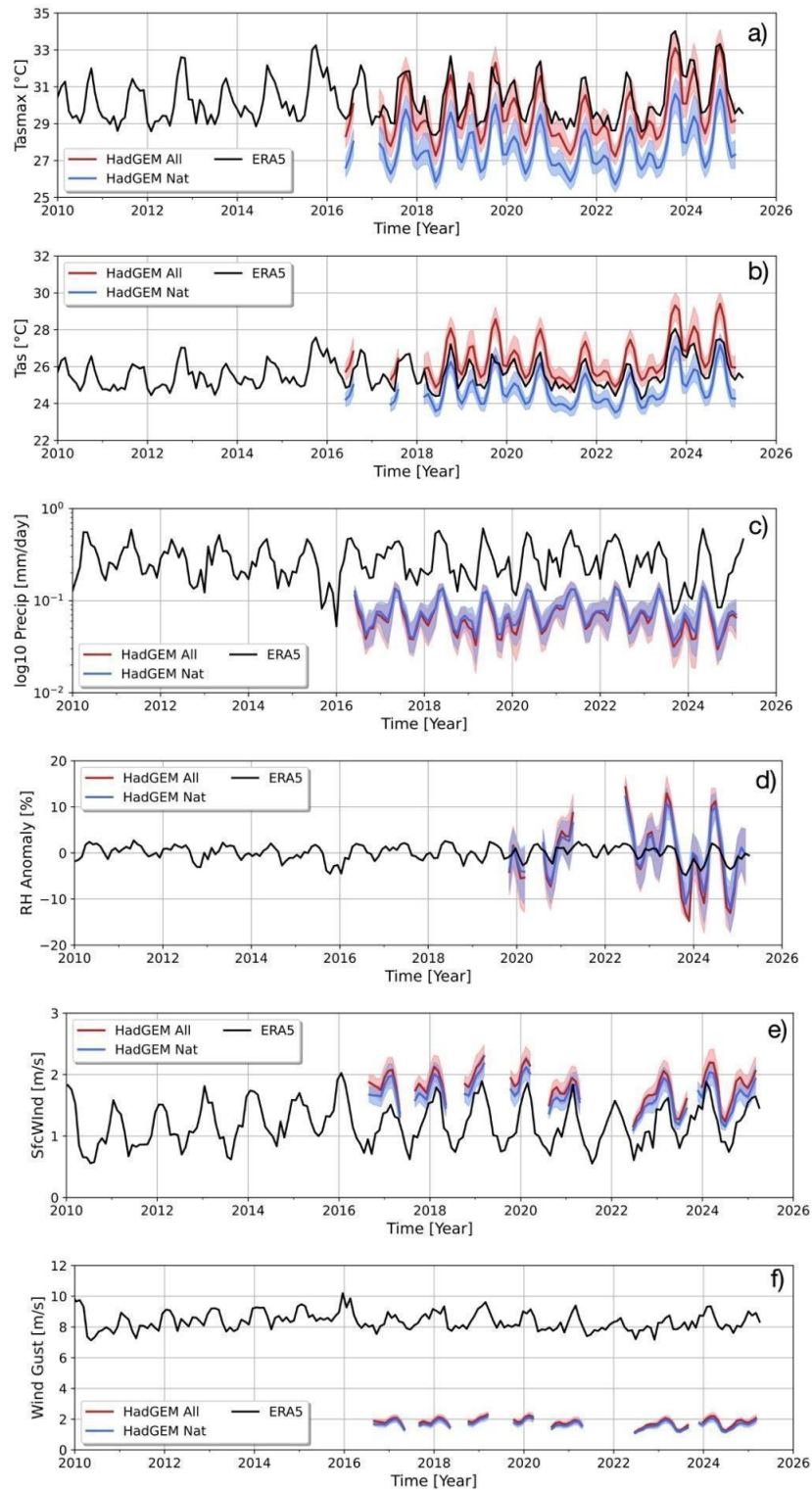
1374
1375 **Figure S48:** January 2010 to April 2025 time series of individual component variables of the
1376 FWI from HadGEM (red: all forcing scenario, blue: natural forcing scenario) compared to ERA5
1377 reanalysis (black) over northeast Amazonia region. We show monthly mean a) daily maximum
1378 temperature, b) temperature, c) total precipitation, d) relative humidity, e) wind speed as well
1379 as f) wind gusts. Shading represents the 5th-95th percentile confidence interval.
1380
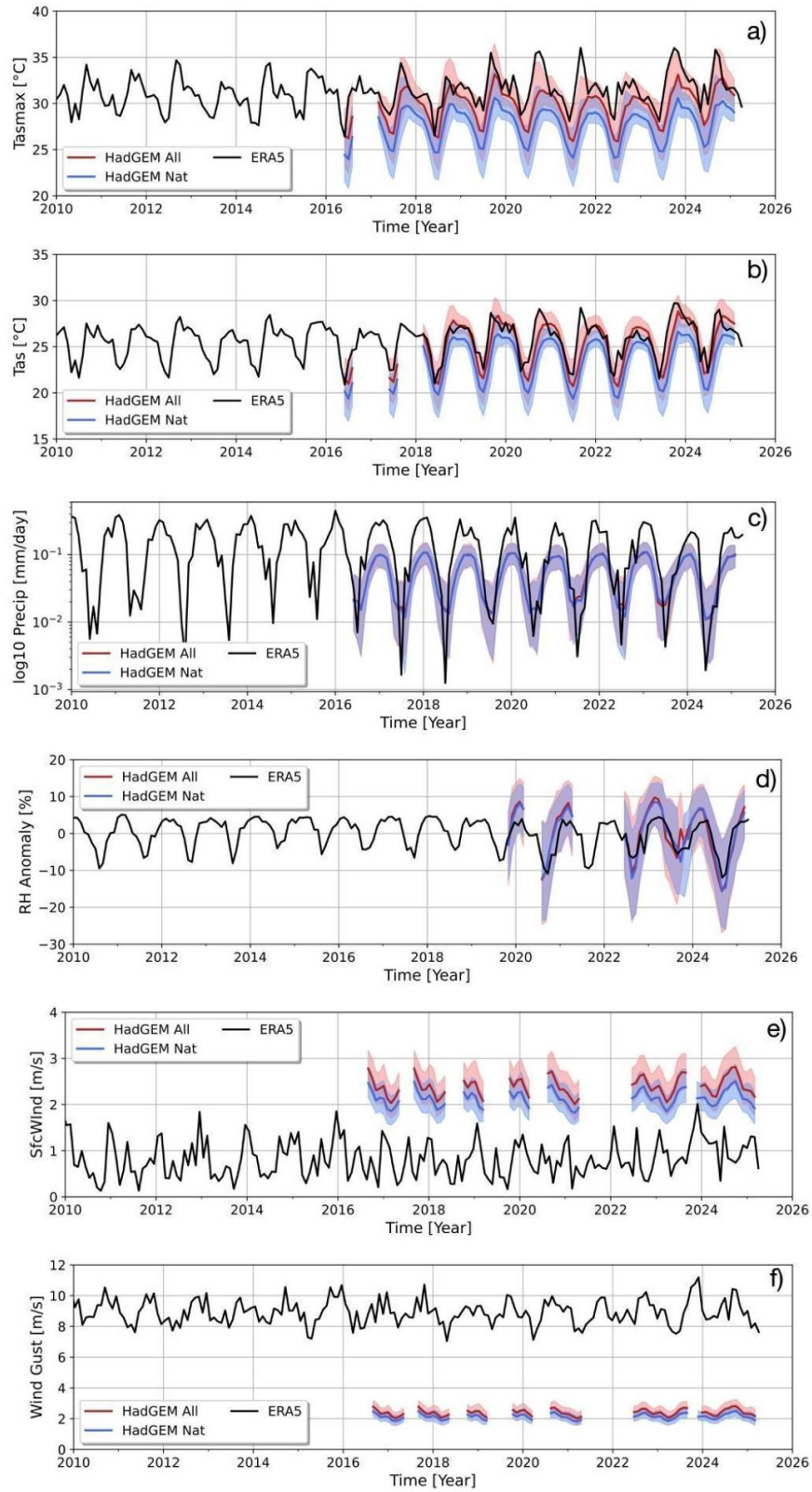
1381
1382 **Figure S49:** Same as in figure S48, but for the Pantanal-Chiquitano.
1383
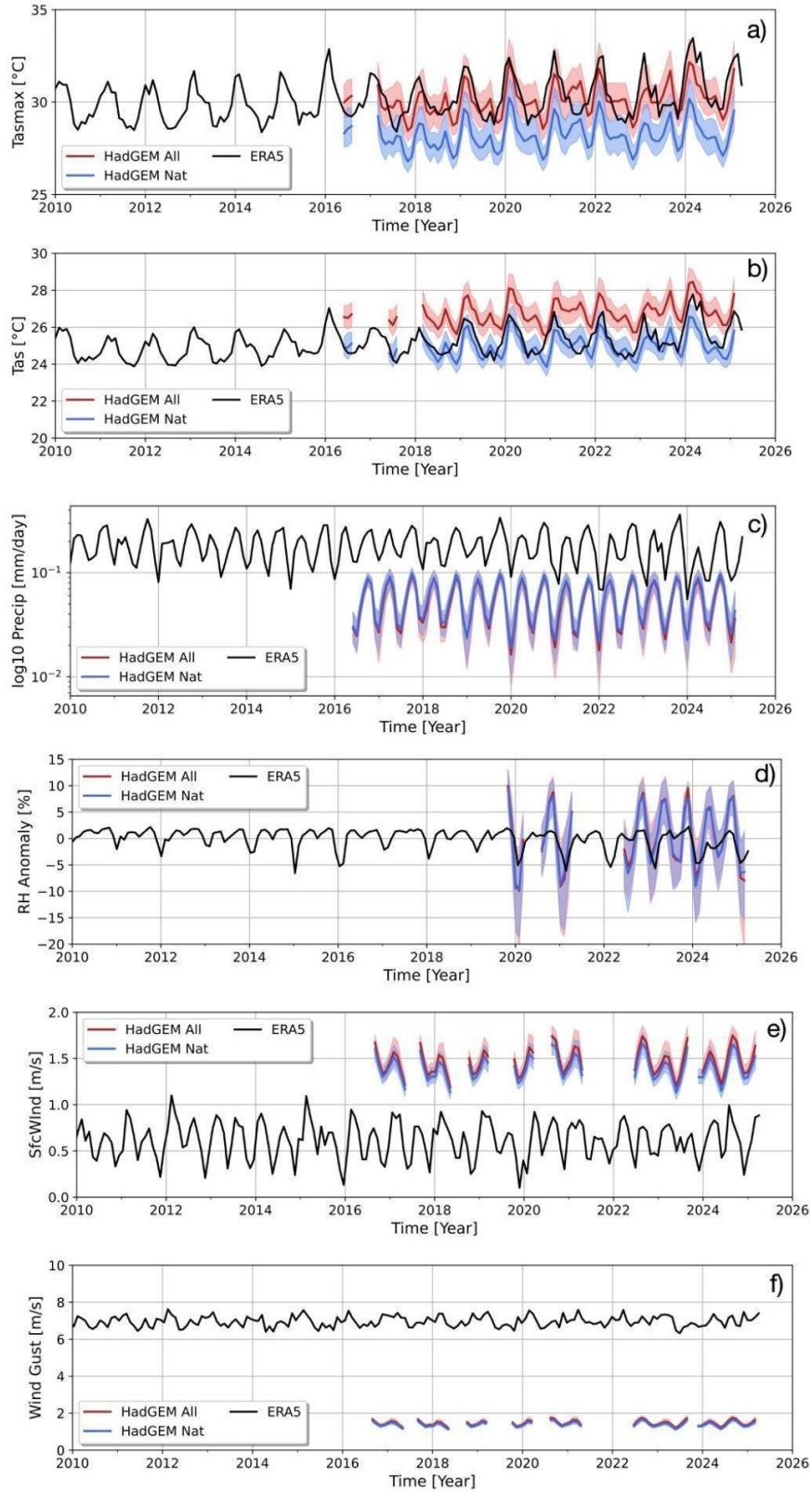
1384
1385
1386 **Figure S50:** Same as in figure S48, but for the Congo Basin.
1387
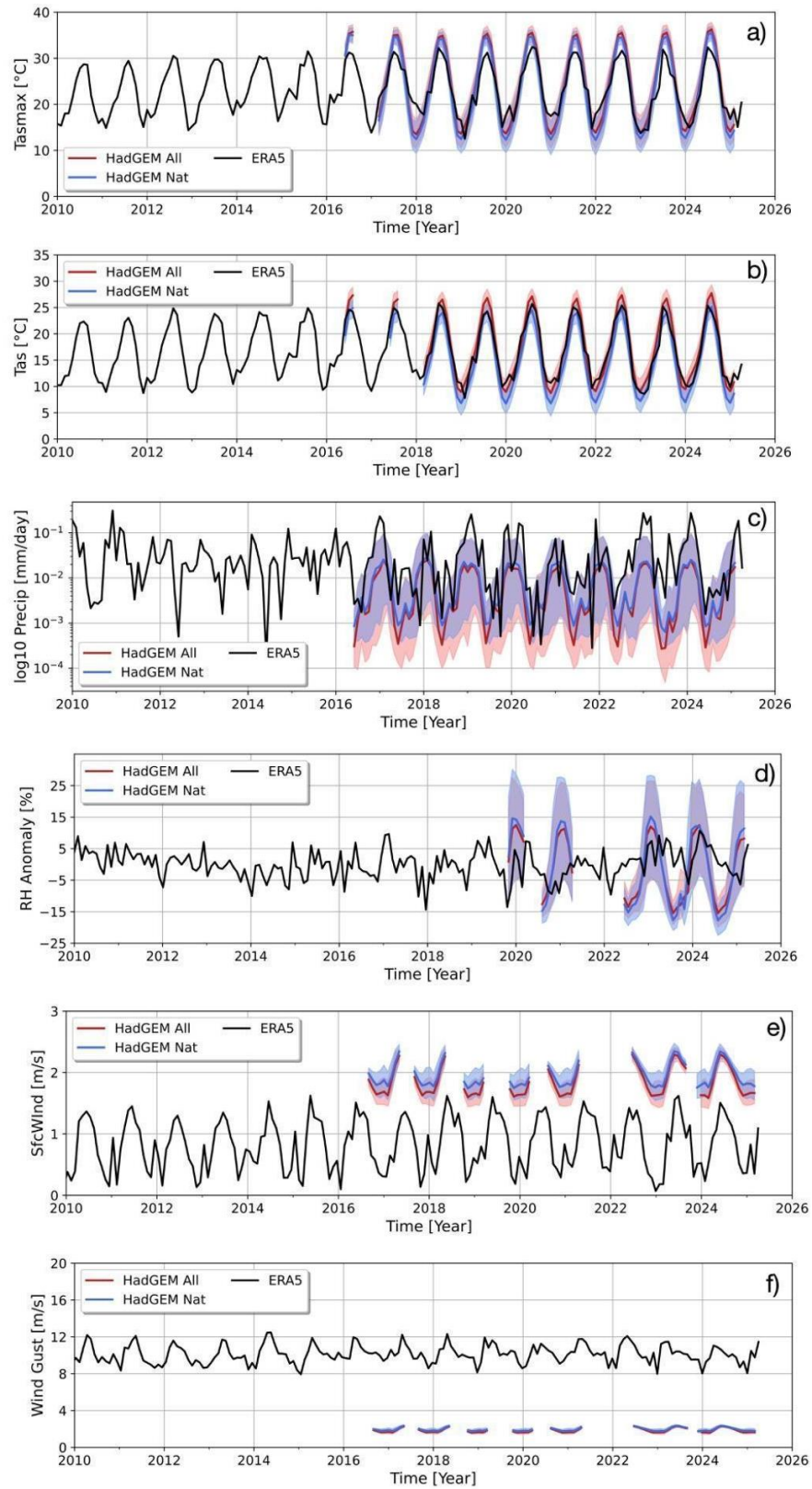
1388
1389 **Figure S51:** Same as in figure S48, but for the Souther California region.
1390
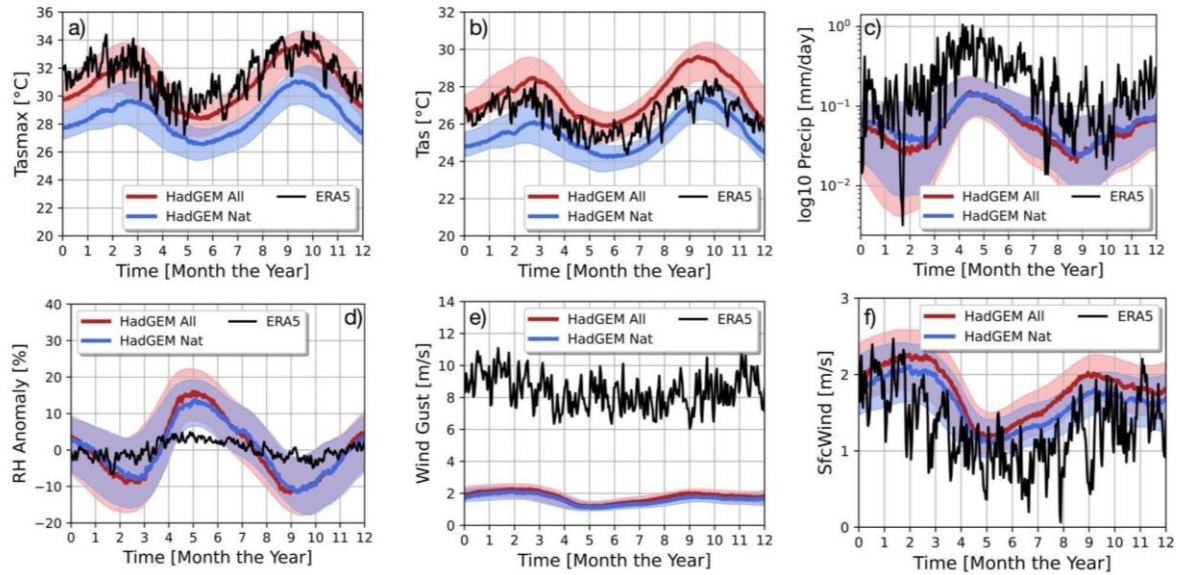
1391
1392 **Figure S52:** Seasonal cycle of individual component variables of the FWI from HadGEM (red:
1393 all forcing scenario, blue: natural forcing scenario) compared to ERA5 reanalysis (black)
1394 across 2024 over the northeast Amazonia region. We show daily a) maximum temperature,
1395 b) mean temperature, c) total precipitation, d) relative humidity, e) wind gusts as well as f)
1396 mean wind speed. Shading represents the 5th-95th percentile confidence interval.
1397
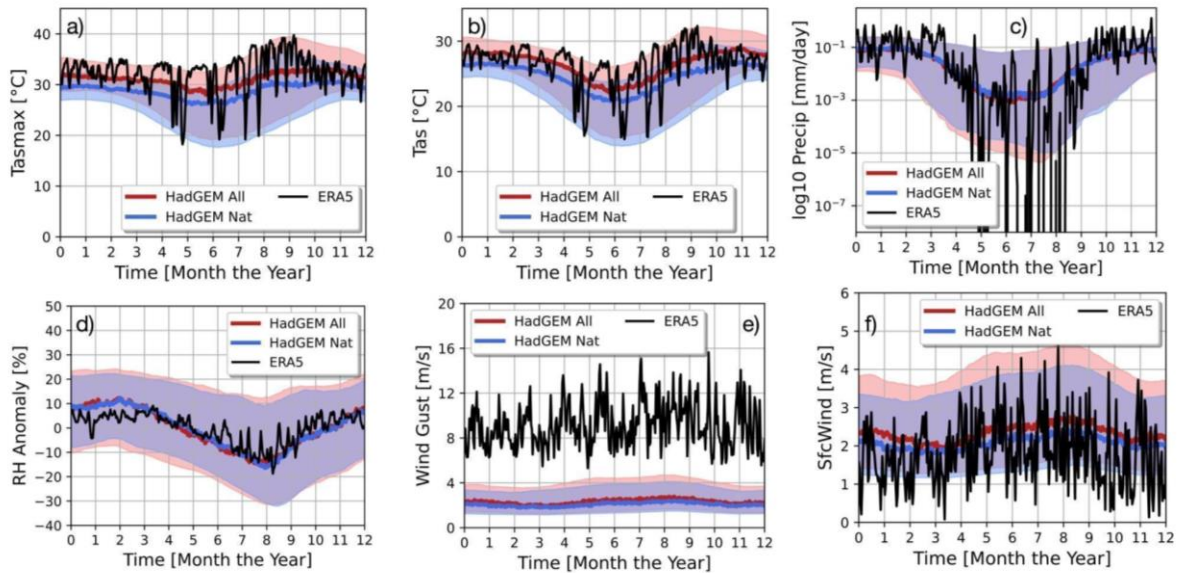
1398
1399 **Figure S53:** Same as in figure S52, but for the Pantanal-Chiquitano.
1400
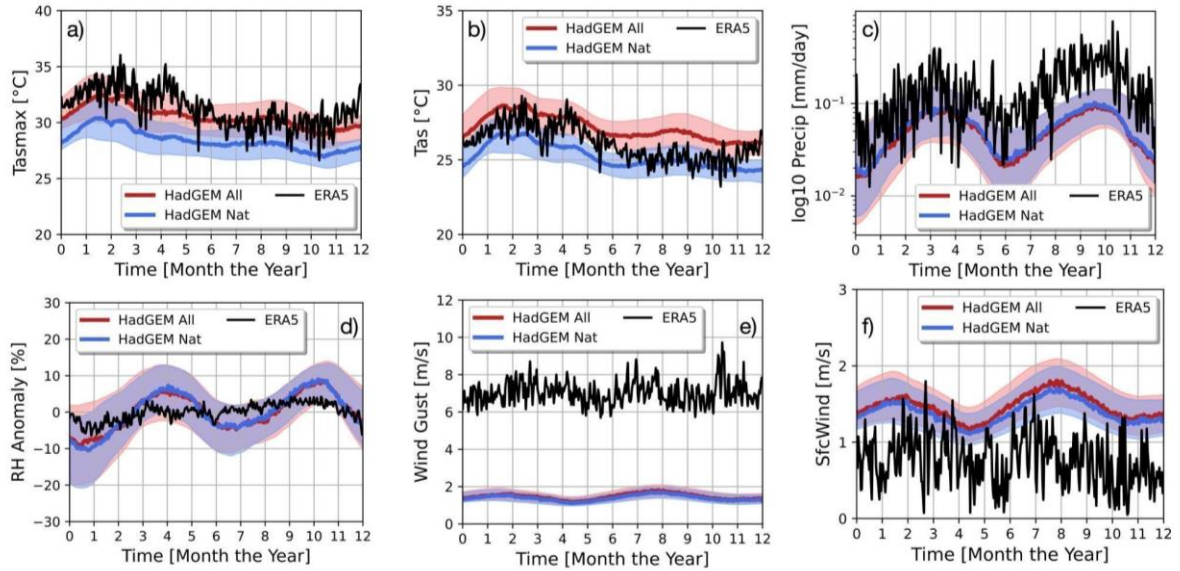
Figure S54: Same as in figure S52, but for the Congo Basin.
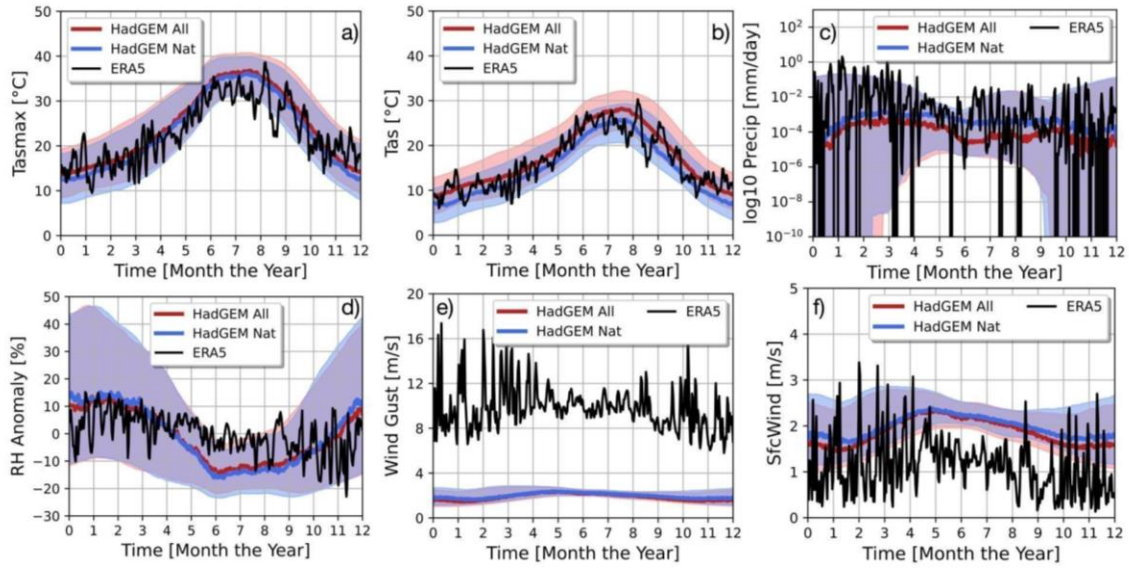
Figure S55: Same as in figure S52, but for the Southern California egion.
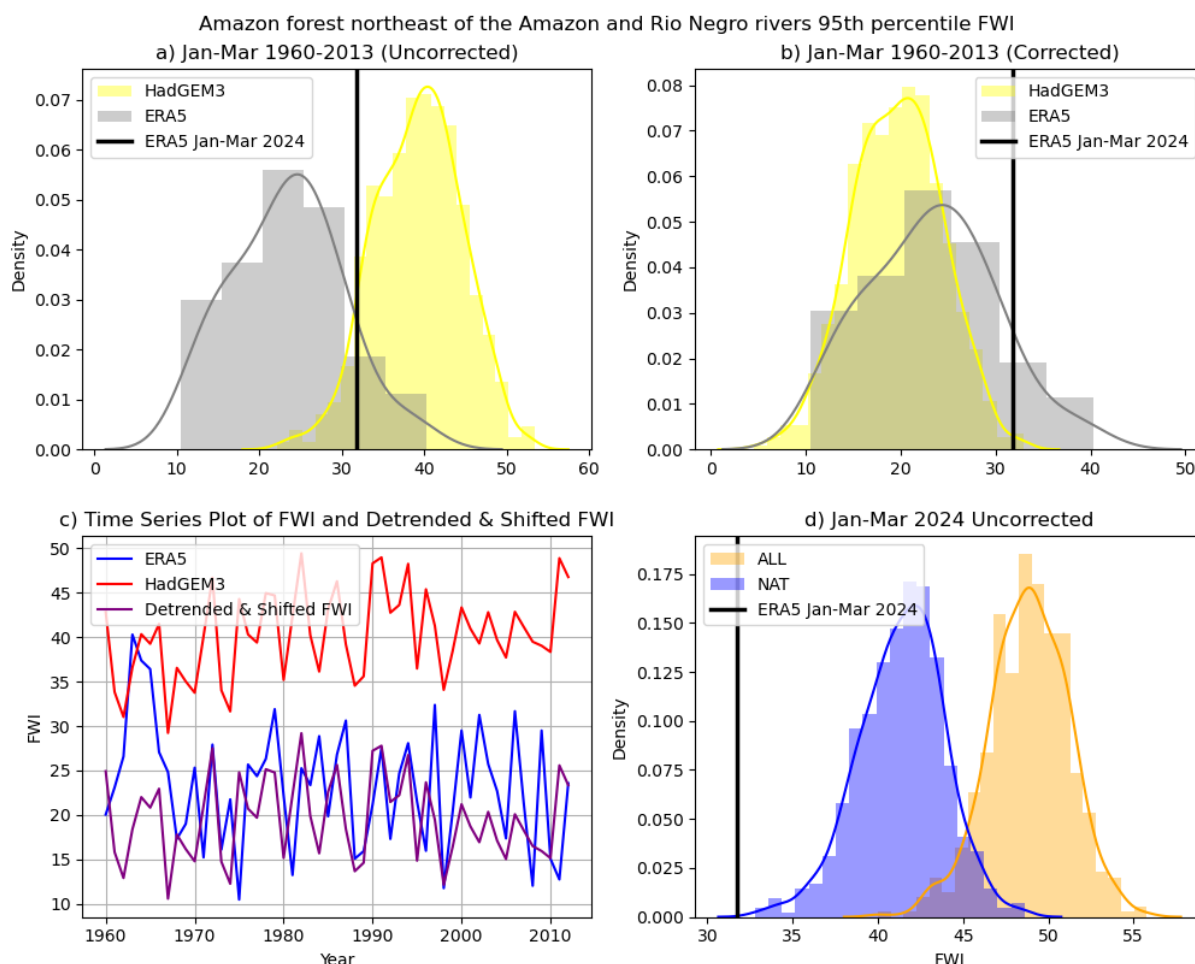
1409
1410 **Figure S56:** Bias correction for Amazon forest northeast of the Amazon and Rio Negro rivers.
1411 Historical ensemble of HadGEM3 (yellow) compared to ERA5 (grey) 95th percentile of FWI
1412 for the historical period (1960-2013), shown as probability density before correction (a) and
1413 after correction (b), and one member shown as a time series (c, where HadGEM3 is shown in
1414 red, ERA5 in blue and corrected HadGEM3 in purple). HadGEM3 ensemble for 2024 shown
1415 before bias-correction (d). ERA5 2024 event shown as black vertical line on all probability
1416 density plots.
1417
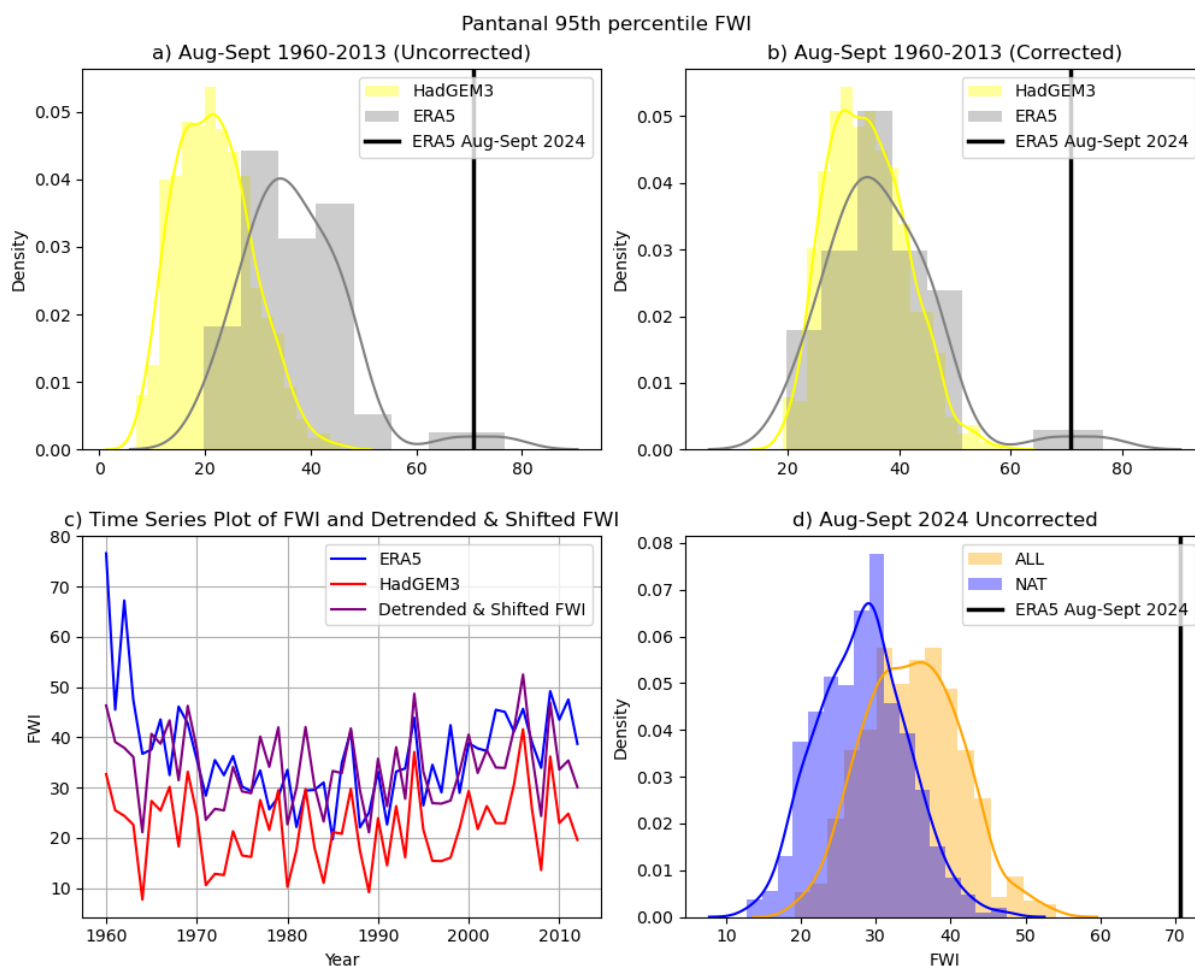
1418
1419   **Figure S57:** As for **Figure S56**, but for Pantanal & Chiquitano
1420
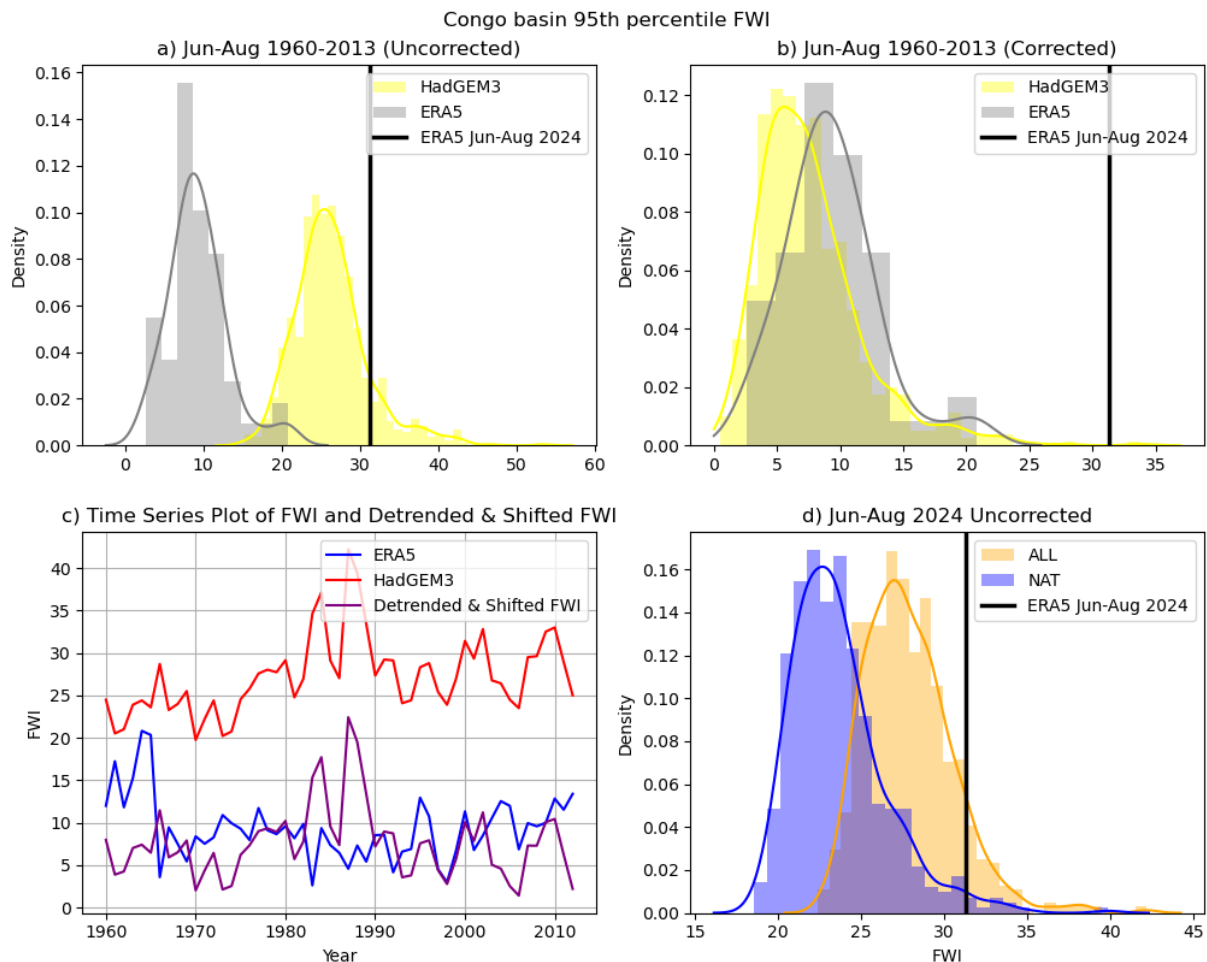
1421
1422 **Figure S58:** As for **Figure S56**, but for Congo basin
1423
1424
1425
1426
1427

Supplementary References

1429 Abatzoglou, J. T., Williams, A. P., Boschetti, L., Zubkova, M., and Kolden, C. A.: Global
1430 patterns of interannual climate--fire relationships, Glob. Chang. Biol., 24, 5164–5175, 2018.

1431 Abatzoglou, J. T., Williams, A. P., and Barbero, R.: Global emergence of anthropogenic
1432 climate change in fire weather indices, Geophys. Res. Lett., 46, 326–336,
1433 https://doi.org/10.1029/2018gl080959, 2019.

1434 Andela, N., Morton, D. C., Giglio, L., Chen, Y., van der Werf, G. R., Kasibhatla, P. S.,
1435 DeFries, R. S., Collatz, G. J., Hantson, S., Kloster, S., Bachelet, D., Forrest, M., Lasslop, G.,
1436 Li, F., Mangeon, S., Melton, J. R., Yue, C., and Randerson, J. T.: A human-driven decline in
1437 global burned area, Science, 356, 1356–1362, https://doi.org/10.1126/science.aal4108,
1438 2017.

1439 Barbero, R., Abatzoglou, J. T., Steel, E. A., and K Larkin, N.: Modeling very large-fire
1440 occurrences over the continental United States from weather and climate forcing, Environ.
1441 Res. Lett., 9, 124009, https://doi.org/10.1088/1748-9326/9/12/124009, 2014.

1442 Barbosa, M. L. F., Kelley, D. I., Burton, C. A., Ferreira, I. J. M., da Veiga, R. M., Bradley, A.,

1443 Molin, P. G., and Anderson, L. O.: FLAME 1.0: a novel approach for modelling burned area
1444 in the Brazilian biomes using the maximum entropy concept, Geosci. Model Dev., 18, 3533–
1445 3557, https://doi.org/10.5194/gmd-18-3533-2025, 2025.

1446 Boussetta, S., Balsamo, G., Arduini, G., Dutra, E., McNorton, J., Choulga, M., Agustí-
1447 Panareda, A., Beljaars, A., Wedi, N., Munõz-Sabater, J., de Rosnay, P., Sandu, I., Hadade,
1448 I., Carver, G., Mazzetti, C., Prudhomme, C., Yamazaki, D., and Zsoter, E.: ECLand: The
1449 ECMWF land surface modelling system, Atmosphere (Basel), 12, 723,
1450 https://doi.org/10.3390/atmos12060723, 2021.

1451 Burton, C., Betts, R., Cardoso, M., Feldpausch, T. R., Harper, A., Jones, C. D., Kelley, D. I.,
1452 Robertson, E., and Wiltshire, A.: Representation of fire, land-use change and vegetation
1453 dynamics in the Joint UK Land Environment Simulator vn4. 9 (JULES), Geoscientific Model
1454 Development, 12, 179–193, 2019.

1455 Burton, C., Betts, R. A., Jones, C. D., Feldpausch, T. R., Cardoso, M., and Anderson, L. O.:
1456 El Niño Driven Changes in Global Fire 2015/16, Front Earth Sci. Chin., 8,
1457 https://doi.org/10.3389/feart.2020.00199, 2020.

1458 Burton, C., Kelley, D. I., Jones, C. D., Betts, R. A., Cardoso, M., and Anderson, L.: South
1459 American fires and their impacts on ecosystems increase with continued emissions, Climate
1460 Resilience and Sustainability, 1, e8, https://doi.org/10.1002/cli2.8, 2022.

1461 Burton, C. A., Lampe, S., Kelley, D., Thiery, W., Hantson, S., Christidis, N., Gudmundsson,
1462 L., Forrest, M., Burke, E., Chang, J., Huang, H., Ito, A., Kou-Giesbrecht, S., Lasslop, G., Li,
1463 W., Nieradzik, L., Li, F., Chen, Y., Randerson, J., Reyer, C. P. O., and Mengel, M.: Global
1464 burned area increasingly explained by climate change, Nat. Clim. Chang., 1–7,
1465 https://doi.org/10.1038/s41558-024-02140-w, 2024.

1466 Burton, C. A., Ciavarella, A., Kelley, D., Hartley, A. J., McCarthy, M., S. New, Betts, R. A.,
1467 and Robertson, E.: Very high fire danger in UK in 2022 at least 6 times more likely due to
1468 human-caused climate change, Environ. Res. Lett., 20, https://doi.org/10.1088/1748-
1469 9326/adb764, 2025.

1470 Center for International Earth Science Information Network (CIESIN): Gridded Population of
1471 the World, Version 4 (GPWv4): Population Count, Revision 11, 2025.

1472 Chuvieco, E., Lucrecia Pettinari, M., Lizundia-Loiola, J., Khairoun, A., Danne, O., Boettcher,
1473 M., and Storm, T.: ESA Fire Climate Change Initiative (Fire_cci): Sentinel-3 SYN Burned
1474 Area Grid product, version 1.1, 2024.

1475 Clark, D. B., Mercado, L. M., Sitch, S., Jones, C. D., Gedney, N., Best, M. J., Pryor, M.,
1476 Rooney, G. G., Essery, R. L. H., Blyth, E., Boucher, O., Harding, R. J., Huntingford, C., and
1477 Cox, P. M.: The Joint UK Land Environment Simulator (JULES), model description – Part 2:
1478 Carbon fluxes and vegetation dynamics, Geoscientific Model Development, 4, 701–722,
1479 https://doi.org/10.5194/gmd-4-701-2011, 2011.

1480 CMES: Fire danger indices historical data from the Copernicus Emergency Management
1481 Service, https://doi.org/10.24381/CDS.0E89C522, 2019.

1482 Cunningham, D., Cunningham, P., and Fagan, M. E.: Evaluating forest cover and
1483 fragmentation in Costa Rica with a corrected global tree cover map, Remote Sens. (Basel),
1484 12, 3226, https://doi.org/10.3390/rs12193226, 2020.

1485 Di Giuseppe, F., Pappenberger, F., Wetterhall, F., Krzeminski, B., Camia, A., Libertá, G.,
1486 and San Miguel, J.: The potential predictability of fire danger provided by numerical weather

1487   prediction, J. Appl. Meteorol. Climatol., 55, 2469–2491, https://doi.org/10.1175/jamc-d-15-
1488   0297.1, 2016.

1489   Dimiceli, C., Carroll, M., Sohlberg, R., Kim, D.-H., and Kelly, M.: MOD44B MODIS/Terra
1490   Vegetation Continuous Fields Yearly L3 Global 250m SIN Grid V006,
1491   https://doi.org/10.5067/MODIS/MOD44B.006, 2015.

1492   Eden, J. M., Wolter, K., Otto, F. E. L., and Jan van Oldenborgh, G.: Multi-method attribution
1493   analysis of extreme precipitation in Boulder, Colorado, Environ. Res. Lett., 11, 124009,
1494   https://doi.org/10.1088/1748-9326/11/12/124009, 2016.

1495   Eden, J. M., Kew, S. F., Bellprat, O., Lenderink, G., Manola, I., Omrani, H., and J., van O.
1496   G.: Extreme precipitation in the Netherlands: An event attribution case study, Weather and
1497   climate extremes, 21, 90–101, 2018.

1498   Efron, B. and Tibshirani, R.: The problem of regions, Ann. Stat., 26, 1687–1718,
1499   https://doi.org/10.1214/aos/1024691353, 1998.

1500   Eyring, V., Bony, S., Meehl, G. A., Senior, C. A., Stevens, B., Stouffer, R. J., and Taylor, K.
1501   E.: Overview of the Coupled Model Intercomparison Project Phase 6 (CMIP6) experimental
1502   design and organization, Geosci. Model Dev., 9, 1937–1958, https://doi.org/10.5194/gmd-9-
1503   1937-2016, 2016.

1504   Giglio, L.: VIIRS/NPP Burned Area Monthly L4 Global 500m SIN Grid V002,
1505   https://doi.org/10.5067/VIIRS/VNP64A1.002, 2024.

1506   Giglio, L., Boschetti, L., Roy, D. P., Humber, M. L., and Justice, C. O.: The Collection 6
1507   MODIS burned area mapping algorithm and product, Remote Sens. Environ., 217, 72–85,
1508   https://doi.org/10.1016/j.rse.2018.08.005, 2018.

1509   Gneiting, T. and Katzfuss, M.: Probabilistic forecasting, Annu. Rev. Stat. Appl., 1, 125–151,
1510   https://doi.org/10.1146/annurev-statistics-062713-085831, 2014.

1511   Goss, M., Swain, D. L., Abatzoglou, J. T., Sarhadi, A., Kolden, C. A., Williams, A. P., and
1512   Diffenbaugh, N. S.: Climate change is increasing the likelihood of extreme autumn wildfire
1513   conditions across California, Environ. Res. Lett., 15, 094016, https://doi.org/10.1088/1748-
1514   9326/ab83a7, 2020.

1515   Guzman-Morales, J. and Gershunov, A.: Climate change suppresses Santa Ana winds of
1516   southern California and sharpens their seasonality, Geophys. Res. Lett., 46, 2772–2780,
1517   https://doi.org/10.1029/2018gl080261, 2019.

1518   Hantson, S., Arneth, A., Harrison, S. P., and Kelley, D. I.: The status and challenge of global
1519   fire modelling, 2016.

1520   Hawkins, L. R., Abatzoglou, J. T., Li, S., and Rupp, D. E.: Anthropogenic influence on recent
1521   severe autumn fire weather in the west coast of the United States, Geophys. Res. Lett., 49,
1522   https://doi.org/10.1029/2021gl095496, 2022.

1523   Hersbach, H., Bell, B., Berrisford, P., Biavati, G., Horányi, A., Muñoz Sabater, J., Nicolas, J.,
1524   Peubey, C., Radu, R., Rozum, I., Schepers, D., Simmons, A., Soci, C., Dee, D., and
1525   Thépaut, J.-N.: ERA5 hourly data on single levels from 1940 to present,
1526   https://doi.org/10.24381/cds.adbb2d47, 2023.

1527   Huang, H., Xue, Y., Li, F., and Liu, Y.: Modeling long-term fire impact on ecosystem
1528   characteristics and surface energy using a process-based vegetation–fire model

1529   SSiB4/TRIFFID-Fire v1.0, Geosci. Model Dev., https://doi.org/10.5194/gmd-2020-122-
1530   supplement, 2020.

1531   Huang, H., Xue, Y., Liu, Y., Li, F., and Okin, G.: Modeling the short-term fire effects on
1532   vegetation dynamics and surface energy in Southern Africa using the improved
1533   SSiB4/TRIFFID-Fire model, https://doi.org/10.5194/gmd-2021-116, 2021.

1534   Hugelius, G., Tarnocai, C., Broll, G., Canadell, J. G., Kuhry, P., and Swanson, D. K.: The
1535   Northern Circumpolar Soil Carbon Database: spatially distributed datasets of soil coverage
1536   and soil carbon storage in the northern permafrost regions, Earth Syst. Sci. Data, 5, 3–13,
1537   https://doi.org/10.5194/essd-5-3-2013, 2013.

1538   Ito, A.: Disequilibrium of terrestrial ecosystem CO_2 budget caused by disturbance-induced
1539   emissions and non-CO_2 carbon export flows: a global model assessment, Earth Syst. Dyn.,
1540   10, 685–709, https://doi.org/10.5194/esd-10-685-2019, 2019.

1541   Jolly, W. M., Cochrane, M. A., Freeborn, P. H., Holden, Z. A., Brown, T. J., Williamson, G. J.,
1542   and Bowman, D. M. J. S.: Climate-induced variations in global wildfire danger from 1979 to
1543   2013, Nat. Commun., 6, 7537, https://doi.org/10.1038/ncomms8537, 2015.

1544   Jones, M. W., Abatzoglou, J. T., Veraverbeke, S., Andela, N., Lasslop, G., Forkel, M., Smith,
1545   A. J. P., Burton, C., Betts, R. A., van der Werf, G. R., Sitch, S., Canadell, J. G., Santín, C.,
1546   Kolden, C., Doerr, S. H., and Le Quéré, C.: Global and regional trends and drivers of fire
1547   under climate change, Rev. Geophys., 60, https://doi.org/10.1029/2020rg000726, 2022.

1548   Jones, M. W., Veraverbeke, S., Andela, N., Doerr, S. H., Kolden, C., Mataveli, G., Pettinari,
1549   M. L., Le Quéré, C., Rosan, T. M., van der Werf, G. R., van Wees, D., and Abatzoglou, J. T.:
1550   Global rise in forest fire emissions linked to climate change in the extratropics, Science, 386,
1551   eadl5889, https://doi.org/10.1126/science.adl5889, 2024a.

1552   Jones, M. W., Kelley, D. I., Burton, C. A., Di Giuseppe, F., Barbosa, M. L. F., Brambleby, E.,
1553   Hartley, A. J., Lombardi, A., Mataveli, G., McNorton, J. R., Spuler, F. R., Wessel, J. B.,
1554   Abatzoglou, J. T., Anderson, L. O., Andela, N., Archibald, S., Armenteras, D., Burke, E.,
1555   Carmenta, R., Chuvieco, E., Clarke, H., Doerr, S. H., Fernandes, P. M., Giglio, L., Hamilton,
1556   D. S., Hantson, S., Harris, S., Jain, P., Kolden, C. A., Kurvits, T., Lampe, S., Meier, S.,
1557   Stacey New, Parrington, M., Perron, M. M. G., Qu, Y., Ribeiro, N. S., Saharjo, B. H., San-
1558   Miguel-Ayanz, J., Shuman, J. K., Tanpipat, V., Van Der Werf, G. R., Veraverbeke, S., and
1559   Xanthopoulos, G.: State of Wildfires 2023–2024, Earth Syst. Sci. Data, 16, 3601–3685,
1560   https://doi.org/10.5194/essd-16-3601-2024, 2024b.

1561   Kelley, D. I., Prentice, I. C., Harrison, S. P., Wang, H., Simard, M., Fisher, J. B., and Willis,
1562   K. O.: A comprehensive benchmarking system for evaluating global vegetation models,
1563   Biogeosciences, 10, 3313–3340, https://doi.org/10.5194/bg-10-3313-2013, 2013.

1564   Kelley, D. I., Bistinas, I., Whitley, R., and Burton, C.: How contemporary bioclimatic and
1565   human controls change global fire regimes, Nat. Clim. Chang., 2019.

1566   Kelley, D. I., Burton, C., Huntingford, C., Brown, M. A. J., Whitley, R., and Dong, N.:
1567   Technical note: Low meteorological influence found in 2019 Amazonia fires, Biogeosciences,
1568   18, 787–804, https://doi.org/10.5194/bg-18-787-2021, 2021.

1569   Klein Goldewijk, K., Goldewijk, K. K., Beusen, A., Van Drecht, G., and De Vos, M.: The
1570   HYDE 3.1 spatially explicit database of human-induced global land-use change over the past
1571   12,000 years, Glob. Ecol. Biogeogr., 20, 73–86, https://doi.org/10.1111/j.1466-
1572   8238.2010.00587.x, 2010.

Knorr, W., Kaminski, T., Arneth, A., and Weber, U.: Impact of human population density on fire frequency at the global scale, Biogeosciences, 11, 1085–1102, 2014.

Knutti, R., Sedláček, J., Sanderson, B. M., Lorenz, R., Fischer, E. M., and Eyring, V.: A climate model projection weighting scheme accounting for performance and interdependence, Geophys. Res. Lett., 44, 1909–1918, https://doi.org/10.1002/2016gl072012, 2017.

Krikken, F., Lehner, F., Haustein, K., Drobyshev, I., and J., van O. G.: Attribution of the role of climate change in the forest fires in Sweden 2018, Natural Hazards and Earth System Sciences, 21, 2169–2179, 2021.

Lehsten, V., Tansey, K., Balzter, H., Thonicke, K., Spessa, A., Weber, U., Smith, B., and Arneth, A.: Estimating carbon emissions from African wildfires, Biogeosciences, 6, 349–360, https://doi.org/10.5194/bg-6-349-2009, 2009.

Li, F., Zeng, X. D., and Levis, S.: A process-based fire parameterization of intermediate complexity in a Dynamic Global Vegetation Model, Biogeosciences, 9, 2761–2780, https://doi.org/10.5194/bg-9-2761-2012, 2012.

Li, F., Levis, S., and Ward, D. S.: Quantifying the role of fire in the Earth system – Part 1: Improved global fire modeling in the Community Earth System Model (CESM1), Biogeosciences, 10, 2293–2314, https://doi.org/10.5194/bg-10-2293-2013, 2013.

Liu, J., Feng, X., Gu, X., Zhang, J., Slater, L. J., and Kong, D.: Detection and attribution of human influence on the global diurnal temperature range decline, Geophys. Res. Lett., 49, https://doi.org/10.1029/2021gl097155, 2022a.

Liu, W., Su, X., Zhang, G., and Chen, D.: Projection of future dry-wet evolution in Northwest China and its uncertainty attribution analysis, River, 2, 65–78, https://doi.org/10.1002/rvr2.39, 2023.

Liu, Z., Eden, J. M., Dieppois, B., and Blackett, M.: A global view of observed changes in fire weather extremes: uncertainties and attribution to climate change, Clim. Change, 173, https://doi.org/10.1007/s10584-022-03409-9, 2022b.

Liu, Z., Eden, J. M., Dieppois, B., Drobyshev, I., Gallo, C., and Blackett, M.: Were meteorological conditions related to the 2020 Siberia wildfires made more likely by anthropogenic climate change?, Bull. Am. Meteorol. Soc., 103, S44–S49, https://doi.org/10.1175/bams-d-21-0168.1, 2022c.

Li, Y., Sulla-Menashe, D., Motesharrei, S., Song, X.-P., Kalnay, E., Ying, Q., Li, S., and Ma, Z.: Inconsistent estimates of forest cover change in China between 2000 and 2013 from multiple datasets: differences in parameters, spatial resolution, and definitions, Sci. Rep., 7, 8748, https://doi.org/10.1038/s41598-017-07732-5, 2017.

Lizundia-Loiola, J., Franquesa, M., Khairoun, A., and Chuvieco, E.: Global burned area mapping from Sentinel-3 Synergy and VIIRS active fires, Remote Sens. Environ., 282, 113298, https://doi.org/10.1016/j.rse.2022.113298, 2022.

Lopez, P.: A lightning parameterization for the ECMWF Integrated Forecasting System, Mon. Weather Rev., 144, 3057–3075, https://doi.org/10.1175/mwr-d-16-0026.1, 2016.

Mangeon, S., Voulgarakis, A., Gilham, R., Harper, A., Sitch, S., and Folberth, G.: INFERNO: a fire and emissions scheme for the UK Met Office's Unified Model, Geosci. Model Dev., 9, 2685–2700, https://doi.org/10.5194/gmd-9-2685-2016, 2016.

Mataveli, G., Maure, L. A., Sanchez, A., Dutra, D. J., de Oliveira, G., Jones, M. W., Amaral, C., Artaxo, P., and Aragão, L. E. O. C.: Forest degradation is undermining progress on deforestation in the Amazon, Glob. Chang. Biol., 31, e70209, https://doi.org/10.1111/gcb.70209, 2025.

Mathison, C., Burke, E., Hartley, A. J., Kelley, D. I., Burton, C., Robertson, E., Gedney, N., Williams, K., Wiltshire, A., Ellis, R. J., and Others: Description and evaluation of the JULES-ES set-up for ISIMIP2b, Geoscientific Model Development, 16, 4249–4264, 2023.

McNorton, J. and Di Giuseppe, F.: A global fuel characteristic model and dataset for wildfire prediction, Biogeosciences, https://doi.org/10.5194/bg-21-279-2024, 2024.

McNorton, J., Agustí-Panareda, A., Arduini, G., Balsamo, G., Bousserez, N., Boussetta, S., Chericoni, M., Choulga, M., Engelen, R., and Guevara, M.: An urban scheme for the ECMWF integrated forecasting system: Global forecasts and residential CO_2 emissions, J. Adv. Model. Earth Syst., 15, e2022MS003286, https://doi.org/10.1029/2022ms003286, 2023.

Meijer, J. R., Huijbregts, M. A. J., Schotten, K. C. G. J., and Schipper, A. M.: Global patterns of current and future road infrastructure, Environ. Res. Lett., 13, 064006, https://doi.org/10.1088/1748-9326/aabd42, 2018.

Melton, J., Arora, V., Wisernig-Cojoc, E., Seiler, C., Fortier, M., Chan, E., and Teckentrup, L.: CLASSIC v1.0: the open-source community successor to the Canadian Land Surface Scheme (CLASS) and the Canadian Terrestrial Ecosystem Model (CTEM) – Part 1: Model framework and site-level performance, Geosci. Model Dev., https://doi.org/10.5194/gmd-2019-329-supplement, 2019.

Mengel, M., Treu, S., Lange, S., and Frieler, K.: ATTRICI v1. 1--counterfactual climate for impact attribution, Geoscientific Model Development, 14, 5269–5284, 2021.

Muñoz-Sabater, J., Dutra, E., Agustí-Panareda, A., Albergel, C., Arduini, G., Balsamo, G., Boussetta, S., Choulga, M., Harrigan, S., Hersbach, H., Martens, B., Miralles, D. G., Piles, M., Rodríguez-Fernández, N. J., Zsoter, E., Buontempo, C., and Jean-Noël Thépaut: ERA5-Land: a state-of-the-art global reanalysis dataset for land applications, Earth Syst. Sci. Data, 13, 4349–4383, https://doi.org/10.5194/essd-13-4349-2021, 2021.

Otto, F., van der Wiel, K., van Oldenborgh, G. J., Philip, S., Kew, S., Uhe, P., and Cullen, H.: Climate change increases the probability of heavy rains in Northern England/Southern Scotland like those of storm Desmond—a real-time event attribution revisited, Environmental Research Letters, 13, https://doi.org/10.1088/1748-9326/aa9663, 2018.

Philip, S., Kew, S., van Oldenborgh, G. J., Otto, F., Vautard, R., van der Wiel, K., King, A., Lott, F., Arrighi, J., Singh, R., and van Aalst, M.: A protocol for probabilistic extreme event attribution analyses, Adv. Stat. Clim. Meteorol. Oceanogr., 6, 177–203, https://doi.org/10.5194/ascmo-6-177-2020, 2020.

Quilcaille, Y., Batibeniz, F., Ribeiro, A. F. S., Padrón, R. S., and Seneviratne, S. I.: Fire weather index data under historical and shared socioeconomic pathway projections in the 6th phase of the Coupled Model Intercomparison Project from 1850 to 2100, Earth Syst. Sci. Data, 15, 2153–2177, https://doi.org/10.5194/essd-15-2153-2023, 2023.

Qu, Y., Jones, M. W., Brambleby, E., Hunt, H. G. P., Pérez-Invernón, F. J., Yebra, M., Zhao, L., Moris, J. V., Janssen, T., and Veraverbeke, S.: A new global gridded lightning dataset with high spatial and temporal resolution, , https://doi.org/10.5194/egusphere-egu25-8351, 2025.

1660 Rabin, S. S., Melton, J. R., and Lasslop, G.: The Fire Modeling Intercomparison Project
1661 (FireMIP), phase 1: experimental and analytical protocols with detailed model descriptions,
1662 Geoscientific Model, 2017.

1663 Schaller, N., Otto, F., Oldenborgh, G. V., Massey, N., Sparrow, S., and Allen: The heavy
1664 precipitation event of may-June 2013 in the upper Danube and Elbe basins, Bulletin of the
1665 American Meteorological Society, 95, 2014.

1666 Scholten, R. C., Jandt, R., Miller, E. A., Rogers, B. M., and Veraverbeke, S.: Overwintering
1667 fires in boreal forests, Nature, 593, 399–404, https://doi.org/10.1038/s41586-021-03437-y,
1668 2021.

1669 Sellar, A. A., Walton, J., Jones, C. G., and Wood, R.: Implementation of UK Earth system
1670 models for CMIP6, Journal of Advances, 2020.

1671 Sexton, J. O., Noojipady, P., Song, X.-P., Feng, M., Song, D.-X., Kim, D.-H., Anand, A.,
1672 Huang, C., Channan, S., Pimm, S. L., and Townshend, J. R.: Conservation policy and the
1673 measurement of forests, Nat. Clim. Chang., 6, 192–196,
1674 https://doi.org/10.1038/nclimate2816, 2016.

1675 Smith, B., Wårlind, D., Arneth, A., Hickler, T., Leadley, P., Siltberg, J., and Zaehle, S.:
1676 Implications of incorporating N cycling and N limitations on primary production in an
1677 individual-based dynamic vegetation model, Biogeosciences, 11, 2027–2054,
1678 https://doi.org/10.5194/bg-11-2027-2014, 2014.

1679 Spuler, F., Wessel, J., Comyn-Platt, E., Varndell, J., and Cagnazzo, C.: ibicus: a new open-
1680 source Python package and comprehensive interface for statistical bias adjustment and
1681 evaluation in climate modelling (v1.0.1), Geosci. Model Dev., https://doi.org/10.5194/gmd-
1682 17-1249-2024, 2024.

1683 ibicus: https://pypi.org/project/ibicus/, last access: 7 August 2024.

1684 Swart, N. C., Cole, J. N. S., Kharin, V. V., Lazare, M., Scinocca, J. F., Gillett, N. P., Anstey,
1685 J., Arora, V., Christian, J. R., Hanna, S., Jiao, Y., Lee, W. G., Majaess, F., Saenko, O. A.,
1686 Seiler, C., Seinen, C., Shao, A., Solheim, L., von Salzen, K., Yang, D., and Winter, B.: The
1687 Canadian Earth System Model version 5 (CanESM5.0.3), Geosci. Model Dev. Discuss., 1–
1688 68, https://doi.org/10.5194/gmd-2019-177, 2019.

1689 Thonicke, K., Venevsky, S., Sitch, S., and Cramer, W.: The role of fire disturbance for global
1690 vegetation dynamics: coupling fire into a Dynamic Global Vegetation Model, Glob. Ecol.
1691 Biogeogr., 10, 661–677, https://doi.org/10.1046/j.1466-822x.2001.00175.x, 2008.

1692 Thonicke, K., Spessa, A., Prentice, I. C., Harrison, S. P., Dong, L., and Carmona-Moreno,
1693 C.: The influence of vegetation, fire spread and fire behaviour on biomass burning and trace
1694 gas emissions: results from a process-based model, Biogeosciences, 7, 1991–2011,
1695 https://doi.org/10.5194/bg-7-1991-2010, 2010.

1696 Torres-Vázquez, M. Á., Herrera, S., Gincheva, A., Halifa-Marín, A., Cavicchia, L., Di
1697 Giuseppe, F., Montávez, J. P., and Turco, M.: Enhancing seasonal fire predictions with
1698 hybrid dynamical and random forest models, NPJ Nat. Hazards, 2, 1–10,
1699 https://doi.org/10.1038/s44304-025-00069-4, 2025.

1700 Turco, M., Jerez, S., Doblas-Reyes, F. J., AghaKouchak, A., Llasat, M. C., and Provenzale,
1701 A.: Skilful forecasting of global fire activity using seasonal climate predictions, Nat.
1702 Commun., 9, 2718, https://doi.org/10.1038/s41467-018-05250-0, 2018.

1703 Turco, M., Jones, M. W., and Di Giuseppe, F.: State of Wildfires 2024-25: Anomalies in
1704 Extreme Fire Weather Days by Continent, Biome, Country, and Administrative Region,
1705 https://doi.org/10.5281/zenodo.15538595, 2025.

1706 UNEP, Popescu, A., Paulson, A. K., Christianson, A. C., Sullivan, A., Tulloch, A., Bilbao, B.,
1707 Mathison, C., Robinson, C., Burton, C., Ganz, D., Nangoma, D., Saah, D., Armenteras, D.,
1708 Driscoll, D., Hankins, D. L., Kelley, D. I., Langer, E. R. L., Baker, E., Berenguer, E., Reisen,
1709 F., Robinne, F.-N., Galudra, G., Humphrey, G., Safford, H., Baird, I. G., Oliveras, I., Littell, J.,
1710 Kieft, J., Chew, J., Maclean, K., Wittenberg, L., Anderson, L. O., Gillson, L., Plucinski, M.,
1711 Moritz, M., Brown, M., Soto, M. C., Flannigan, M., Costello, O., Silva, P. S., Fernandes, P.,
1712 Moore, P., Jandt, R., Blanchi, R., Libonati, R., Archibald, S., Dunlop, S., McCaffrey, S.,
1713 Page, S., Gonzãƒâ¡lez, T. D. T., Sokchea, T., and Charlton, V.: Spreading like Wildfire: The
1714 Rising Threat of Extraordinary Landscape Fires, edited by: Sullivan, A., Kurvits, T., and E.,
1715 B., United Nations Environment Programme and GRID-Arendal., 2022.

1716 Vitolo, C., Di Giuseppe, F., Barnard, C., Coughlan, R., San-Miguel-Ayanz, J., Libertá, G.,
1717 and Krzeminski, B.: ERA5-based global meteorological wildfire danger maps, Sci. Data, 7,
1718 216, https://doi.org/10.1038/s41597-020-0554-z, 2020.

1719 van Wagner, C. E.: Development and structure of the Canadian forest fire weather index
1720 system, cabidigitallibrary.org, https://doi.org/10.5555/19910646918, 1987.

1721 van der Wiel, K., Kapnick, S. B., van Oldenborgh, G. J., Whan, K., Philip, S., Vecchi, G. A.,
1722 Singh, R. K., Arrighi, J., and Cullen, H.: Rapid attribution of the August 2016 flood-inducing
1723 extreme precipitation in south Louisiana to climate change, Hydrol. Earth Syst. Sci., 21, 897–
1724 921, https://doi.org/10.5194/hess-21-897-2017, 2017.

1725 Yue, C., Ciais, P., Cadule, P., Thonicke, K., Archibald, S., Poulter, B., Hao, W., Hantson, S.,
1726 Mouillot, F., Friedlingstein, P., Maignan, F., and Viovy, N.: Modelling the role of fires in the
1727 terrestrial carbon balance by incorporating SPITFIRE into the global vegetation model
1728 ORCHIDEE – Part 1: simulating historical global burned area and fire regimes, Geoscientific
1729 Model Development, 7, 2747–2767, https://doi.org/10.5194/GMD-7-2747-2014, 2014.

1730 Yue, C., Cadule, P., and Van Leeuwen, T. T.: Modelling the role of fires in the terrestrial
1731 carbon balance by incorporating SPITFIRE into the global vegetation model ORCHIDEE--
1732 Part 2: Carbon emissions and the role of fires in the global carbon balance, Geoscientific
1733 Model Development, 8, 1321–1338, 2015.

1734 Zheng, B., Ciais, P., Chevallier, F., Yang, H., Canadell, J. G., Chen, Y., van der Velde, I. R.,
1735 Aben, I., Chuvieco, E., Davis, S. J., Deeter, M., Hong, C., Kong, Y., Li, H., Li, H., Lin, X., He,
1736 K., and Zhang, Q.: Record-high CO2 emissions from boreal fires in 2021, Science, 379,
1737 912–917, https://doi.org/10.1126/science.ade0805, 2023.

1738 Zubkova, M., Giglio, L., Boschetti, L., Roy, D., Hall, J., and Humber, M. L.: The NASA Visible
1739 Infrared Imaging Radiometer Suite (VIIRS) burned area product - VNP64A1, AGUFM, 2024,
1740 B13I–1644, 2024.

1741